RSC Advances

REVIEW

View Article Online
View Journal | View Issue

Cite this: *RSC Adv.*, 2023, **13**, 18404

Experimental and computational study of metal oxide nanoparticles for the photocatalytic degradation of organic pollutants: a review

Fikadu Takele Geldasa, [ad] Mesfin Abayneh Kebede, [b] Megersa Wodajo Shura [a] and Fekadu Gashaw Hone [*c]

Photocatalysis is a more proficient technique that involves the breakdown or decomposition of different organic contaminants, various dyes, and harmful viruses and fungi using UV or visible light solar spectrum. Metal oxides are considered promising candidate photocatalysts owing to their low cost, efficiency, simple fabricating method, sufficient availability, and environment-friendliness for photocatalytic applications. Among metal oxides, TiO_2 is the most studied photocatalyst and is highly applied in wastewater treatment and hydrogen production. However, TiO_2 is relatively active only under ultraviolet light due to its wide bandgap, which limits its applicability because the production of ultraviolet is expensive. At present, the discovery of a photocatalyst of suitable bandgap with visible light or modification of the existing photocatalyst is becoming very attractive for photocatalysis technology. However, the major drawbacks of photocatalysts are the high recombination rate of photogenerated electron–hole pairs, the ultraviolet light activity limitations, and low surface coverage. In this review, the most commonly used synthesis method for metal oxide nanoparticles, photocatalytic applications of metal oxides, and applications and toxicity of different dyes are comprehensively highlighted. In addition, the challenges in the photocatalytic applications of metal oxides, strategies to suppress these challenges, and metal oxide studied by density functional theory for photocatalytic applications are described in detail.

Received 7th March 2023
Accepted 31st May 2023

DOI: 10.1039/d3ra01505j

rsc.li/rsc-advances

[a]*Adama Science and Technology University, Department of Applied Physics, P. O. Box1888, Adama, Ethiopia*
[b]*Institute for Nanotechnology and Water Sustainability, College of Science, Engineering and Technology, University of South Africa, Florida Science Campus, Johannesburg, 1710, South Africa*
[c]*Addis Ababa University, Department of Physics, P.O. Box: 1176, Addis Ababa, Ethiopia. E-mail: fekadu.gashaw@aau.edu.et*
[d]*Oda Bultum University, Department of Physics, P. O. Box 226, Chiro, Ethiopia*

Fikadu Takele was born in Welega, Ethiopia, in 1993. He received his BSc degree in Applied Physics from Hawassa University in 2015 and his MSc degree in Solid State Physics from Dilla University, in 2017. Currently he is a PhD student at Adama Science and Technology University under the supervision of Dr Fekadu Gashaw, Dr Mesfin Abayneh and Dr Megersa Wodajo. His research interest is on energy storage electrode materials specifically on lithium ion batteries.

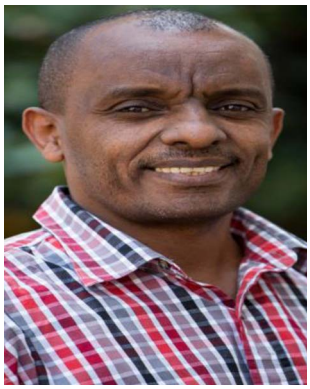

Mesfin Kebede obtained his PhD in Metallurgical Engineering/ Applied Physics from Inha University, South Korea. He is currently a Principal Research Scientist at Energy Centre of Council for Scientific and Industrial Research (CSIR), South Africa. In addition, he holds Honorary Associate Professor position at University of the Witwatersrand, South Africa. His current research mainly focuses on the development and characterization of electrode materials for energy storage and fabrication of coin cell and pouch cell for full cells. Improving the electrochemical performance of electrode materials for energy storage systems such as lithium-ion batteries, sodium-ion batteries, and supercapacitors.

1 Introduction

Nowadays, environmental pollution and the energy crisis are the two main concerns of our world. With urban growth and rapid industrialization, our globe is in an era of prosperity and wealth. The increasing world population and continuous development of urban, industrial, and agricultural processes cause an increase in pollutants in air and water sources. Human activity due to population growth, such as household activity and the development of industrial and agricultural byproducts, leads to mostly organic contaminants. If these organic contaminants are biodegradable, it can be easily treated by biological processes. However, pollutants from industries, such as textiles, pharmaceuticals, and agriculture, often contain low biodegradability. In addition to these, chemicals, microbes, metal plating, pulp, refineries, and food processing are waste-generating businesses that discharge many wastes, contaminating terrestrial land, atmosphere, and water sources.[1] Byproducts from textile industries pollute the environment, especially the water resources, due to the random use of various types of dyes and discharge them to the water sources. Thus, water sources polluted by textile industries contain a variety of organic dyes and chemicals; the chemical composition of these effluents is a major environmental problem.[2] On the other hand, antibiotics are used to treat animal and human diseases. The consumption of these antibiotics leads to their release into the environment after incomplete metabolism. The entering of these compounds into the environment through wastewater from the pharmaceutical industry, human and animal waste deposits, and hospitals causes environmental pollution and is difficult to remove using traditional treatments.[3] Agricultural waste products also cause environmental pollution including water sources. For the development of modern agriculture, pesticides are used. Pesticides and agro wastewater are risks to human health and the aquatic ecosystem.[4]

Moreover, synthetic dyes that are used in the textile industries and agriculture are physically and chemically stable compounds, which enormously affect the environment. Some of these organic pollutants are persistent and identified at a significant level in surface and groundwater, soil, and wastewater effluents.[5] Different conventional techniques such as biological treatment, anaerobic, electrochemical, aerobic, oxidation, adsorption, flotation, reduction, precipitation, and flocculation have been used in wastewater treatment.[6] However, these techniques cannot fully degrade the organic pollutants. On the other hand, we can classify the developed methods to eliminate or reduce organic pollutants into four types:[7–9] (i) physicochemical, which includes membrane bioreactor, adsorption, sedimentation, coagulation, filtration, and flocculation; (ii) chemical treatment, which includes chemical reduction, electrochemistry, advanced oxidation process (AOP), ozone oxidation, enzymes, and photocatalytic degradation; (iii) bioremediation, which includes biological oxidation, and activated sludge; (iv) the combined process. Physicochemical treatment has advantages such as low cost, high treatment efficiency, and easy operation, but its degradation ability is low. Bioremediation can remove organic pollutants from large areas at a very low cost, but it has low efficiency. Chemical treatment has an incredible efficiency to mineralize organic pollutants, but it can cause secondary pollution.

Over the previous decade, researchers around the world made great efforts to develop a more powerful, newer, and promising technique called advanced oxidation process (AOP).[10] The AOP is the most interesting method to remove organic pollutants in wastewater.[11] This method is an alternative to traditional techniques such as adsorption and coagulation because the AOP process mineralizes the organic pollutants rather than moving from place to place. Thus, photocatalysis is a promising AOP and is a green method to decompose organic pollutants nonselectively and quickly from wastewater using semiconductor metal oxides as photocatalyst

Megersa Wodajo Shura was earned his BSc degree in Physics at Asmara University, Eritrea in 1990. After serving at different institutions for a while, he joined Addis Ababa University for his MSc Study in 1997. Then, he joined Adama Teachers College until he moved to Adama Science and Technology University in September 2006. Then, he joined Nelson Mandela University, South Africa for his PhD study in March 2009. Upon completion of his PhD, he returned to ASTU and served as Assistance and Associate Professor of Physics. His research interest is dealing with the various opto-electrical properties of inorganic semiconductors.

Dr Fekadu Gashaw is an Associate Professor of Physics and currently working at Addis Ababa University department of Physics as Researcher and lecturer. He has obtained his first degree in Physics from Debub University in 2001 and his MSc degree from AAU in Laser Spectroscopy (2006). He got his PhD degree from KNUST (Ghana) (2015). Fekadu was also a Postdoctoral researcher at the University of the Free State, (South Africa) from 2016 to 2020. His research mainly focuses on the development and characterization of novel nanomaterials for various applications such as Energy storage and conversion, Gas sensors and Antimicrobial activities. Currently, he is supervising more than ten PhD students.

materials,[12] meaning that for overcoming environmental pollution, the degradation of harmful and toxic contaminant organic compounds using semiconducting photocatalysts is of great significance.[13] A semiconducting photocatalyst is a material that is used as a catalyst in photocatalytic processes. Thus, a catalyst is a material that initiates and enhances the rate of a chemical reaction, but the material that enhances the rate of the chemical reaction remains unchanged at the end of the reaction.[14] In other words, a semiconducting photocatalyst is a material that is capable of harvesting solar light, generating electron–hole pairs that enable transformations of participants of reaction and reproduce its chemical composition after each cycle of such interactions.[15] The catalytic properties of materials under the illumination of either UV or visible light is called photocatalytic activity, and the acceleration of the rate of a chemical reaction by activating a catalyst by light (UV or visible light) is known as photocatalysis.[14] Photocatalysis is a more proficient technique that involves the breakdown or decomposition of different organic pollutants, various dyes, and harmful viruses and fungi using UV or visible light solar spectrum.[16] Photocatalysis was discovered in 1972 during the oil crisis in 1973 and the energy crisis in 1979 for the production of hydrogen production by water splitting.[17] Nowadays, photocatalytic oxidation processes through semiconductor metal oxide nanoparticles are globally accepted and are the most advanced techniques.[18]

After the discovery of photocatalysis technology, researchers have been attracted to understanding the fundamental mechanisms of photocatalysis and improving the photocatalytic properties of the discovered photocatalysts. The photocatalysis technique depends on the reaction between powerful oxidizing and reduction agents (holes and electrons) generated through the illumination of UV or visible solar spectrum on the surface of photocatalyst materials and harmful organic pollutants.[19] Overall, photocatalysis is a process in which the electron–hole pair is generated through the illumination of sunlight to the photocatalyst materials. When the photocatalyst material is exposed to light with energy equal to or greater than the photocatalyst bandgap, the electrons in the valence band (VB) are stimulated and excited to the highest-level conduction band (CB), leaving behind holes in the VB. Generally, the photocatalysis process follows five complementary steps including (i) light harvesting, (ii) electrons–holes generation under the irradiation of light, (iii) charge carrier's separation and moving to the photocatalyst surface, (iv) oxidation and reduction of charge carriers with reactants, and (v) charge carrier recombination on the catalyst surface. The photoinduced electrons and holes reacted with oxygen (O_2), water (H_2O), and hydroxyl groups to generate reactive oxygen species (ROS) such as hydroxyl radicals ($^{\bullet}OH$) and superoxide radical anions ($O_2^{\bullet-}$) with strong oxidation abilities. These ROS are the foremost accountable species for the degradation of persistent organic pollutants in wastewater. These phenomena can be utilized to solve the main problems of our world today in the energy crisis by the process of water splitting to generate hydrogen gas, which is used as fuel, and environmental pollution through the degradation of organic pollutants in wastewater.[20] Thus, the application of photocatalysis is not limited to the degradation of organic pollutants, it is also applied in bacterial disinfectants and for the removal of antibiotics from water. It has great potential in the evolution of hydrogen (H_2) by water splitting as a green energy fuel in the production of hydrocarbon fuel by reducing carbon dioxide (CO_2), and the potential of changing NO and NO_2 into nitrate, which is used as a fertilizer to stimulate the growth of plants.[21–23]

According to researchers' investigations, the nanosized particles show an essential photocatalysis process due to their unique chemical and physical properties, high surface-to-volume ratio, fast dissolution, strong sorption, and high reactivity with respect to their bulk of the same compositions.[24,25] Among these nanosized materials, metal oxide nanoparticles (MONPs) are used as prominent photocatalysts. MONPs have a wide range of applications including environmental remediation, energy storage, electrochemistry, sensors, lubrication, coatings, and other various areas of nanotechnology.[1] Various semiconducting metal oxide photocatalyst materials have been developed to date. Semiconducting metal oxides such as TiO_2, ZnO, SnO_2, Cu_2O, Fe_2O_3, $SrTiO_3$, zinc germanium oxide, bismuth oxides, copper oxides, and WO_3 have got much attention due to their ability in the degradation of various organic pollutants.[13,26] Their effective advantages are attributed to their large surface area, small size, optical and chemical properties, and electrical conductivity properties.[27] However, there are some shortcomings of semiconductor metal oxide photocatalysts such as a small range of the solar spectrum absorption abilities, wide bandgap, and fast recombination rates of photogenerated electrons and holes, which reduce their photocatalytic activities.[20,28] A photocatalyst materials with wide bandgap value requires more energy to be absorbed for charge carrier separation. In addition, the photogenerated electrons and holes could recombine without forming oxidation and reduction, which reduces the photocatalytic activities of these photocatalysts. The fast recombination rate results in a lower number of photogenerated ROS that are available on surface reaction sites to carry out the photodegradation process. Hence, the overall photocatalytic activity is significantly reduced. Many researchers have been working on the modification of photocatalysts or engineering new photocatalysts to address these concerns. The introduction of a heteroatom doping agent into the bulk semiconductor metal oxides modifies the photocatalytic activities of semiconductor metal oxides. Thus, it provides a large dipole moment to change the electron transfer kinetic, and more electrons can be transferred from the valence band to the conduction band of the photocatalyst, hence narrowing the bandgap value.[28,29] The low bandgap value indicates better absorption ability in visible light or natural sunlight. Good photocatalyst materials will now be able to reduce the recombination of photogenerated electron–hole pairs and are able to absorb the visible light range of the solar spectrum. In addition, materials used as photocatalysts should be earth-abundant and cost-effective.

A lead monoxide (PbO) nanoparticle is among the MONPs. PbO and Pb-based oxide material has attracted the researchers' focus due to its exceptional mechanical, optical, and electrical

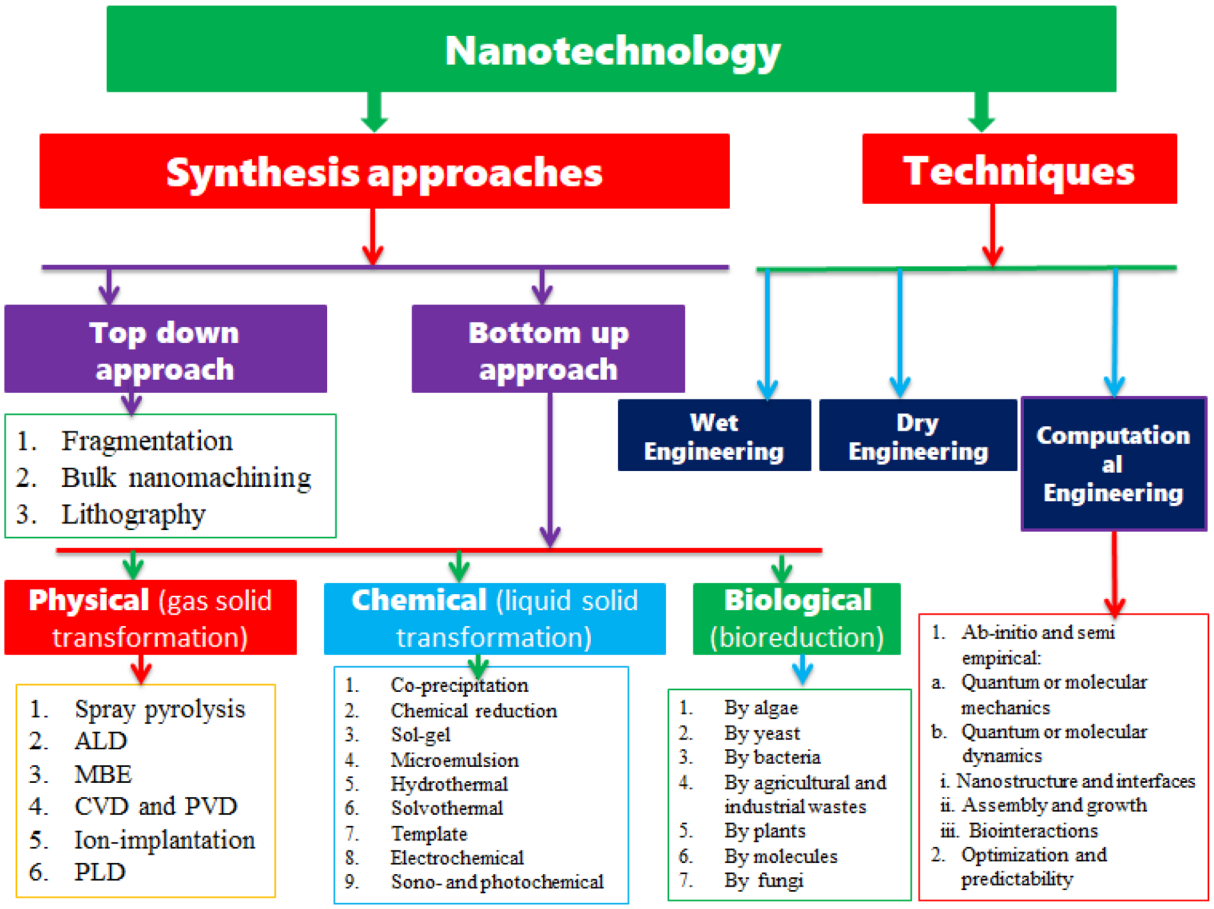

Fig. 1 The major synthesis approaches of MONPs and techniques used in nanotechnology.

properties.[30] The photocatalyst activity of PbO nanoparticles have been investigated for the degradation of organic pollutants.[31–33] However, for the photocatalytic applications of PbO, there are only very few reports, but the coupled PbO with other semiconductors has been widely reported. Thus, the combination of PbO with different metal oxide semiconductors has advantages such as shifting the ultraviolet activity of materials to visible light active by controlling the bandgap and modifying the structure and morphology of the newly formed composite photocatalyst.

Nanotechnology includes both research and engineering of new materials at the nanoscale level. Different synthetic techniques have been used for the synthesis of metal oxide nanoparticles. In this review, the synthesis method for metal oxide nanoparticles, metal oxide studied by density functional theory for photocatalytic applications, applications, and toxicity of different dyes are highlighted. In addition, the photocatalytic applications of metal oxides, challenges in the photocatalytic applications of metal oxides, and strategies to suppress these challenges in metal oxide photocatalysts are described in detail. Previously, many review articles on the photocatalytic applications of metal oxide have been published so far. However, these articles are mainly focused on either applications or challenges and strategies for solving challenges in metal oxide photocatalysts. In addition to this, these articles did not include metal oxide studied both by experimental and DFT methods simultaneously. Therefore, this review has significant advantages in giving way for understanding and studying metal oxide nanoparticles experimentally and computationally. Moreover, the reader can understand easily the drawbacks of metal oxide photocatalysts and the strategically taken action until the present to tackle the abovementioned drawbacks. Therefore, depending on the identified drawbacks, researchers can develop additional strategies to overcome the mentioned drawbacks or design new photocatalysts.

2 Metal oxide nanoparticles

Metal oxide nanoparticles (MONPs) are semiconducting materials that have tremendous applications in different areas of science and technology. Thus, nanosized metal oxides have more imperative physicochemical properties than their bulk of the same composition and have received large attention due to their electronic, catalytic, and magnetic properties.[34] These materials have unique properties such as cold welding, nonlinear, superparamagnetic behavior, higher ductility at elevated temperatures than coarse-grained ceramics, unique catalytic properties, sensitivity, and selective activity that make them indispensable tools in modern nanotechnology.[35,36] In addition, they exhibit fast diffusivity and unique adsorption

properties, which makes them different from their bulk materials of the same compositions.[37] Low density, high surface-to-volume ratio, and quantum properties of nanoparticles are the enchanted properties of nanoparticles.[38,39] More importantly, MONPs have potential applications that attract researchers from the fields of medicine, materials chemistry, materials science, physics, agriculture, electronics, information technology, energy, biomedical, catalysis, sensor, and environment.[40,41] Specifically, MONPs have been attracted for their development of new and effective strategies in environmental remediation and energy production. Among these MONPs, CuO, ZnO, Al_2O_3, Fe_2O_3, ZrO_2, MgO, AgO, SnO_2, TiO_2, CeO_2, PbO, *etc.*, are the most attractive one.[35]

As nanotechnology includes the search for and manufacturing nonexistent materials at the nanoscale level, several synthetic techniques and strategies were successfully used in the development of nanotechnology. In general, there are two types of approaches to the synthesis and fabrication of nanomaterials.[42,43] They are (i) bottom-up approach: this approach includes the miniaturization of materials components up to the atomic level with further self-assembly process (physical forces operating at the nanoscale are used to combine basic units into larger stable structures), leading to the formation of nanostructures. This approach organizes atomic or molecular components to form clusters and then to grow into different morphologies. Quantum dots or nanoparticles formed from colloidal dispersion are examples of a bottom-up approach; (ii) the top-down approach starts from bulk structures to reduce to nanostructured materials.[44]

Nanotechnology techniques can be classified as wet, dry, and computational engineering, as shown in Fig. 1. Wet nanotechnology handles the process, which takes place in a wet environment mostly using living organisms and different components present in the tissue, organs, and cells in living systems. Dry engineering deals with the engineering of different technological applications and it includes (i) electronics, optoelectronic, and photonics; (ii) information processing, storage, and transmission; (iii) food packing and storage; (iv) pigments, protective glasses, textiles; and (v) sensors and energy devices. Computational engineering deals with the development and use of computer-based quantum and molecular design, modeling, and simulation of properties of systems relevant to nanotechnology.[35]

2.1 Synthesis of metal oxide nanoparticles

The strategies for the synthesis of MONPs can be classified into top-down and bottom-up approaches, as shown in Fig. 1. The top-down approach is reducing the large particle size either macro or microparticles to nanosized, whereas the bottom-up approach begins atomic growth up to nanosized particles.[50] As presented in Fig. 1, the top-down approach includes fragmentation, bulk nanomachining, and lithography, whereas the bottom-up approach can be classified into physical, chemical, and biological methods. The physical methods are the process of gas transformation to solids. The physical methods under the bottom-up approaches for the synthesis of nanoparticles include spray pyrolysis, atomic layer deposition (ALD), molecular beam epitaxy (MBE), chemical vapor deposition (CVD), physical and pulse vapor deposition (PVD), and ion implantation, and the biological method is a green synthesis method of nanoparticles by extracting from algae, yeast, bacteria, agricultural and industrial wastes, plants, molecules, fungi, *etc.* The chemical methods for nanoparticle synthesis include coprecipitations, chemical reduction, sol–gel, microemulsion, hydro and solvothermal, template, electrochemical, and sono and photochemical. In this review, we only reviewed some of the chemical synthetic methods that are widely used for the synthesis of metal oxide nanoparticles.

2.1.1 Sol–gel process. The sol–gel process is a simple, eco-friendly, and inexpensive method that enables to control the high purity and homogeneity of the final metal oxide nanoparticles product and also to control the size and growth of particles and supports the addition of large concentrations of doping agents.[51] The sol–gel process is used to prepare a high-quality metal oxide nanoparticle and metal oxide nanocomposite, which is done by the hydrolysis process of metal alkoxides dissolved in alcohol or water. From this, the corresponding hydroxide has resulted. Thereafter, by the condensation of the formed hydroxide, a metal hydroxide polymer is formed in a densely packed gel form. To obtain the metal oxide powder of the targeted particle size, the formed gel is heated and dried. Generally, the sol–gel process steps are (i) hydrolysis, (ii) polycondensation, (iii) aging, (iv) drying, and (v) thermal decomposition.[45,52] The finally heated and dried have the possibility to give us metal oxide in a form of bulk materials, nanoparticles, or oxygen vacancy based on the heat-treatment process done.[28] A variety of metal oxide nanoparticles such as ZnO,[53] TiO_2,[54] MgO,[55] ZrO_2,[56] CuO,[57] and Nb_2O_5/SiO_2 (ref. 58) were synthesized by the sol–gel process. For example, Patel *et al.*[59] reported the synthesized CuO and ZnO by the sol–gel process using copper(II) nitrate and zinc nitrate as starting materials, respectively. The advantages and disadvantages of the sol–gel method is summarized in Table 1.

2.1.2 Coprecipitation. In the synthesis of metal oxide nanoparticles using the coprecipitation process, the reaction takes place at ambient temperature. In this method, a solution of metal salt and a precipitating media produces a precipitated oxo-hydroxide in a solvent. KOH, NaOH, and ammonia solutions are commonly used as precipitating media. Thus, the alkaline nature and pH of the solution highly influence the properties and morphologies of metal oxide nanoparticles. To come up with the desired morphology and properties of metal oxide nanoparticles, the amount, rate, and mode of alkali solution added to the reaction mixture must be added. By adding surfactants, it is possible to narrow the size of the produced nanoparticles as surfactants are very useful and crucial in the tailoring of surface characteristics of metal oxide nanoparticles. This method is the highly used synthesis method for metal oxide nanoparticles due to its simplicity, low cost, scale-up, and low-temperature reaction rates. It is also possible to control the particle size and crystal structure by varying media pH and, at times, large amounts of nanoparticles can be prepared using the coprecipitation method.[62] Various metal

oxide nanoparticles such as MnO_2,[63] ZnO,[64] MgO,[65] $BiVO_4$,[66] Ni-doped SnO_2,[67] N- and Fe-doped TiO_2,[68] CuO,[69] Cu-doped ZnO,[70] $PbWO_4$,[71] *etc.*, were synthesized using the coprecipitation method. Kotresh *et al.*[64] synthesized ZnO nanoparticles *via* the coprecipitation process at 50 °C and 70 °C reaction temperatures using sodium hydroxide as the precipitating media and zinc nitrate hexahydrate as the Zn^{2+} precursor. Buraso *et al.*[72] also used the same synthesizing approach for the preparation of TiO_2 using titanium(IV) isopropoxide as a precursor. Rangel *et al.*[73] used the coprecipitation method to synthesize CuO nanoparticles using copper chloride and copper sulfate as a precursor. Coprecipitation method has advantages and disadvantages in metal oxide synthesis, as given in Table 2.

2.1.3 Hydrothermal synthesis. Hydrothermal synthesis is a solution reaction-based method, and the process is called hydrothermal because water is used as a solvent, whereas in solvothermal synthesis, organic solvents are used. In this method, a wide range of temperature and pressure (above ambient temperature and pressure) is used for the formation of nanoparticles. By controlling the reaction pressure, the morphology of the prepared nanoparticles can be controlled either by decreasing or increasing the pressure conditions. In this method, the aqueous mixture is heated in a sealed stainless-steel autoclave above the water boiling point and increasing pressure in the reaction above the atmospheric pressure. This method has significant advantages over other synthesis approaches. It can generate nanoparticles that cannot be prepared at low temperatures or room temperature, and it can also produce nanoparticles if the materials have a high vapor pressure.[74] During the reaction in an autoclave, the particles can be agglomerated. To prevent the agglomeration of the particles, it is necessary to use a suitable stabilizer or capping agent. Several metal oxide nanoparticles such as SnO_2,[75] TiO_2,[76] Fe_2O_3,[77] NiO,[78] and $BiVO_4$ (ref. 79) were prepared using the hydrothermal synthesis process. Bade *et al.*[80] prepared copper oxide nanoparticles using copper sulfate pentahydrate as a precursor and NaOH as the stabilizing agent *via* hydrothermal synthesis. Suthakaran *et al.*[81] reported high-quality SnO_2 nanoparticles synthesized by hydrothermal synthesis, and they studied the photocatalytic activity of these nanoparticles by degrading methyl violet dye. The advantage and disadvantage of the hydrothermal synthesis method is summarized in Table 3.

2.1.4 Microemulsion. Stankic *et al.*[85] reviewed the microemulsion method consisting of oil and water immiscible phases. These immiscible phases are separated by surfactant molecules, creating an oil/surfactant and water surfactant binary system. The surfactant molecules have properties of a hydrophobic tail, which is dissolved in the oil phase and a hydrophilic head, which is grouped to the water phase. To synthesize the homogenized phase, proper amounts of metallic precursor, surfactant, water, and oil are mixed while stirring at

Table 1 Advantages and disadvantages of the sol–gel synthesis method

Synthesis methods	Advantages	Disadvantages	Ref.
Sol–gel	• Easy to perform in the laboratory • Inexpensive and high yield • Synthesis is at low temperature • Produce high-quality materials • High scale homogeneity and purity • Doping of different elements can be controlled • Atomic level mixing components (precursors) • High purity and proper stoichiometry can be achieved • Desired shape and length can be obtained • Precise control of size and structure • Materials can be obtained in bulk, thin film, or nanopowders • Can produce coating to provide protection against corrosion • Homogenous and high adhesion products of thin films • Synthesis of uniform compounds in the form of composite oxides	• Use of organic solution that can cause toxicity • Sensitivity to moisture • Includes many steps and the process takes a long time • Dimensions and volume changes during different steps • Product contains sol–gel matrix components • Metal alkoxides are almost expensive • Residual carbon and hydroxyl groups	45–47

Table 2 Advantages and disadvantages of the coprecipitation synthesis method

Synthesis methods	Advantages	Disadvantages	Ref.
Coprecipitation	• Low cost and environment-friendly • Simple synthesis • High product • Simple and efficient • Fast reaction • Well dispersed in polar solution • Easily scale up the production	• Wide particle size distribution • Wide particle size distribution, poor crystallinity, and aggregation • Surface oxidation • Poor reproducibility • Limited by the boiling point of water	46, 48 and 49

room temperature. For the precipitation of nanoparticles, oxidizing agent, reducing agent, and precipitating agent are added while stirring vigorously and thereafter, followed by centrifugation; subsequently, washing and drying or annealing takes place. The shape and size of metal oxide nanoparticles synthesized by this method can be easily manipulated. Different metal oxide nanoparticles such as Fe_2O_3,[86] CeO_2,[87] NiO,[88] ZnO,[89] TiO_2,[90] and CuO[91] were synthesized using the microemulsion method. In metal oxide synthesis, the microemulsion has advantages and disadvantages, as summarized in Table 4.

2.1.5 Sonochemical synthesis. The sonochemical method uses ultrasound to facilitate the chemical reaction in which the ultrasound induces a chemical effect on the reaction process. In sonochemical synthesis, a starting material is dissolved in a solvent to get a solution. Thereafter, the resulting solution is irradiated with ultrasonic waves with a frequency above 20 kHz. Ultrasonic irradiation causes acoustic cavitation, which leads to the formation, growth, and implosive collapse of bubbles in a liquid.[85] The implosive collapse of millions of bubbles in the liquid generates extremely high energy (temperature 5000 K and pressure 20 MPa) and is subsequently released, thereby heating the solution. In general, for metal oxide preparation, we follow three steps: (i) formation of metal hydroxide precursor's precipitate, (ii) ultrasonic irradiation, and (iii) transformation to metal oxide nanoparticles through heat treatment. The rate at which the solution is cooled affects the crystal shape and morphology of the resulting metal oxide nanoparticles. This method is advantageous as it is rapid, nonhazardous, and it

Table 3 Advantages and disadvantages of hydrothermal synthesis method

Synthesis methods	Advantages	Disadvantages	Ref.
Hydrothermal	• Able to synthesize materials that are unstable near melting point • Ability to synthesize high quality products • Environment-friendly and versatile • Simple, easy, and inexpensive synthesis method • The morphology of products can be changed easily • Easy to control particle size, shape, and dispersion • Production of high quality of 1D nanostructures such as nanorod • Good crystallization • Magnetic controllability • Reactants have elevated reactivity • Scalable	• High cost of equipment such as autoclave • Safety issues during the reaction process • Impossibility of observing the reaction process • The reaction takes a long time • High reaction temperature • High pressure • Usually, polydisperse samples are obtained • Harsh reaction conditions • Adsorption of capping agents	46, 47, 49 and 60

Table 4 Advantages and disadvantages of the microemulsion synthesis method

Synthesis methods	Advantages	Disadvantages	Ref.
Microemulsion	• Easy and do not require energy during synthesis • Better thermodynamic stability • Low viscosity • Uniform properties • Narrow pore size distribution • Homogeneous particle size distribution and good control of shape • Increase the rate of absorption • Increase bioavailability • Helpful in taste masking • Eliminates variability in absorption	• Large amounts surfactants required, poor yield, and time consuming • Surfactants are difficult to remove • For substances with high melting points limited solubility capacity • Difficulty in scale up produces • Microemulsion stability is influenced by parameters such as temperature and pH	46, 49 and 61

Table 5 Advantages and disadvantages of the sonochemical synthesis method

Synthesis methods	Advantages	Disadvantages	Ref.
Sonochemical	• Improves the reaction rates and selectivity	• The rate of sonochemical reduction completely depends on the ultrasonic frequency	46, 47, 82–84
	• Less toxic compounds and environmentally safe solvents are used	• Extensions of problems	
	• Reduction in the energy use for chemical transformations	• Inefficient energy	
	• Reusability of materials	• Low yield	
	• Reduced number of reaction steps		
	• Successfully employed for less volatile organic liquids		

produces metal oxide nanoparticles of high surface area, uniform size, and high purity products. In addition to this, the sonochemical method is a low-cost process and also produces small particle sizes.[84] Various metal oxide nanoparticles such as TiO_2,[92] Cu-doped CeO_2,[93] La-doped CeO_2,[94] ZnO,[95] Zn_2SnO_4–V_2O_5 nanocomposite,[96] MoO_3,[97] Ag-$PbMoO_4$,[98] Co- and Mn-codoped W_3O_8,[99] and Cu_2O[16] were produced using this method. Hassanjani-Roshan *et al.*[100] prepared iron oxide nanoparticles using the sonochemical method, and they argued that the morphology and the size of the final product were influenced by the parameters such as power of ultrasonication, temperature, and sonication time. Noman *et al.*[95] reported the successfully prepared ZnO nanoparticle by the sonochemical process for photocatalytic applications. The advantages and disadvantages of the sonochemical method are summarized in Table 5.

2.2 Dyes

Dyes are used for the coloration of several materials such as textile fibers, cosmetics, paper, food, tannery, leather, and pharmaceutical products.[8] Generally, dyes can be classified as natural and synthetic. Natural dyes are the naturally existing dyes originating from plant parts including leaves, berries, wood, fungi, lichens, and bark, while synthetic dyes are man-made dyes synthesized from chemicals, petroleum derivatives, and earth minerals.[101] Various synthetic dyes and their applications are presented in Fig. 2. These dyes are mostly used in food and beverages, printing, textile industries, and pharmaceuticals. The textile industry is the main contributor to the dyes released into the environment. The annually worldwide fabricated dyes are about 7×10^7 tons and over 10 000 different types of dyes are used by textile industries.[9] The azo dye aniline yellow dye is used in textile industries in the production of nylon and silk. The acid dye acid blue is used in the production of cosmetics, wool, and leather. The reactive dye reactive red 198 is applied in the production of nylon, silk, and wool. The sulfur dye thiazine is used in the fabrication of paper, silk, and cotton. The mordant dye mordant red 11 is used in the production of anodized aluminum and wool. The direct dye direct yellow 11 is applied in the fabrication of paper, cotton, and leather. The disperse dye disperse red 60 is used in the production of plastic, polyamide, and nylon. A basic dye, methylene blue is used in inks and medicines.

These dyes are used as coloration in textile industries and discharging textile industry wastewater into water bodies is not important as the color prevents reoxygenation in receiving water by cutting off the penetration of sunlight. These organic dyes have a complex structure and can produce aromatic amines as they are released into the environment. These carcinogens and hazardous dyes resist the sunlight entering into the water bodies, resulting in influencing the natural aquatic processes such as biodegradable and photosynthesis.[102] When they are released into the environment, they cause environmental pollution and are highly toxic to aquatic life, microorganisms, and human beings as they are mutagenic and carcinogenic.[10] Dyes found in wastewater discharge or dust produced in the textile industry pose a serious health concern to human beings, as presented in Fig. 3. These dyes affect our body systems such as the immune, respiratory, and reproductive and also affect vital organs including the heart, liver, kidney, and brain.[8] They cause diseases either directly *via* inhalation such as nausea, respiratory problems, allergy, asthma, dermatitis, and eye or skin irritation, or indirectly *via* the food chain including tuberculosis, gene mutations, cancer, heart disease, and hemorrhage.

2.2.1 Toxicity of methylene blue. The fabrication of synthetic dyes is a way to increasing due to their highly demanded in the textile and clothing industries. In addition to the aforementioned dyes, dyes such as crystal violet, aniline blue, basic fuchsin, congo red, toluidine blue, and methylene blue are also a few examples of synthetic dyes. These synthetic dyes remain in the environment when they are directly or indirectly released into the environment because most of them are nonbiodegradable and are not completely removed during conventional water treatment. Thus, they persist in the environment because of their high stability to light, temperature, water, and other substance such as detergent and soap.[103] Effluents from textiles and factories using dyes release highly colored dyes, which can damage the aquatic environment.[104] Dye molecules may resist sunlight penetration into the water bodies, thereby inhibiting natural photosynthesis.

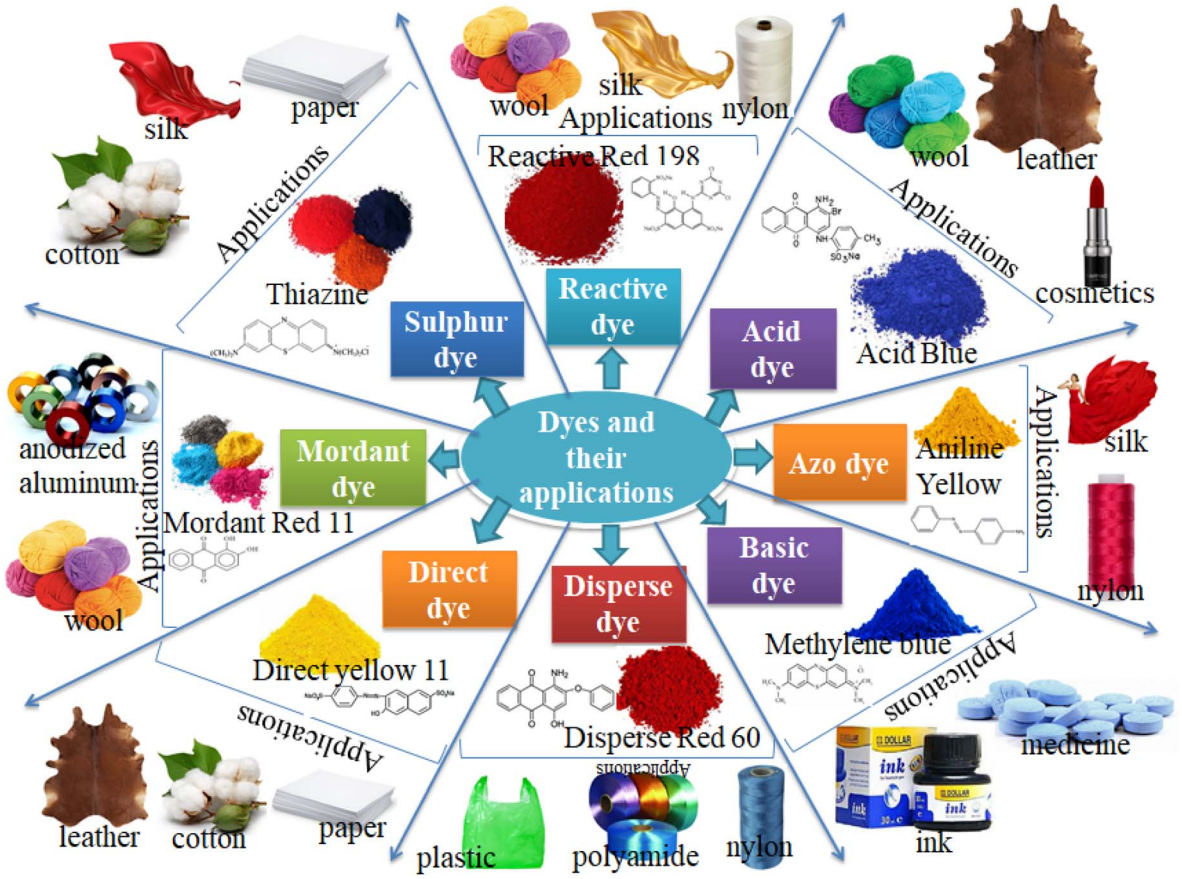

Fig. 2 Different types of dyes and their applications in industries (colors online).

Methylene blue (MB) is applied in huge amounts as a colorant for silk, paper, cotton, and wool. In addition to these, cosmetics, food, and pharmaceutical industries consume large amounts of MB dye in their fabrications.[105] MB is a cationic dye and a heterocyclic aromatic compound with a planar structure.[103,106] It has $C_{16}H_{18}N_3SCl$ chemical formula with a molecular weight of 319.85 g mol^{-1}. MB is highly soluble in water and forms a stable solution at room temperature. MB is a class of phenothiazine with an International Union of Pure and Applied Chemistry (IUPAC) name [3,7-bis(dimethylamino) phenothiazine chloride tetramethylthionine chloride] with color index (CI) 52 015.[107,108] MB is nonbiodegradable and carcinogenic, having characteristic stability of the aromatic ring molecular structure, as presented in Fig. 4. When released partially or without treating, the MB dye-contaminated wastewater from any of the industries that used MB dye could cause a lot of human health risks, such as vomiting, increased heart rate, Heinz body formation, shock, quadriplegia, cyanosis, jaundice, and tissue necrosis in human beings.[109] The health risks associated with the discharge of untreated MB-loaded wastewater includes respiratory disorder, genitourinary complications, gastrointestinal complications, cardiovascular issues, central nervous system, and dermatological effects, which are also included.[110] The discharge of MB dye wastewater into the environment also causes risks such as reduction of pigment, growth inhibition, and protein content of microalgae *Spirulina platensi* and *Chlorella vulgaris* in plants.[104] Moreover, the discharge of untreated MB dye-loaded water to either groundwater or surface water recently has caused a shortage of clean water in society. Commonly, developing countries release large amounts of MB dye-loaded wastewater into the physical environment without efficient and effective management.[111]

In addition, it is known that MB is commonly an inert dye, but it acts as a potent reversible monoamine oxidase (MAO) inhibitor (MAOI), which makes it difficult to find applications in medicine by ameliorating a clinical condition known as hypotension and improving hyperdynamic and hypoxia circulation in liver cirrhosis and severe hepatopulmonary syndrome.[103,112,113] However, if infused intravenously at a dosage higher than the recommended concentration, MAOI may precipitate serious serotonin toxicity.[113,114] Serotonin toxicity, also called serotonin syndrome, is a deadly disorder that is linked to elevated serotonergic activity in the spinal cord and brain.[112] Also, skin-contacting MB using improperly or untreated MB-loaded water causes redness, itching, and skin necrosis, which causes the death of cells in tissues and organs.[115] Generally, the discharge of MB-loaded wastewater from any utilization causes devastating effects on the

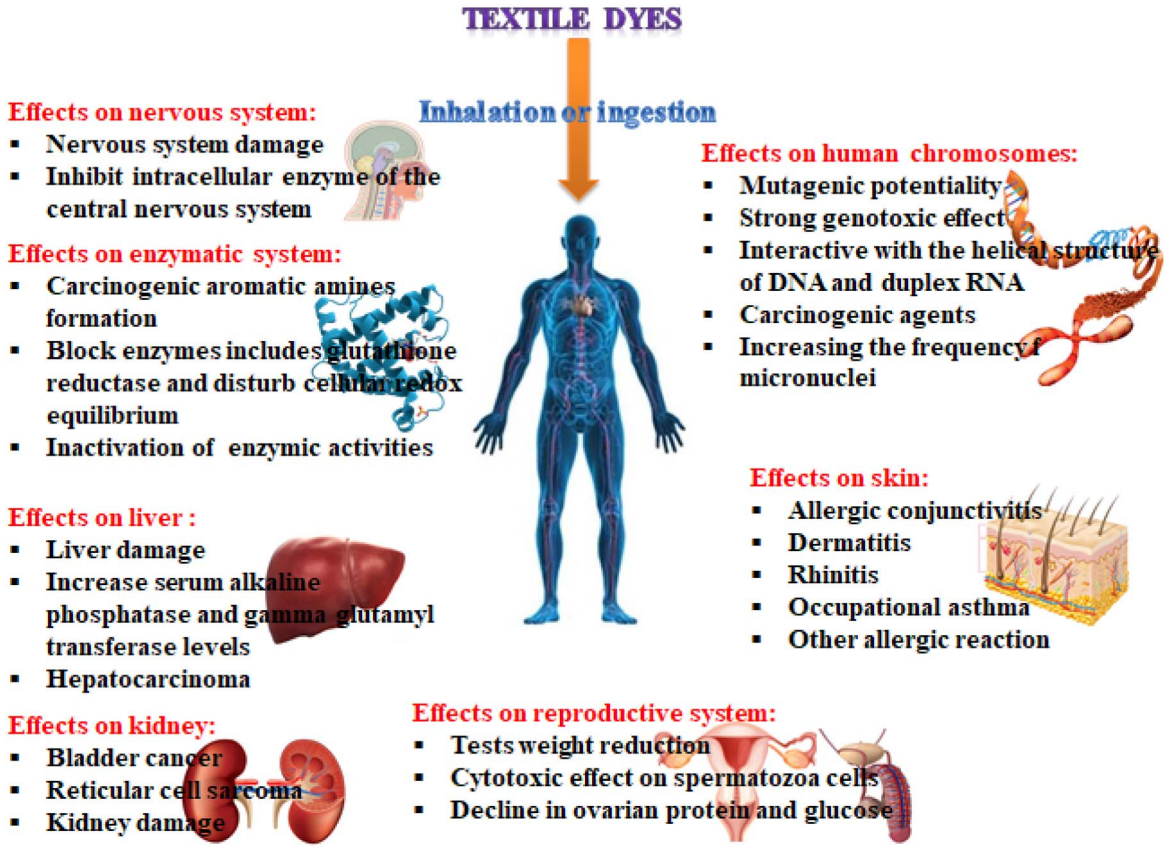

Fig. 3 Negative effects of textile dyes on human health on different parts of the body (colors online).

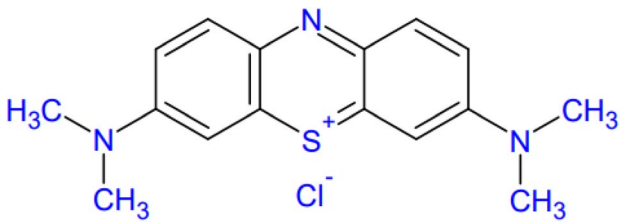

Fig. 4 Molecular structure of Methylene Blue.

environment. Therefore, it shall be removed or degraded before being exposed to the environment. However, it cannot easily be removed by a traditional treatment because of its non-biodegradability and persistence. The photocatalytic mechanism is the most effective way to degrade these dyes.

2.3 Photocatalytic applications of metal oxides

Various metal oxides are used as photocatalysts in photocatalysis technology. Photocatalysis is potentially applied in fields including (i) photodegradation of organic pollutants, (ii) for hydrogen evolution by water splitting, and (iii) photoreduction of CO_2 into renewable fuels such as CH_4 and CH_3OH.[116] Metal oxide nanoparticles have been used in different areas including the removal of heavy metals, poisonous gas sensing, energy conversation and storage, biomedical, and photocatalytic removal of organic pollutants. In this review paper, we only overview the applications of different metal oxide nanoparticles in photocatalysis technology and we start our discussion with the mechanisms of photocatalysis.

2.3.1 General mechanism of photocatalysis. Photocatalysis is a chemical reaction that triggers or accelerates the specific reduction and oxidation (redox) reactions with the irradiated semiconductors.[116] The major reactions involved in photodegradation are listed in eqn (1)–(5). The mechanism of photocatalytic degradation takes place with three general processes: (i) charge separation (hole and electron separation) under light irradiation, when the irradiated light match or exceeds the bandgap of the photocatalyst; (ii) distribution of charge carriers to the photocatalysis surface (MONPs); (iii) oxidation and reduction takes place on the surface of the photocatalyst.[22] The process starts from the light adsorption of the photocatalyst by a certain wavelength when the light falls on the surface of the photocatalyst, which results in the excitation of electrons (e^-) from the valence band (VB) to the conduction band (CB), leaving holes (h^+) in the valence band, as shown in eqn (1).[1,117] When the photocatalyst materials came in contact with organic pollutants, the holes created in the valence band split water molecules or react with OH^- by resulting in hydroxyl free radical $^{\bullet}OH$, as shown in eqn (2),[117] while the electrons (e^-) excited to the conduction band react with O_2 to create super oxygen radical $O_2^{\bullet-}$ species, as shown in eqn (3).[118] Both $^{\bullet}OH$ and $O_2^{\bullet-}$ are

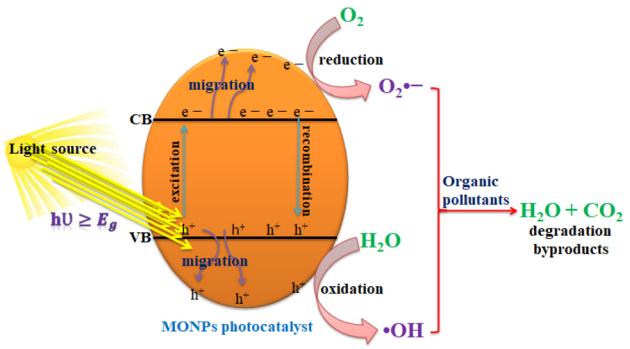

Fig. 5 Schematic diagram of photocatalysis reaction mechanisms.

highly reactive species and they react with organic pollutants adsorbed/absorbed on the surface of the photocatalyst materials by degrading these pollutants or reducing them into H_2O and CO_2, as shown in eqn (5). The general photodegradation mechanism of photocatalysis is presented in Fig. 5.

$$\text{MONP} + h\nu \rightarrow (\text{MONP})(h^+)_{VB} + (\text{MONP})(e^-)_{CB} \quad (1)$$

$$(\text{MONP})(h^+)_{VB} + H_2O \rightarrow H^+ + {}^{\cdot}OH \quad (2)$$

$$(\text{MONP})(e^-)_{CB} + O_2 \rightarrow O_2^{\cdot -} \quad (3)$$

$$(\text{MONP})(e^-)_{CB} + O_2^{\cdot -} + 2H^+ \rightarrow {}^{\cdot}OH + OH^- \quad (4)$$

$$\text{pollutants} + {}^{\cdot}OH \rightarrow \text{degradation byproducts } (CO_2 + H_2O) \quad (5)$$

Oxidation and reduction:[1]

$$\text{organic pollutants} + \text{photocatalyst } (\text{MONP}(h^+)_{VB}) \rightarrow \text{oxidation products} \quad (6)$$

$$\text{organic pollutants} + \text{photocatalyst } (\text{MONP}(e^-)_{CB}) \rightarrow \text{reduction products} \quad (7)$$

The photocatalytic reaction takes place at ambient temperature and pressure without the production of additional sludge and a significant reduction of catalyst. The excited electrons are produced with strong reducibility while holes in the valence band with strong oxidability together result in the formation of the oxidation–reduction or shortly redox generated on the surface of the photocatalyst. The redox reaction takes place on the photocatalyst surface as the photogenerated electrons and holes are scattered on the surface of the photocatalyst. The oxidation reaction takes place by the cathode holes in the valence band reacting with the moisture on the surface of the photocatalyst to create the hydroxyl radicals. If oxygen is delivered from the outside to the photocatalytic reactor, it acts as an electron acceptor and delays the rate of charge recombination.

In semiconductor metal oxides, when the conduction band electrons possess a chemical potential of +0.5 to −1.5 V *versus* normal hydrogen electrode (NHE), then they act as reductants, while the valence band holes possess a strong oxidative potential of +1.0 to +3.5 V *versus* NHE.[116,119] Thus, for a semiconductor to be photochemically active as a photocatalyst for the generation of ˙OH radicals, the redox potential of the photoinduced valence band hole must be sufficiently positive, whereas the redox potential of the photoinduced conduction band electrons must be sufficiently negative for the reduction of the adsorbed O_2 to superoxide.[120]

There are constraints to the photocatalytic mechanism. Only the photons with energy equal or larger than the bandgap of the photocatalyst are used in the target reaction. Thus, the optimization and tuning of the bandgap is required to achieve high efficiency of the photocatalyst. Another main challenge in the processes of photodegradation of photocatalysis is the rapid recombination of charges (electron–hole pair's recombination) in photocatalysts without forming free radicals. To solve these challenges, many interesting options such as the manipulation of experimental conditions, producing low bandgap photocatalyst, and modification of the discovered photocatalyst are among the strategies undertaken to overcome these challenges.

2.3.2 Performance evaluation of a photocatalyst. Photocatalyst performance can be measured by the degradation of concentrations in liquids. The degradation efficiency of the photocatalyst can be calculated by eqn (8)[121]

$$\text{degradation efficiency} = (C_0 - C)/C_0 \times 100 \quad (8)$$

where C_0 is the concentration of the dye before light irradiation and C is the concentration after a certain light illumination time.[122] The Beer–Lambert law given by $A = \varepsilon cd$ is used to calculate the concentration of the organic compound in the liquid, where A is the absorbance, ε is the molar extinction coefficient, c is the absorber concentration of the absorbing species, and d is the optical path length.[123]

The kinetic model, the Langmuir–Hinshelwood model, is used to evaluate the performance of the photocatalytic reaction occurring in the solid–liquid interface.[124,125] The concentration of the organic pollutant, reaction parameters, temperature, and light irradiation intensity can be covered within the frame of the Langmuir–Hinshelwood model. For the first-order reaction, the Langmuir–Hinshelwood model is given as

$$dC/dt = kC \quad (9)$$

where C is the concentration, t is the respective time, and k is the rate constant. From the first-order plot, the rate constant can be calculated according to the equation[121]

$$\ln(C/C_0) = -kt \quad (10)$$

where k is the apparent first-order rate constant given by the slope of the graph of $\ln C_0/C$ *versus* t.

2.3.3 Challenges in photocatalysis. The photocatalytic activity of the photocatalyst highly depends on its optical, crystallinity, structure, surface chemistry, and electronics. However, substantial challenges such as the high cost of semiconductors, lower solar energy utilization rate, and rapid recombination of photogenerated electron–hole pairs limit its potential applications in small-scale environmental areas.[126]

The stability, photocorrosion, and availability are also the challenges.[127] The main challenge for the photocatalytic performance is associated with its semiconductor metal oxides including the mismatch of solar spectrum and bandgap of metal oxides, materials instability, and inefficient separation and transport of charges. The incident photon absorption efficiency of the photocatalyst is determined by its bandgap. Thus, most of the discovered photocatalysts such as TiO_2 and ZnO have a wide bandgap, which made then active only under the ultraviolet region of the solar spectrum. The solar spectrum consists of 5% UV, 45% visible, and 50% infrared (IR), which means that UV is expensive and limits the wide applications in different areas. Therefore, bandgap tailoring is the fundamental challenge in photocatalysts to be solved. The recombination of photogenerated electron–hole pairs is another key issue influencing the photocatalytic activity of metal oxides. The recombination can occur either in the bulk or on the catalyst surface by dissipating energy as nonradiative (heat) or radiative (light) reducing the photocatalytic activity. The low surface chemistry also influences the photocatalytic activity of semiconductor metal oxides. In the photocatalytic reaction, the surface energy plays a great role in transferring electrons between the reactants. Various article reviews are reported on the strategies to develop a novel and high performance photocatalysts. Recently, Ahmad *et al.*[128] reviewed on the most effective strategies for overcoming the shortcoming of photocatalysts to enhance their applications in pollutant degradation, CO_2 reduction, H_2 evolution, and N_2 fixation. The strategies to suppress these challenges are described in detail in the next sections.

2.3.4 Doping in metal oxide nanoparticles. Doping is adding or substituting foreign elements either metals or nonmetals into parent elements, which can induce changes in the electronic and crystal structure of the parent oxide.[129] Doping into host semiconductors is one of the most effective methods to manipulate the electronic structures, thus separating the charges efficiently.[22] The main advantage of doping is to tune the bandgap of parent oxides either by increasing or decreasing the bandgap of metal oxides. Nonmetal dopants are fluorine, nitrogen, chlorine, carbon, iodine, phosphorus, selenium, sulfur, and tellurium, which are commonly used as dopants in metal oxides. These dopants can substitute in the site of oxygen or can exist as interstitial dopants.[50] The contribution of orbital states of these dopants creates mixed or localized states at the edges of the valence band and/or conduction band edges, which cause the narrowing of the bandgap of metal oxides and subsequently enhance the visible light activity of metal oxides.[130] A foreign dopant can also create an additional dopant impurity level at the middle of the bandgap, which initiates new excitations and increases the concentrations of photogenerated electrons and holes.[131] The added or substituted impurity can also lead to the formation of defects, which can trigger new optical characteristics. Moreover, in photocatalytic applications, they can create an additional trapping state, which suppresses the rapid charge recombination and increases the lifetime of charge carriers.[132] Metal dopants such as alkaline earth metals, transition metals, rare earth metals, and post-transition metals can also be used in the bandgap engineering of metal oxides.[50,133,134] Metal ion dopants have the advantage of inducing defects and changing the diffusion behaviors, which can improve the electron mobilities and charge transport, thus enhancing the electrical properties.[19,50] Metal doping can also activate the surface of the photocatalyst to boost the reaction. Generally, metal doping has advantages such as improving the mobility rate of the electron–hole pairs, formation of new energy states either inside or beyond the bandgap of host semiconductor metal oxides, and enhancing the visible light adsorption by the red-shifting of the adsorption edge.[19]

2.4 Metal oxides in photocatalytic degradation

A huge number of semiconductor metal oxide nanoparticles have been discovered for the degradation of pollutants in wastewater and air for a green and suitable environment. Among these metal oxides, TiO_2 is the foremost discovered photocatalyst, which attracted many researchers around the world to engineer new photocatalyst materials. Thus, after the discovery of TiO_2 in 1972, many other metal oxides are discovered for photocatalytic applications. Photocatalysts are generally divided into two main categories: (i) homogeneous catalysts and (ii) heterogeneous catalysts. When a catalyst is present in the same phase as that of the reagents, it is defined as homogeneous, which means that the catalysts are present as solutes in a homogeneous catalytic reaction system. In contrast, a catalyst is said to be heterogeneous if it is present in a different phase in the reaction mixture.[14] In heterogeneous photocatalysis, the photocatalyst acts as an active surface for the reaction or mineralizing of organic pollutants by generating free radicals, which are capable of the complete mineralization of organic pollutants through complex mechanisms.[5] In this section, we have overviewed the commonly used metal oxide nanoparticles in photocatalysis technology.

2.4.1 TiO_2 photocatalyst. Titanium dioxide (TiO_2) is the leading photocatalytic material since its discovery in 1972 due to its low cost, corrosion resistance, strong oxidizing power, and photochemical and chemical stability. TiO_2 is an n-type semiconductor metal oxide and it has the capability of oxidizing organic pollutants into nonhazardous products completely.[135,136] Despite its high performance in the photocatalytic degradation of polluted air and wastewater pollutants, its photocatalytic activities are limited due to the rapid recombination of the photogenerated electron and hole pairs, poor sensitivity to visible solar radiation because of its wide bandgap, and TiO_2 particles aggregated when produced in nanoparticle form, which blocks the active sites to adsorb/absorb pollutants that hinders its activity in photocatalysis technology.[28]

Many researchers are interested in overcoming these challenges by taking different options to improve the photocatalytic activity of TiO_2 nanoparticles. To enhance its poor sensitivity to the visible light region, it is important to reduce the bandgap and decrease the rate of charge recombination to improve its lifetime for photocatalytic applications. Researchers have proposed a strategic approach to address these challenges. The well-studied and sufficient approach is metal-ion doping, which

introduces additional energy levels and reduces the bandgap. Metal-ion doping also introduces a charge-trapping site, which decreases the rapid recombination of photogenerated electron and hole pairs. Different metal-ion doped TiO_2 is extensively studied with the advantage of increasing its absorption spectrum in visible light because the visible light region of the solar spectrum is freely available everywhere. Miyamoto *et al.*[135] synthesized lutetium(III) ion-doped TiO_2 by the sol–gel method to modify the photocatalytic performance of TiO_2 for the photocatalytic degradation of adenosine 5′-triphosphate (ATP) under UV irradiation. Their result showed that the lutetium(III) ion-doped TiO_2 nanoparticles indicated higher photoreactivity than undoped TiO_2. Garza-Arévalo *et al.*[137] synthesized Fe-doped TiO_2 by the sol–gel method and evaluated the removal of arsenic(III) from groundwater under visible light. The incorporation of Fento TiO_2 extends the absorption of TiO_2 to visible light region, and induces oxygen vacancies, which initiate the photocatalytic oxidation of arsenic(III) and retarded the fast recombination of photogenerated electrons and holes. Ndabankulu *et al.*[12] reported different lanthanides (Ce, Dy, Lu, and Sm)-doped TiO_2 by the sol–gel process and evaluated the photocatalytic activity and efficacy of four different lanthanides-doped TiO_2 for the degradation of caffeine under visible light irradiation. Sood *et al.*[18] reported iron(III)-doped TiO_2 nanoparticle photocatalyst synthesized by the hydrothermal method and examined its photocatalytic activity under the illumination of visible light spectrum using *para*-nitrophenol as a model pollutant. The maximum degradation they obtained was 92% in 5 h with 0.05 mol% Fe^{3+}, which was attributed to the high crystalline structure, small size, maximum charge separation, retarded electron–hole recombination, and better visible light response of the prepared Fe^{3+}-doped nanoparticle. Xie *et al.*[138] reported Se^{4+}-doped TiO_2 nanoparticles synthesized by the sol–gel method for the degradation of rhodamine B under visible light irradiation. Se^{4+} introduces extra electronic states in the bandgap of TiO_2 and narrowed the bandgap of TiO_2, as presented in Fig. 6a. The smallest bandgap they obtained was 2.17 eV and due to the extended absorption range, the photocatalytic activity of TiO_2 was improved. However, as the percentage concentration of Se^{4+} increased to 25%, the bandgap started to increase; hence, the photocatalytic activity also decreased.

Depositing noble metals such as Ag, Pd, Au, and Pt on the surface of TiO_2 retards the fast recombination of photogenerated electron–hole pairs. Narkbuakaew and Sujaridworakun reported the Ag metal deposited on the surface of anatase

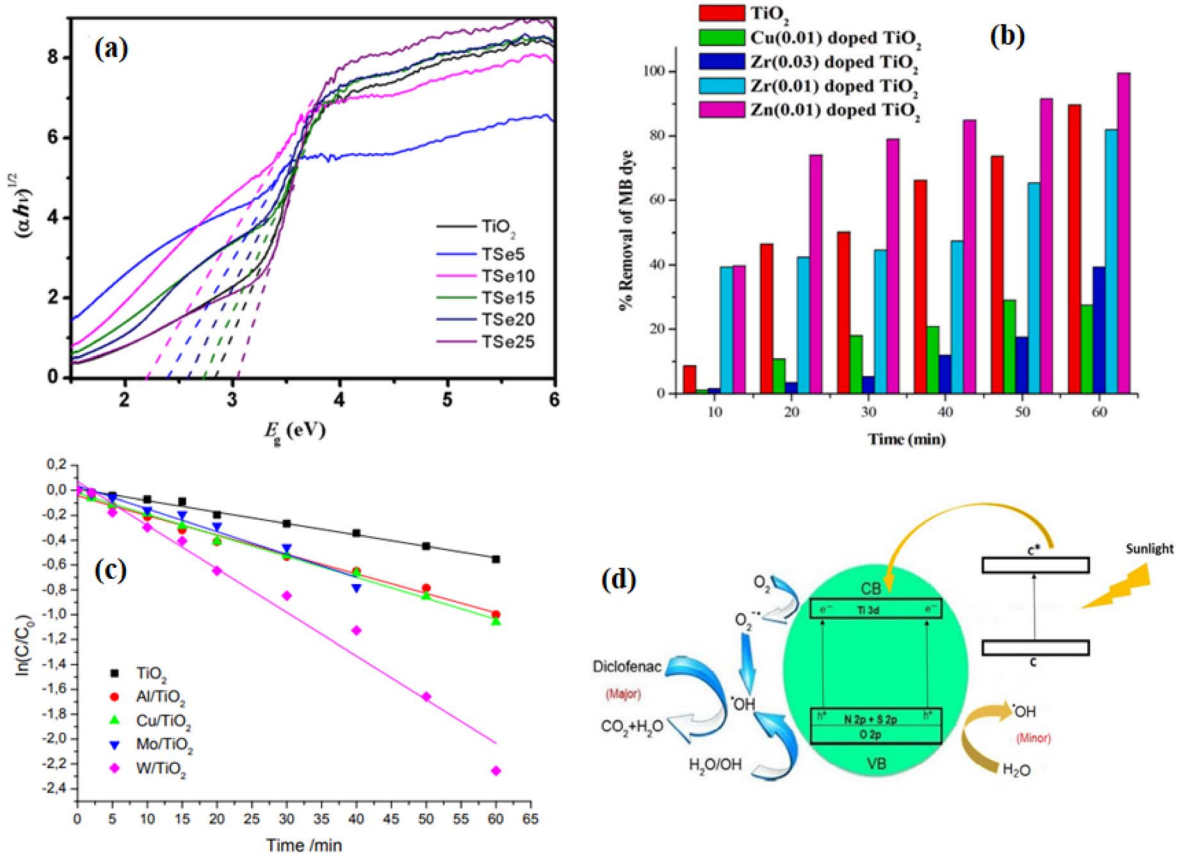

Fig. 6 (a) Optical bandgap of different percentage concentrations of Se-doped TiO_2 photocatalyst;[138] (b) bar diagram of % removal of methylene blue (MB) dye with time under visible light irradiation using pure TiO_2 and Zn, Cu, Zr-doped TiO_2 catalyst;[139] (c) kinetic curves of rhodamine B destruction over the undoped and doped TiO_2 under the visible light irradiation;[140] (d) schematically representation of the improvement in the photoactivity of C–S–N-tridoped TiO_2 photocatalyst.[142]

TiO_2 prepared by chemical reduction, followed by the calcination method for the degradation of rhodamine B, and the deposition of silver nanoparticles significantly inhibited the fast recombination of photogenerated electron–hole pairs.[136] Metal doping is another strategy for reducing charge recombination and enhancing the visible light response of the TiO_2 photocatalyst. Karuppasamy *et al.*[139] synthesized different transition metals (Zn, Zr, Cu)-doped TiO_2 by the sol–gel method and utilized them for the decoloration of methylene blue dye under visible light irradiation. The decoloration efficiency of the prepared materials is presented in Fig. 6b. Among the doped TiO_2, the Zn-doped photocatalyst showed greater photocatalytic activity than pristine TiO_2 or other doped photocatalysts. Thus, the enhanced photocatalytic activity of Zn-doped TiO_2 is attributed to the decrease in the optical bandgap compared to pristine and other dopants. Khlyustova *et al.*[140] synthesized Al, Cu, Mo, and W-doped TiO_2 by the sol–gel method and tested the photocatalytic activity of the doped and pristine TiO_2 using rhodamine B as the pollutant model under the illumination of visible light. As shown in Fig. 6c, the doped photocatalysts have enhanced photocatalytic performance compared to pristine TiO_2. Thus, the doped photocatalysts have a higher kinetic rate constant than pristine TiO_2, which resulted in enhanced photocatalytic performance due to the formation of a new energy level near the conduction band. However, metal doping possesses disadvantages such as photocorrosion and high cost specifically when using noble metals as a dopant. To solve these problems, nonmetal doping such as iodine, sulfur, and nitrogen were used as dopants to enhance the photocatalytic performance of TiO_2. Saroja *et al.*[141] reported the iodine-doped TiO_2 synthesized through the solution combustion method and investigated the effects of iodine dopant concentration on the photocatalytic activity of TiO_2 for the photodegradation of Direct Blue 199. They observed that the visible light response of iodine-doped TiO_2 was enhanced as the dopant concentration increased.

Nonmetal co- and triple-doped TiO_2 for the enhancement of its photocatalytic activity was also reported by different groups. For instance, Ramandi *et al.*[142] reported C–N–S-tri doped TiO_2 anatase phase synthesized b they sonochemical method. They studied the photocatalytic activity of the prepared photocatalysts using diclofenac as a model pollutant under sunlight irradiation. The photocatalytic degradation mechanism of the C–N–S triple-doped TiO_2 is shown in Fig. 6d. Each nonmetal dopant has its own advantages in enhancing the photocatalytic activity of TiO_2 by generating new impurity levels such as N 2p, S 2p, and C 1s. Thus, the doped C acts as a photosensitizer, which injects electrons into the conduction band (CB) under sunlight irradiation, while N and S doping modifies the electronic band structure of TiO_2 by mixing the O 2p of TiO_2 with N 2p and S 2p orbitals, which resulted in the narrowing of the bandgap of TiO_2. According to this report, the electrons in the CB and the trapped electrons trap the adsorbed O_2 molecules to generate the superoxide ($O_2^{\bullet -}$). The main oxidative and reactive species were electrons and $^{\bullet}OH$ radicals, holes were the minor oxidative species, and $O_2^{\bullet -}$ has considerable effects on the degradation of diclofenac. The $^{\bullet}OH$ radicals can be obtained in two ways, as shown in eqn (11)–(13). In eqn (11), molecular O_2 reacts with the electrons (e^-) in the CB and resulted in $O_2^{\bullet -}$. Then, $O_2^{\bullet -}$ reacts with water molecules to produce $^{\bullet}OH$ radical species, as shown in eqn (12). On the other hand, as shown in eqn (13), the h^+ can react with H_2O on the surface of photocatalyst to produce $^{\bullet}OH$ radical species.

$$O_2 + e^- \rightarrow O_2^{\bullet -} \quad (11)$$

$$O_2^{\bullet -} + 2H_2O \rightarrow 2^{\bullet}OH + 2OH^- + O_2 \quad (12)$$

$$h^+ + H_2O + {}^{\bullet}OH \quad (13)$$

The immobilization of TiO_2 on carriers such as activated carbon and metallic oxides is also an effective technique to retard the fast charge recombination and extend the visible light region response of the TiO_2 photocatalyst. Saqib *et al.*[143] reported zeolite-immobilized TiO_2 nanoparticles synthesized using the conventional liquid impregnation method for the efficient degradation of methylene blue dye. The presence of zeolite improves the photocatalytic degradation of methylene blue by four folds compared to pure TiO_2. Coupling TiO_2 with other semiconductors to develop heterojunctions is also another method for enhancing the photocatalytic activity of TiO_2. Coupling TiO_2 with other semiconductors expands the visible light spectrum to the near-infrared response of TiO_2 as well as promotes charge separation.[28] Song *et al.*[144] synthesized a novel TiO_2/Bi_2MoO_6 heterostructures *via* a solvothermal process for the partial oxidation of aromatic alkanes under visible light illumination. They observed that compared to single components TiO_2 and Bi_2MoO_6, the heterostructures TiO_2/Bi_2MoO_6 showed better photocatalytic performance, and the charge separation was also improved.

Heterojunction modes of metal oxide photocatalysts with a similar band structure when coupled enhance the transfers, separation, and stability of photogenerated electrons and holes. For instance, Abdel-Wahab *et al.*[145] reported the coupled heterojunctions TiO_2/Fe_2O_3 with the bandgap of TiO_2 of ~3.2 eV and Fe_2O_3 bandgap of ~2.2 eV. When the TiO_2/Fe_2O_3 heterojunction was irradiated, the electron–hole pairs were generated, as shown in Fig. 7. Thereafter, the photogenerated electrons transfer from the conduction band (CB) of Fe_2O_3 to the conduction band (CB) of TiO_2, with lower potential, whereas the photogenerated holes transfer from the valence band (VB) of TiO_2 to the valence band (VB) of Fe_2O_3 with higher potential. The photogenerated electrons eventually reacted with oxygen molecules to produce $O_2^{\bullet -}$ active species, while the photogenerated holes reacted with water molecules to produce $^{\bullet}OH$ radicals. The prepared TiO_2/Fe_2O_3 heterojunction was applied for the degradation of paracetamol.

Generally, the comparison of pure, doped, noble metals immobilized, composites, and heterojunction of TiO_2-based photocatalysts are summarized in Table 6.

2.4.2 ZnO photocatalyst. Recently, many researchers are highly interested in zinc oxide (ZnO) nanoparticles due to its simple synthesis, low cost, and unique physical and chemical properties, which made it compete with TiO_2 in photocatalytic

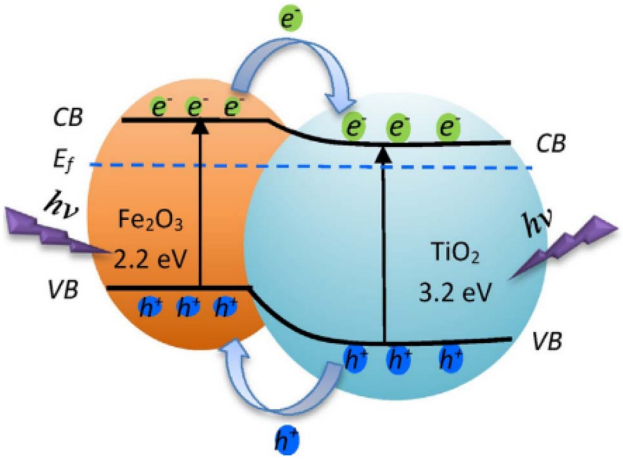

Fig. 7 Schematic diagram of charge transfer in the photoexcited TiO_2/Fe_2O_3 core–shell photocatalysis.[145]

activity degradation of organic pollutants. It has excellent photocatalytic activity under UV irradiation but is less stable compared to TiO_2.[26] ZnO is an n-type semiconductor having a wide bandgap of 3.37 eV.[154] Compared to TiO_2, ZnO responds to broader ranges of the light spectrum including the visible light spectrum.

The photocatalytic activity of ZnO is widely studied and the synthesis method affects the specific surface area of ZnO nanoparticles, which subsequently affects the photocatalytic activity of ZnO nanoparticles. Uribe-Lopez *et al.*[155] reported the effect of the synthesis method on the photocatalytic activity of ZnO nanoparticles synthesized by the precipitation and sol–gel method. They obtained hexagonal rod-like geometries with 50 nm diameters for the ZnO nanoparticle synthesized *via* the sol–gel method and quasi-spherical geometries with 100 nm diameters for ZnO nanoparticles *via* the precipitation method. They estimated the photocatalytic activity of the synthesized ZnO *via* both methods by the degradation of phenol and achieved 100% degradation after 120 min for nanoparticles *via* the precipitation method, whereas they achieved 80% degradation for nanoparticles *via* the sol–gel method after 120 min. Pure ZnO nanoparticles only show the UV light spectrum, which only covers approximately 4% of the solar spectrum; thus, it is important to enhance the visible light response because visible light covers approximately 43% of the solar spectrum, which is much larger than the UV spectrum.[156] In addition to this, because of the wide bandgap of ZnO, the photogenerated

Table 6 Summary of TiO_2-based photocatalysts for the photodegradation of organic pollutants

Catalysts	Synthesis methods	Morphology	Model pollutant	Light	Reaction time	Degradation efficiency	Ref.
TiO_2	*In situ* complexation-hydrolysis	Hierarchical mesoporous nanoshell	Methylene blue	UV	40 min	~100%	146
Fe-doped TiO_2	Sol–gel	Nanoparticles	Arsenic(III)	Visible light	3 h	99%	137
Fe^{3+}-doped TiO_2	Hydrothermal	Nanoparticles	*Para*-nitrophenol	Visible light	5 h	92%	18
Se^{4+}-doped TiO_2	Sol–gel	Nanoparticles	Rhodamine B	Visible light	30 min	91.3%	138
MWCNT/TiO_2	Sol–gel	Nanoparticles	2,4-Dichlorophenol	UV and solar light	120 min	93%	147
MWCNT/TiO_2	Sol–gel	Nanoparticles	2,4-Dichlorophenol	Solar light	120 min	87%	147
Zn-doped TiO_2	Sol–gel	Nanoparticles	Methylene blue	Visible light	60 min	99.64%	139
Mo- and W-doped TiO_2	Sol–gel method	Nanoparticles	Rhodamine B	Visible light	60 min	96%	140
Lu^{3+}-doped TiO_2	Sol–gel	Microparticles	ATP	UV	90 min	—	135
Ce-doped TiO_2	Sol–gel	Nanoparticles	Caffeine	Visible light	120 min	—	12
Iodine-doped TiO_2	Combustion method	Nanoparticles	Direct blue 199	Visible light	—	—	141
C–N–S-tri doped TiO_2	Sonochemical method	Nanoparticles	Diclofenac	Sunlight	180 min	100%	142
Zeolite-immobilized TiO_2	Impregnation	Nanoparticles	Methylene blue	Compact fluorescent light	180 min	94%	143
TiO_2/Bi_2MoO_6	Solvothermal	Nanoparticles	Oxidation of aromatic alkanes	Visible light	—	—	144
TiO_2/ZrO_2	Solvothermal	Nanoparticles	Rhodamine B	Visible light	180 min	99%	148
RGO-TiO_2	Hydrothermal	Nanoparticles	Methyl orange	UV	60 min	100%	149
TiO_2/Fe_2O_3	Ultrasonic-assisted sol–gel	Core–shell nanoparticles	Paracetamol	Mercury lamp	90 min	99%	145
g-C_3N_4/TiO_2	Sol–gel	Nanotubes	Rhodamine B	Visible light	80 min	~97%	150
g-C_3N_4/TiO_2	Template	Nanospheres	Rhodamine B	Visible light	80 min	92%	150
g-C_3N_4/TiO_2	Template	Nanorod	Rhodamine B	Visible light	80 min	94.5%	150
Z-scheme g-C_3N_4/TiO_2	Impregnation/hydrothermal	Nanotubes	Isoniazid	Visible light	4 h	90.8%	151
Ag metal deposited on TiO_2	Chemical reduction	Nanoparticles	Rhodamine B	UV	1 h	—	136
TiO_2/Ag/rGO	Hydrothermal	Nanoparticles	Methylene blue	Visible light	45 min	100%	152
rGO@TiO_2/CN	Hydrothermal	Nanocomposite	Rhodamine B	Solar light	120 min	97%	153

electrons and holes easily recombine, which limits its photocatalytic performance.

To improve the visible light irradiation response and slow down the fast charge recombination of photogenerated electrons–holes pairs of ZnO nanoparticles, different approaches have been developed. Doping with metal ions and metals is a famous approach, in which it reduces the electron–hole recombination and expands the visible light spectrum responses. Ji *et al.*[131] reported the Fe^{3+}- doped, Sn^{4+}-doped, and Fe^{3+} and Sn^{4+}-codoped ZnO nanoparticles prepared by a simple low-temperature solution method and evaluated its photocatalytic activity by the degradation of methylene blue dye. The low to high photocatalytic activity sequence was ZnO, $Fe_{0.01}$ZnO, $Fe_{0.01}Sn_{0.01}$ZnO, and $Sn_{0.05}$ZnO, as presented in Fig. 8a. Pristine ZnO nanoparticles only achieved 45.88% of methylene blue dye degradation, whereas $Sn_{0.05}$ZnO achieved the highest degradation of 99.61% of all the four materials. When Fe^{3+} and Sn^{4+} were incorporated into ZnO, an impurity level near the conduction band was formed, which allows the electrons in the valence band to transition with less energy, as shown in Fig. 8b. Consequently, the concentrations of photogenerated electrons and holes increased and also improved the photocatalytic performance of ZnO nanoparticles. Alam *et al.*[157] synthesized different rare earth metals (La, Nd, Sm, and Dy)-doped ZnO nanoparticles by the sol–gel process and evaluated the photocatalytic degradation of methylene blue and rhodamine B by the improved photocatalyst due to the doped rare earth metals. Qi *et al.*[158] reported transition metal ions (Mn, Fe, Co, Ni, or Cu)-doped ZnO nanoparticles synthesized *via* a solvothermal method. They studied the photodegradation of methylene blue dye under the simulation of visible light. As shown in Fig. 8c and d, the photocatalytic activity of the doped ZnO was increased compared to bare ZnO. Among all the doped photocatalysts, Cu-doped ZnO showed greater photocatalytic activity than bare ZnO and other doped photocatalysts. Thus, the Cu-doped ZnO has the highest rate constant than other photocatalysts, as depicted in Fig. 8d.

Nonmetal-doped ZnO photocatalyst with improved photocatalytic activity under visible light irradiation is also reported. Mirzaeifard *et al.*[159] reported sulfur-doped ZnO synthesized by the hydrothermal method and utilized it for the degradation of rhodamine B under visible light irradiation. They optimized the dosage of the catalyst for the best degradation of rhodamine B, as shown in Fig. 9a. Among those, 0.10 g photocatalyst containing 0.5 wt% of S showed a 100% rate degradation of rhodamine B (5 ppm) at pH = 5 in 90 min.

Immobilizing the ZnO nanoparticles on the polymer supports is another method to improve the photocatalytic

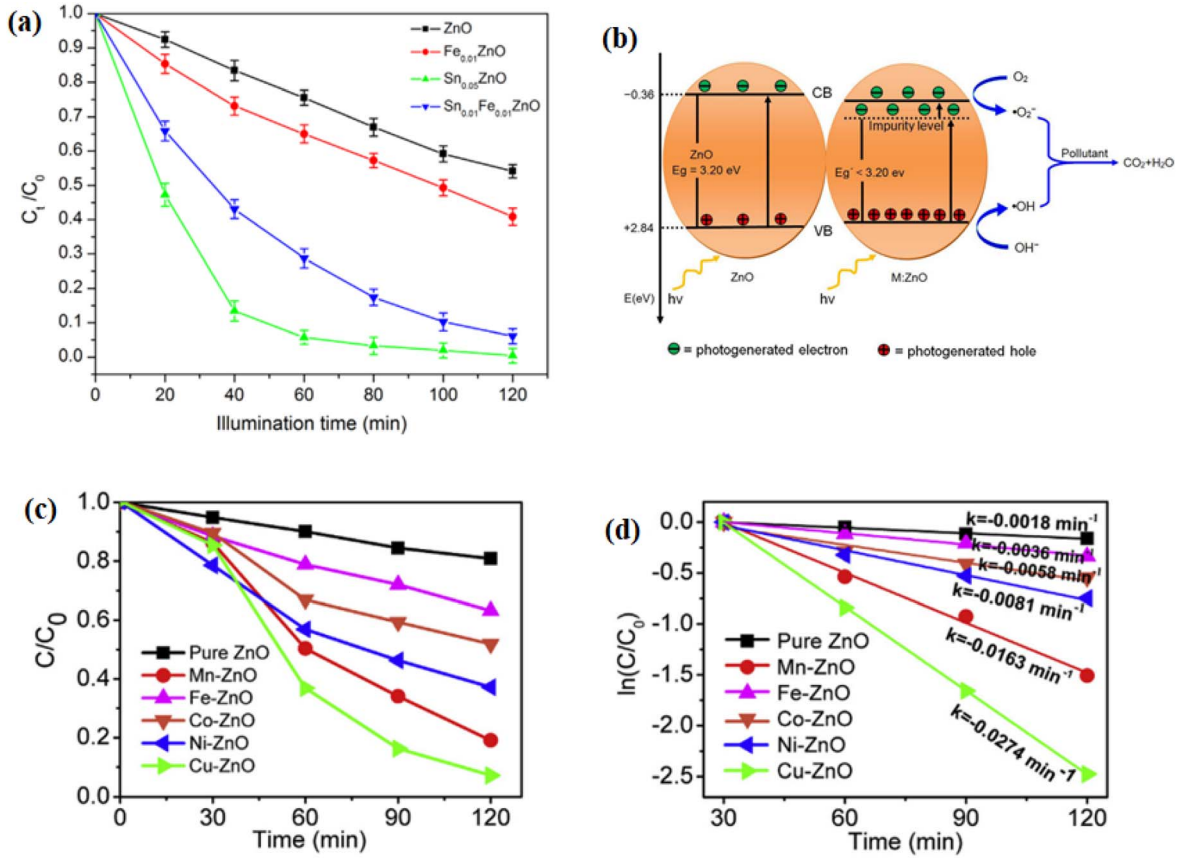

Fig. 8 (a) Photodegradation of methylene blue (MB) dye with different catalysts and (b) photocatalytic schematic diagram of ZnO with the impurity level introduced;[131] (c) photocatalytic activity for the decomposition of MB of the pure ZnO and transition metal-doped ZnO samples under simulated solar light irradiation (photocatalyst dosage, 0.1 g per 200 mL) and $\ln(C/C_0)$ *vs.* time slope for the kinetic rate constant.[158]

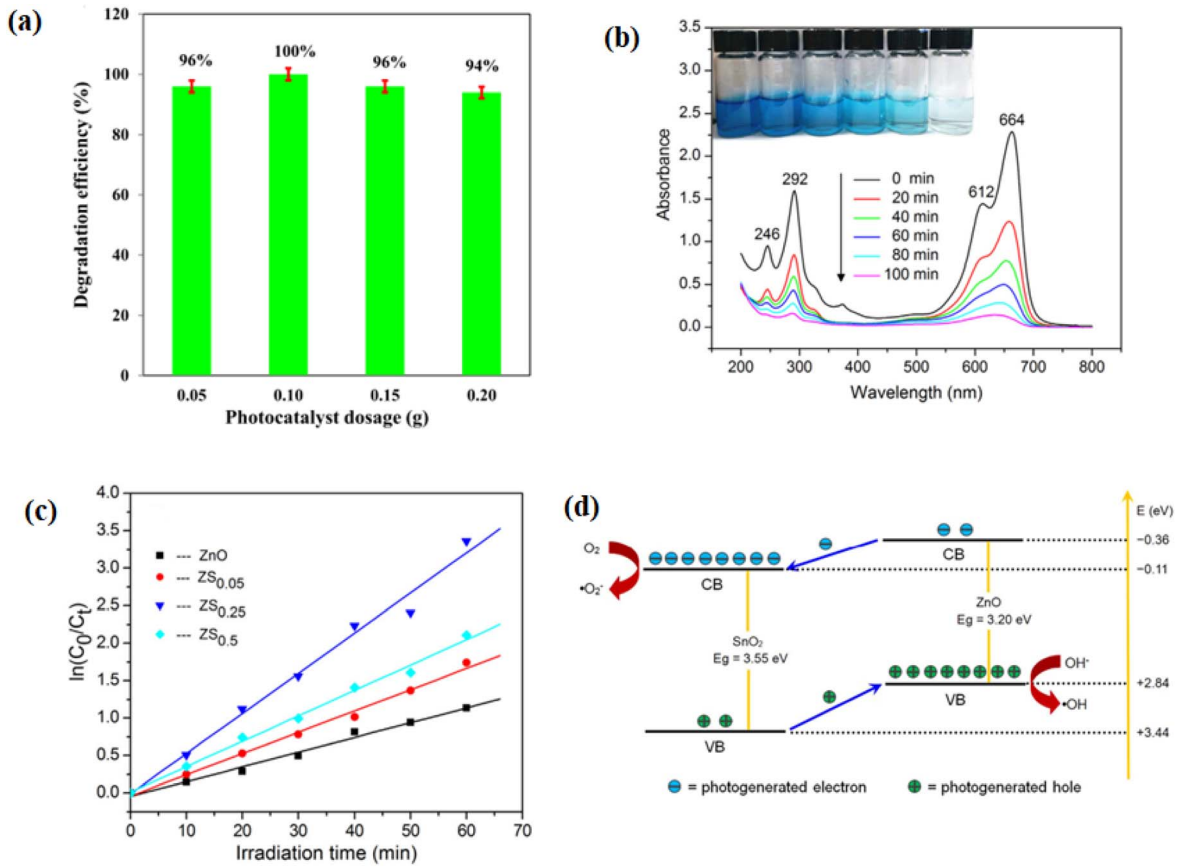

Fig. 9 (a) Degradation efficiency of various dosages of the 0.5 wt% S-doped ZnO photocatalyst;[159] (b) UV-vis spectra of the MB solutions at different irradiation times (the inserted image shows the color change of the MB solution), (c) kinetic linear simulation curves of MB degradation and (d) schematic of the band structure and e^{-}–h^{+} separation in the ZS composite.[162]

activity of ZnO. Mochane *et al.*[160] reviewed the ZnO nanoparticles immobilized in various matrices such as polymers and ceramics. They discriminated that the ZnO nanoparticles were immobilized on the polymer because of high durability, chemical inertness, and low cost. ZnO coupled with other semiconductor metal oxide nanoparticles such as SnO_2, TiO_2, and WO_3 is also another approach to improve the photocatalytic activity of ZnO under the irradiation of visible light. Mugunthan *et al.*[161] reported the visible light irradiation photocatalytic degradation of the pharmaceutical compound diclofenac in wastewater using a ZnO–WO_3 composite semiconductor photocatalyst synthesized through a hydrothermal method. The prepared composite photocatalyst extended the optical response to the visible light spectrum and it showed better stability in retaining the degradation efficiency of 80%. Lin *et al.*[162] also synthesized ZnO–SnO_2 (ZS) nanocomposites with different compositions by a simple coprecipitation method. As shown in Fig. 9b, the aqueous solution of methylene blue dye color becomes colorless with increasing irradiation time. Among the composition of the synthesized nanocomposite, 25% SnO_2 showed the optimum rate constant, as depicted in Fig. 9c. Fig. 9d shows the schematic representation of band structure and electron–hole separation ZnO–SnO_2 composites. As shown in the schematic, the conduction band (CB) potential of ZnO (−0.36 eV) is lower compared to SnO_2 (−0.11 eV) and the valence band (VB) potential of SnO_2 (+3.44 eV) is higher than the VB potential of ZnO. When ZnO–SnO_2 composites were irradiated, the photogenerated electrons flow from low potential to high potential while holes flow in the opposite direction. As a result, the electrons accumulated in the conduction band of SnO_2 and the holes accumulated in the valence band of ZnO. Thus, the sufficiently separated photogenerated electrons and holes provided the enhanced photocatalytic performance of the ZnO–SnO_2 composite. The general summarization of ZnO-based photocatalysts are given in Table 7.

2.4.3 WO_3 photocatalyst. The first experiment on the photocatalysis of tungsten oxide (WO_3) was reported in 1976.[171] Tungsten oxide is an inexpensive metal oxide semiconductor having high and promising photocatalytic performance. It has advantages such as good response to the solar spectrum due to its narrow optical bandgap (2.5–2.8 eV), tunable stoichiometric structure, earth abundance, high oxidizing of holes, and stability.[28] Despite its high photocatalytic performance, the photocatalytic efficiency of WO_3 is limited due to the rapid recombination of photogenerated electrons and holes and less reduction of O_2 molecules because of the relatively low conduction band level that lies above the reduction potential of

Table 7 Summary of ZnO-based photocatalysts for the photodegradation of organic pollutants

Catalysts	Synthesis methods	Morphology	Model pollutant	Light	Reaction time	Degradation after action	Ref.
ZnO	Precipitation	Nanoparticles	Phenol	UV	120 min	100%	155
ZnO	Sol–gel	Nanoparticles	Phenol	UV	120 min	80%	155
$Sn_{0.05}ZnO$	Low-temperature solution	Nanoparticles	Methylene blue	UV	120 min	99.61%	131
Nd-doped ZnO	Sol–gel	Nanoparticles	Methylene blue	UV	25 min	98%	157
Cu-doped ZnO	Solvothermal	Nanoparticles	Methylene blue	Simulated sunlight	2 h	81%	158
Sulfur-doped ZnO	Hydrothermal	Nanoparticle	Rhodamine B	Visible light	90 min	100%	159
ZnO–WO_3	Hydrothermal	Nanoparticle	Diclofenac	Visible light	270 min	80%	161
ZnO–SnO_2	Coprecipitation	Nanocomposites	Biebrich scarlet dye	UV	40 min	97%	163
ZnO–TiO_2	Hydrothermal		Nitrophenol	UV	25 min	95%	164
GO/ZnO	Multistep solution-based	Nanostructure	Methylene blue	Visible light	70 min	100%	165
rGO/ZnO	Hydrothermal	Nanosheets	Methylene blue	Visible light	80 min	100%	166
GO/ZnO	Sol–gel	Nanoparticles	Rhodamine B	Visible light	70 min	99%	
rGO/ZnO	Hydrothermal	Nanoparticles	Methylene blue	Visible light	60 min	100%	167
Ag-doped ZnO/CNTs	Microwave-assisted	Nanoparticle	Reactive black GR	Solar light	30 min	100%	168
Ag-doped ZnO/CNTs	Microwave-assisted	Nanoparticle	Reactive black GR	Visible light	120 min	100%	168
Cu-doped ZnO/g-C_3N_4	One-pot pyrolysis	Nanocomposite	EBT dye	Visible light	90 min	99%	169
ZnO–SnO_2–Sn	—	Nanocomposite	Methylene blue	UV	90 min	95.6%	170

$O_2/O_2^{\bullet-}$. These challenges have inspired researchers to find promising techniques to suppress these challenges by tuning the structure and optical bandgap of WO_3. These techniques include the manipulation of particles morphology, deposition of noble metal on WO_3, doping of elements, carbon-based composite, and forming heterojunctions by coupling with other semiconductors.

Particle morphology control reduces the fast photogenerated electrons and holes recombination, improves charge separation, and enhances the overall photocatalytic activity. Rong and Wang synthesized novel hierarchical hollow nest-like WO_3 micro/nanostructures (HNWMs) by the hydrothermal method without a template and a surfactant.[172] The effects of different parameters such as time of reaction, pH, and annealing conditions have been investigated according to this report. The time-dependent experimental SEM morphology of hierarchical hollow nest-like WO_3 micro/nanostructure is presented in Fig. 10a–i, and the hydrothermal treatment process is shown in Fig. 10j. This morphological structure of WO_3 retained an improved photocatalytic activity toward an aqueous solution of tetracycline (TC) under visible light and possesses good stability and reusability.

Metal doping can narrow the bandgap and retarded the fast charge recombination of the WO_3 photocatalyst. Ramkumar and Rajarajan synthesized nanocrystalline Ni-doped WO_3 thin film deposited by chemical bath deposition method and evaluated its photocatalytic activity by the photodegradation of methyl orange, methylene blue, and phenol.[173] The photocatalytic activity of Ni-doped WO_3 was remarkably improved. Noble-metal deposition and coupling with other semiconductors also enhances the photocatalytic performance of WO_3 under visible light irradiation. Wang *et al.*[174] reported the multiple heterojunctions containing WO_3 nanorods and Pt and TiO_2 nanoparticles for the degradation of gaseous acetaldehyde, rhodamine B dye, and phenol under the illumination of visible light. The multiheterojunction (WO_3–Pt)/TiO_2 photocatalyst's higher performance was attributed to the synergistic effect of efficient electrons and holes transfer at the WO_3/Pt interface and WO_3/TiO_2 interface, respectively.

Graphene, reduced graphene oxide, and other carbon-based composites also enhance the photocatalytic performance of WO_3.[175,176] Jeevitha *et al.*[175] prepared the WO_3-GO nanocomposite *via* the ultrasonic method and investigated the photocatalytic activity, antibacterial, and anticancer of the prepared nanocomposite. The irregular spherical shape and small pores of WO_3 greatly improved the photocatalytic activity. The irregular spherical shape with small pores of WO_3 is shown in Fig. 11a and b. The morphology of graphene oxide (GO) is a sheet, as shown in Fig. 10c and d. The well-distributed nanosphere WO_3 on the graphene sheet is shown in Fig. 11e and f. This report compared the obtained photocatalytic degradation of methylene blue dye under the illumination of visible light, as shown in Fig. 11g and h. Fig. 11g shows the photocatalytic activity of pure WO_3 and in 270 min, it could not completely degrade the methylene blue dye. However, the WO_3-GO nanocomposite achieved a 97.03% rate of degradation of methylene blue dye in 180 min, as presented in Fig. 11h. The summary of WO_3-based photocatalysts is given in Table 8.

2.4.4 Cu_2O photocatalyst. Copper oxide nanoparticle is the most probable candidate of promising photocatalytic materials for the degradation of organic pollutants. It possesses high optical absorption properties and optimal optical bandgap. Copper oxide nanoparticles can be produced at a low cost due to its precursor materials being highly abundant in the earth's crust.[16] It has two semiconducting phases, namely, cupric oxide (CuO) and cuprous oxide (Cu_2O), which possesses approximately 1.6 eV and 2.4 eV optical bandgap, respectively. Cu_2O is a p-type metal oxide semiconductor with a 2.4 eV bandgap.[188] Since its bandgap is optimal for the application of photocatalysis under visible light illumination, it is the preferable candidate for photocatalytic activity.

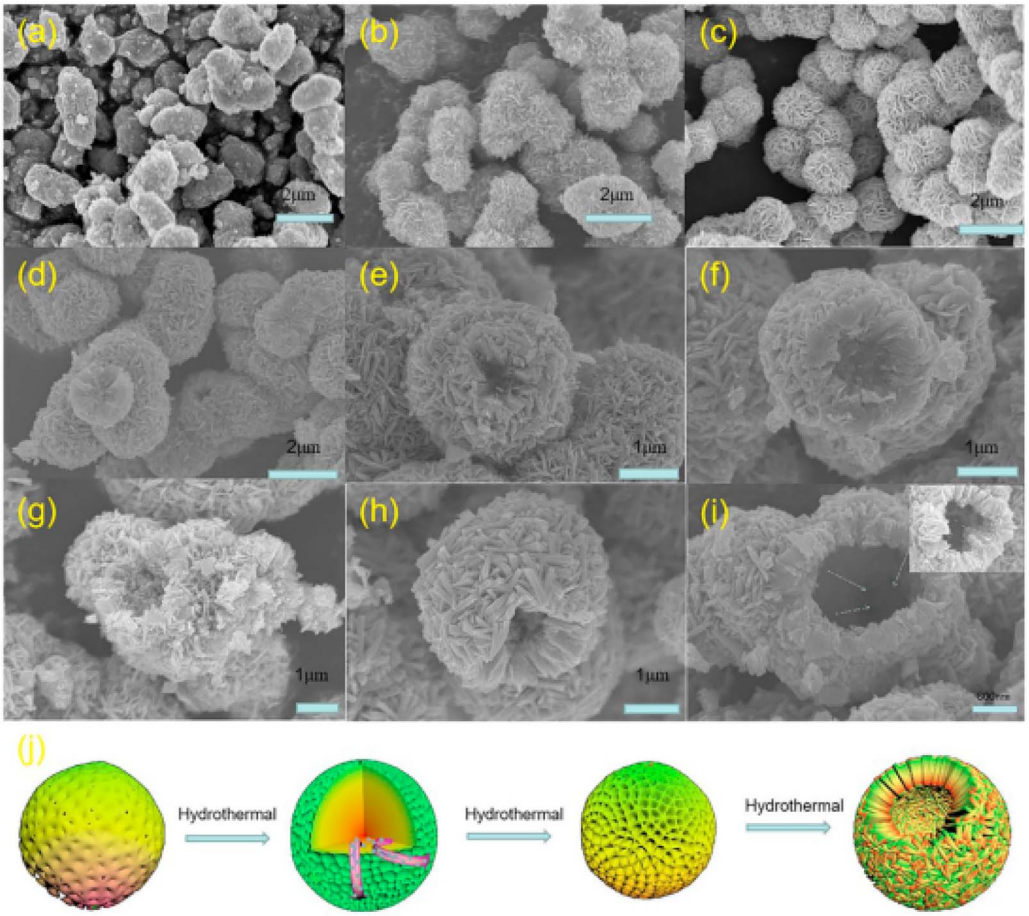

Fig. 10 SEM images of the hollow nest-like WO_3 micro/nanostructures obtained after hydrothermal treatment at different times: (a) 3 min; (b) 9 min; (c) 15 min; (d) 2 h; (e) 4 h; (f) 6 h; (g) 8 h; (h) 10 h; and (i) 16 h; (j) schematic diagram of the hollow nest-like WO_3 micro/nanostructures formation process.[172]

Muthukumaran *et al.*[16] synthesized cuprous oxide (Cu_2O) nanoparticles photocatalyst *via* the sonochemical method for the degradation of Malachite green under the illumination of visible light. The prepared nanoparticle achieved 91.89% degradation efficiency after 45 min visible light illumination. There are various green syntheses reported on the cuprous oxide (Cu_2O) nanoparticles for the photocatalytic degradation of organic pollutants. Kerour *et al.*[182] synthesized Cu_2O nanoparticles by a green method using aloe vera leaves plants extracted for the degradation of methylene blue dye and were able to completely degrade methylene blue after 10 min of visible light illumination. Yadav *et al.*[183] used sugarcane bagasse to synthesize ecofriendly Cu_2O nanoparticles for the degradation of methyl red, Congo red, methylene blue, and methyl orange organic dyes.

Despite the achievement and simple green synthesized Cu_2O nanoparticles, the rate of recombination of photogenerated electrons and holes, stability, and photocorrosion are challenging for photocatalytic applications.[127] For instance, during the photocatalytic process, when Cu_2O is irradiated, it can be converted into CuO through photooxidation, which shows the deactivation of the photocatalytic process.[189] To suppress these challenges and improve the photocatalytic activity of Cu_2O, different ideas have been generated by researchers. The preparation of Cu_2O nanoparticles with good control on the morphology significantly influences its chemical and physical properties in using them as photocatalyst materials.[190] Prado-Chay *et al.*[184] synthesized hierarchical Cu_2O microspheres by a simple chemical method at room temperature with enhanced photocatalytic activity for the degradation of methyl orange under visible light irradiation.

Coupling with other metal oxides to create heterojunctions is another method to enhance the photocatalytic performance of Cu_2O. Wang *et al.*[185] reported ZnO/Cu_2O heterojunctions designed by the self-templating method for the degradation of rhodamine B and achieved 96% within 40 min under visible light irradiation. Making composite with carbon-based materials is also another strategy to boost the photocatalytic activity of Cu_2O. K. Polat produced a 2D thin film catalyst Cu_2O/2D graphene on copper foil having photocatalytic activity under the visible light spectrum.[186] Karthikeyan *et al.*[187] reported hierarchical Cu_2O nanospheres and Cu_2O/rGO nanocomposites for the degradation of 4-chlorophenol and production of H_2 under the illumination of visible light, which is attributable to enhanced visible absorption. Z-scheme modification is also the

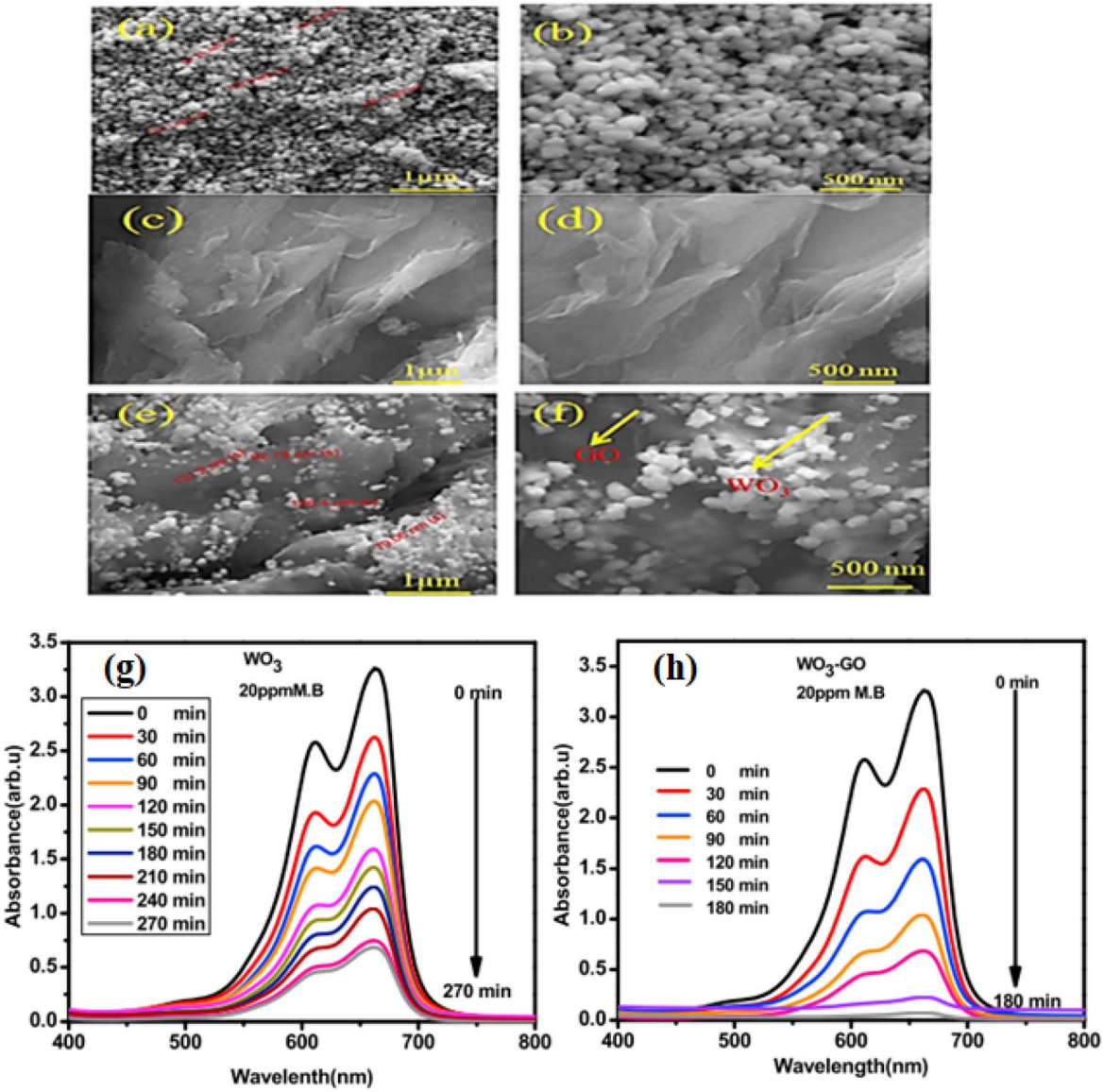

Fig. 11 FE-SEM image of (a and b) WO_3, (c and d) GO, and (e and f) WO_3-GO nanocomposite; (g) absorbance spectra of MB by pure WO_3 and (h) absorbance spectra of methylene blue dye by the WO_3-GO nanocomposite.[175]

Table 8 Summary of WO_3-based photocatalysts for the photodegradation of organic pollutants

Catalysts	Synthesis methods	Morphology	Model pollutant	Light	Reaction time	Degradation after action	Ref.
WO_3	Hydrothermal	Hierarchical hollow nest-like	Tetracycline	Visible light	60 min	94.3%	172
Ni-doped WO_3	Chemical bath deposition	Thin film	Methyl orange	Visible light	150 min	88%	173
(WO_3–Pt)/TiO_2	Hydrothermal	Nanoparticles	Rhodamine B	Visible light	90 min	98.8%	174
WO_3-GO	Ultrasonic method	Nanocomposite	Methylene blue	Visible light	180 min	97.03%	175
rGO/WO_3 nanoplate	One-step hydrothermal	Nanohybrids	Methylene blue	Sunlight irradiation	90 min	82.2%	177
rGO/WO_3	Hydrothermal	Nanorod	Rhodamine B	Visible light	120 min	94%	178
Ag@WO_3@rG	Hydrothermal	Nanocomposites	Rhodamine B	Solar simulation	70 min	99.5%	179
WO_3/g-C_3N_4/h-BN	Thermal treatment	Lamellar structure	Tetracycline	Visible light	60 min	81.4%	180
Indigo-RGO/WO_3	Hydrothermal	Nanosheets	Methylene blue	Sunlight	120 min	~80	181

most effective technique to improve the photocatalytic activity of Cu_2O. Chen *et al.*[191] synthesized a Z-scheme Cu_2O-(rGO-TiO_2) photocatalyst for the degradation of 2,2′,4,4′-tretrabromodiphenyl ether. The reported Z-scheme photocatalytic performance by this group was greater than either single or composite of Cu_2O and TiO_2 under the same reaction

Table 9 Summary of Cu_2O-based photocatalysts for the photodegradation of organic pollutants

Catalysts	Synthesis methods	Morphology	Model pollutant	Light	Reaction time	Degradation after action	Ref.
Cu_2O	Sonochemical	Nanoparticles	Malachite green	Visible light	45 min	91.89%	16
Cu_2O	Green synthesis	Nanoparticles	Methylene blue	Solar simulator	10 min	100%	182
Cu_2O	Biogenically synthesized	Nanoparticles	Methyl orange	Visible light	80 min	77.39%	183
Cu_2O	Chemical solution	Hierarchical nanoparticles	Methyl orange	Visible light	120 min	76%	184
ZnO/Cu_2O	Self-templating		Rhodamine B	Visible light	40 min	96%	185
Cu_2O/graphene/Cu	Magnetron sputtering	Thin film	Hydrogen peroxide	Visible light	—	—	186
Cu_2O/rGO	Self-assembly	Pompon Dahlia-like	4-Chlorophenol	Visible light	1 h	95%	187

condition. Different Cu_2O-based photocatalysts are summarized in Table 9.

2.4.5 CuO photocatalyst. Because of its desirable properties, such as easy preparation low cost, and nontoxicity, CuO nanoparticles acquired great interest in the research field such as photocatalysis, solar cells, supercapacitors, biodiesel, water pollutant removal, and electrocatalysis.[27] CuO nanoparticles are an outstanding and efficient photocatalytic material for the degradation of organic pollutants. However, similar to Cu_2O, CuO also has the limitation that comes from rapid photogenerated recombination and photocorrosion. Hence, researchers have employed various techniques to address these concerns. Among these, the CuO composite with carbon-based materials has attracted great attention. Banu *et al.*[192] synthesized GO/CuO nanocomposite by the hydrothermal method for the photocatalytic degradation of azure-B dye with an efficiency of 95%. The enhanced photocatalytic activity of the prepared nanocomposite was attributed to the small size and high surface area of GO/CuO. Coupling it with Cu_2O and graphene oxide also enhances its photocatalytic performance. Zhang *et al.*[193] reported CuO–Cu_2O/GO nanocomposite for the degradation of tetracycline and methyl orange and achieved 90% and 95% degradation efficiency after 120 min under visible light irradiation.

Coupling with other metal oxide semiconductors also enhances the photocatalytic performance of CuO nanoparticles. Sakib *et al.*[194] synthesized CuO/ZnO nanocomposite through the mechanochemical combustion method for the degradation of methylene blue under visible light irradiation. They achieved methylene blue degradation of 81% and 98% using ZnO and CuO/ZnO, respectively. Forming a p–n junction heterostructure has the advantages of widening the light harvesting and retarding the fast recombination of the photogenerated electrons and holes. Malwal and Gopinath synthesized the 3D hierarchical nanostructured n-type ZnO and Fe_3O_4 deposited on p-type CuO *via* thermal oxidation, followed by microwave-assisted deposition for the formation of p–n heterojunctions.[195] The prepared p–n heterojunctions enhanced the photocatalytic activity for the degradation of Congo red dye under solar light irradiation. The enhanced photocatalytic performance was attributed to the effective and sufficient charge separation formation of the p–n junction heterostructures at the interface of p-type (CuO) and n-type (ZnO/Fe_3O_4) semiconductors, as depicted in Fig. 12. The charge

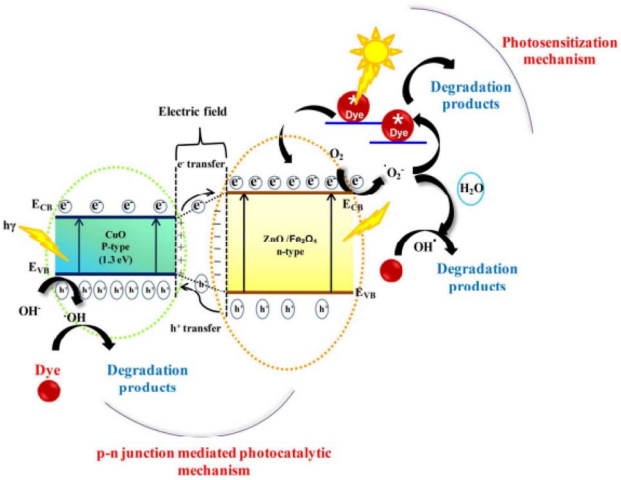

Fig. 12 Proposed mechanisms for the photodegradation of Congo red dye under solar light irradiation using p–n heterojunctions (p-type CuO and n-type ZnO/Fe_3O_4) semiconductor.[195]

separation creates an electric field at the interfaces. For dye degradation, the photosensitization and p–n junction-mediated photocatalytic mechanisms are involved, as shown in Fig. 12.

Metal doping is another effective strategy to improve the photocatalytic performance of CuO. George *et al.*[196] synthesized nanoflower-like 3D transition metal-doped CuO nanostructure by the sonication method for the degradation of methylene blue dye under visible light illumination. The 3D transition metal incorporated into CuO played a great role in tuning the structure, morphology, and optical properties. Maraj *et al.*[197] reported Mo-doped CuO nanoparticles synthesized by the sol–gel process and utilized it for the degradation of methylene blue under visible light irradiation. Islam *et al.*[198] synthesized Ce-doped CuO nanoparticles through the sol–gel autocombustion method and utilized it for the degradation of methylene blue under the illumination of visible light. Ce-doped CuO nanoparticles exhibited better photocatalytic activity than undoped CuO nanoparticles. The general summary of different CuO nanoparticles and CuO-based photocatalysts are summarized in Table 10.

2.4.6 SnO_2 photocatalyst. Tin dioxide (SnO_2) is an n-type semiconductor and has a wide range of applications in areas such as catalysts, gas sensors, transistors, batteries, and

Table 10 Summary of CuO-based photocatalysts for the photodegradation of organic pollutants

Catalysts	Synthesis methods	Morphology	Model pollutant	Light	Reaction time	Degradation efficiency	Ref.
CuO	Mechanochemical	Nanoparticles	Methyl green	Sunlight	60 min	65%	199
CuO	Green synthesis	Nanoparticles	Rhodamine B	UV	90 min	98%	200
CuO	Microwave-assisted	Nanoparticles	Methylene blue	Sunlight	90 min	99%	201
GO/CuO	Hydrothermal	Lamellar sheets	Azure-B dye	Tungsten lamp	120 min	95%	192
CuO-Cu_2O/GO	Hydrothermal	—	Tetracycline	Visible	120 min	90%	193
CuO-Cu_2O/GO	Hydrothermal	—	Methyl orange	Visible light	120 min	95%	193
CuO/ZnO	Mechanochemical combustion	Nanoparticles	Methylene blue	Solar irradiation	2 h	98%	194
ZnO	Mechanochemical combustion	Nanoparticles	Methylene blue	Solar irradiation	2 h	81%	194
ZnO@CuO	Microwave-assisted	Hierarchical nanostructures	Congo red dye	Visible light	300 min	90%	195
Mo-doped CuO	Sol–gel	Nanoparticles	Methylene blue	Visible light	120 min	90%	197
Ce-doped CuO	Sol–gel	Nanoparticles	Methylene blue	Visible light	3 h	99%	198
CuO/g-C_3N_4	Pyrolysis	Nanosheets	Salicylic acid	Visible light	80 min	100%	202
ZnO/CuO/g-C_3N_4	Cocrystallization	Sheet-like	Methylene blue	Visible light	50 min	97.46%	203
ZnO/CuO/g-C_3N_4	Cocrystallization	Sheet-like	Congo red	Visible light	50 min	91.73%	203

transparent electrodes.[204] SnO_2 in its nanoparticles has a high surface-to-volume ratio that enhances the active sites and is expected to exhibit good photocatalytic activity. Pure SnO_2 is rarely studied because of the simultaneous formations of Sn^{2+} and Sn^0 during the photocatalysis process. Thus, it can be presented as SnO_2, SnO, or Sn in the catalyst. Moreover, in photocatalytic applications, it is found as a composite form with other semiconductors to suppress instability, and the composite of SnO_2 with other semiconductors has been widely reported. SnO_2 is also an ultraviolet-active metal oxide semiconductor due to its wide bandgap of 3.6 eV similar to TiO_2.[205] To date, numerous efforts such as building heterojunctions, morphology control, metal or nonmetal doping, and carbon-based materials composite have been developed to suppress these challenges. G. Devi and R. Shyamala synthesized SnO_2 and α-Fe_2O_3 by the sol–gel method and combined them by mixing and grinding to form a SnO_2–α-Fe_2O_3 composite.[206] They studied the photocatalytic activity of the prepared composite using phenol as a pollutant model. Due to the redshifts in the bandgap, the prepared composite showed higher extent absorption in the visible light region.

Combining SnO_2 with other metal oxide and carbon-based materials also enhances its visible light activity. Yao *et al.*[207] reported SnO_2/TiO_2/RGO nanocomposite synthesized by the hydrothermal method with enhanced photocatalytic activity under visible light illumination for the degradation of rhodamine B. The superior photocatalytic activity of the synthesized nanocomposite is attributed to the great efficiency of light absorption and outstanding charge separation and transfers. Wang *et al.*[208] synthesized micron-sized spherical SnO_2 (Fig. 13a) and flower In_2O_3 (Fig. 13c) by the hydrothermal method and prepared the In_2O_3/SnO_2 composite by the two-step method. Fig. 13e shows the morphology of In_2O_3/SnO_2, and Fig. 13b, d, and f show the magnified morphology of the SnO_2, In_2O_3, and In_2O_3/SnO_2 composite, respectively. According to this report, the bandgap of the prepared materials in decreasing order is SnO_2, In_2O_3, and In_2O_3/SnO_2, respectively, as presented in Fig. 13g. For the photocatalytic degradation study of the prepared photocatalyst, they used rhodamine B as a model organic pollutant, and the In_2O_3/SnO_2 composite showed the highest degradation rate of 97% after 240 min irradiation (Fig. 13h), which was twice that of pure SnO_2 or In_2O_3. The photocatalytic mechanism of the prepared composite is shown in Fig. 13i. In this report, the superoxide ($O_2^{\bullet -}$) and holes play a great role in the degradation of rhodamine B, while $^{\bullet}OH$ played an auxiliary role. The energy band positions of the two compounds matched well, as shown in Fig. 13i, in which the photogenerated electrons and holes separated effectively. An electron (e^-) was generated in the conduction band and a hole (h^+) was generated in the valence band.

When the two compounds were irradiated, electrons and holes were generated, as shown in eqn (14) and (15). The photogenerated holes of SnO_2 transferred to the valence band of In_2O_3 (eqn (16)) and the photogenerated electrons of In_2O_3 transferred to the conduction band of SnO_2 (eqn (17)). Thereafter, e^- reacts with O_2 to form superoxide ($O_2^{\bullet -}$) (eqn (18)), and the photodegradation process of rhodamine B is shown in eqn (19)–(21).[208]

$$SnO_2 + h\nu \rightarrow SnO_2(h^+)_{VB} + SnO_2(e^-)_{CB} \quad (14)$$

$$In_2O_3 + h\nu \rightarrow In_2O_3(h^+)_{VB} + In_2O_3(e^-)_{CB} \quad (15)$$

$$SnO_2(h^+)_{VB} \rightarrow In_2O_3(h^+)_{VB} \quad (16)$$

$$In_2O_3(e^-)_{CB} \rightarrow SnO_2(e^-)_{CB} \quad (17)$$

$$SnO_2(e^-)_{CB} + O_2 \rightarrow O_2^{\bullet -} \quad (18)$$

$$\text{Rhodamine B} + O_2^{\bullet -} \rightarrow H_2O + CO_2 \quad (19)$$

$$\text{Rhodamine B} + h^+ \rightarrow H_2O + CO_2 \quad (20)$$

$$\text{Rhodamine B} + {}^{\bullet}OH \rightarrow H_2O + CO_2 \quad (21)$$

Combining SnO_2 with noble metals also enhances its photocatalytic activity and its visible light response. Ansari *et al.*[209] synthesized Ag–SnO_2 nanocomposites in water at room temperature using electrochemically-active biofilm and utilized

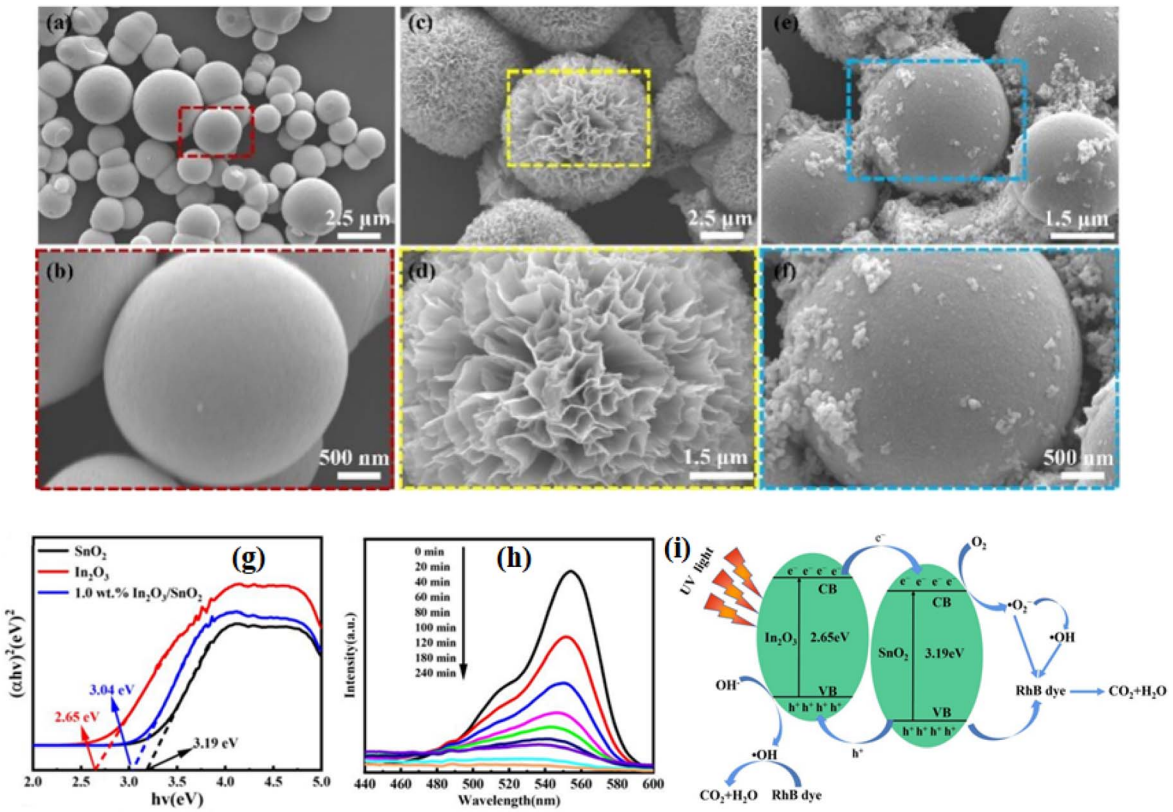

Fig. 13 SEM images: (a and b) of the pure SnO_2; (c and d) of the prepared In_2O_3; (e and f) of the prepared 1.0 wt% In_2O_3/SnO_2 composite photocatalysts; (g) the bandgap; (h) degradation kinetics of rhodamine B. (i) Schematic illustration of the separation and migration mechanism of photogenerated electron–hole pairs of the In_2O_3/SnO_2 composite.[208]

it for the degradation of methylene blue, methyl orange, 2-chlorophenol, and 4-nitrophenol under visible light irradiation. The prepared nanocomposite showed enhanced photocatalytic activity compared to pure SnO_2. Doping with metals is also an effective method to slow down the photogenerated electron–holes recombination and expand the visible light activity of SnO_2. Ran *et al.*[210] reported hollow-structured Ti-doped SnO_2 prepared using silica microspheres as templates for the decomposition of methylene blue under UV and visible-light irradiation. Compared with pristine SnO_2 hollow spherical, Ti-doped SnO_2 showed enhanced photocatalytic activity with 92% rate of degradation under UV light irradiation and 54% under visible light irradiation decomposition of methylene blue within 135 min of degradation time. Ali Baig *et al.*[211] synthesized a Zn-doped SnO_2 photocatalyst by the hydrothermal method for the degradation of methylene blue under visible light illumination. The effects of Zn-doping are clearly understood to prolong the photoabsorption to the visible region and decreasing electron–hole recombination. The summary of SnO_2-based photocatalysts for the photodegradation are given in Table 11.

2.4.7 Fe_2O_3 photocatalyst. Iron oxide can be present in different phases such as maghemite (ν-Fe_2O_3), magnetite (Fe_3O_4), hematite (α-Fe_2O_3), and wustite (FeO). Among these phases, Fe_2O_3 and Fe_3O_4 are the most common phases of iron oxide in nature. Because of the easy manipulation of morphology, structures, and dimension orientation to provide stability, Fe_2O_3 is applied in various industrial applications.[118] Fe_2O_3 has four polymorphic phases, namely, ε-Fe_2O_3, γ-Fe_2O_3, β-Fe_2O_3, and α-Fe_2O_3 (hematite).[102] Among these crystallographic phases, α-Fe_2O_3 (hematite) is the most stable and widely used in different applications such as sorbents, catalysts, biomedical devices, and solar cells.[216] Nanosized α-Fe_2O_3 has better magnetic behavior (ferromagnetic) than ferum (Fe).[217,218] This magnetic behavior helps to separate the photocatalyst materials from the solution after the photocatalytic treatment.

Moreover, α-Fe_2O_3 has been used as a photocatalyst material due to its energy bandgap being appropriate for the photocatalysis process. However, pure Fe_2O_3 is limited in its application in photocatalysis because of disadvantages such as lower minority charge carriers mobility, sluggish surface kinetics, the short diffusion length of photogenerated carriers, and high recombination rate of photogenerated electron–holes pairs.[219] Different strategies have been developed to address these problems. The suitably positioned bandgap of α-Fe_2O_3 allows it to form a composite with other metal oxides to reduce the recombination of photogenerated electron–hole pairs. Senthil *et al.*[220] reported α-Fe_2O_3/WO_3 composite photocatalyst designed by a simple physical mixing process and utilized it for the photodegradation of methylene blue under visible light irradiation. The prepared composite exhibited excellent photocatalytic activity, which was attributed to the strong absorption of α-Fe_2O_3/WO_3

Table 11 Summary of SnO_2-based photocatalysts for the photodegradation of organic pollutants

Catalysts	Synthesis methods	Morphology	Model pollutant	Light	Reaction time	Degradation efficiency	Ref.
SnO_2	Precipitation	Nanoparticles	Methylene blue	UV	180 min	79%	204
SnO_2/TiO_2/RGO	Hydrothermal	Nanoparticle	Rhodamine B	Visible light	120 min	83.84%	207
In_2O_3/SnO_2	Hydrothermal	Nanoparticle	Rhodamine B	Visible light	240 min	97%	208
Ag–SnO_2 nanocomposites	Electrochemically active biofilm	Nanoparticle	Methylene blue, methyl orange	Visible light	6 h for MO and 5 h for MB	100%	209
Ti-doped SnO_2	Templates	Nanoparticle	Methylene blue	UV	135 min	92%	210
Ti-doped SnO_2	Templates	Nanoparticle	Methylene blue	Visible light	135 min	54%	210
Zn-doped SnO_2	Precipitation	Nanoparticle	Methylene blue	Visible light	120 min	93.03%	211
SnO_2/g-C_3N_4	Solution ball milling-baking	Layer structure	Trichlorophenol	Visible light	5 h	85%	212
SnO_2/GL-C_3N_4	Hydrothermal	Layer structure	Rhodamine B	Visible light	3 h	92%	213
SnO_2/TiO_2	Hydrothermal	Nanoparticle	methylene blue dye	Solar light	50 min	~90%	214
La_2O_3/SnO_2	Coprecipitation	Nanoparticles	Methylene blue	UV	70 min	92%	215

composite and slow down recombination of electron–hole pairs. The polymer coating is also another method to enhance the photocatalytic activity of α-Fe_2O_3. Zhang *et al.*[221] synthesized nitrogen-rich crosslinked copolymer, poly(1,4,8,11-cyclotetradecane [2,2-bipyridine]-5,5-dicarboxamine) (PNH). This polymer covered Fe_2O_3 by moderate hydrothermal treatment to form Fe_2O_3@PNH, which showed excellent photocatalytic activity for the degradation of tetracycline with catalytic performance of ~90% under visible light illumination, which was three times greater than that of Fe_2O_3.

Doping is another effective strategy to address the aforementioned problems that generate electron trap centers. Li *et al.*[219] synthesized different metal-doped Fe_2O_3 nanoparticles using fabric filter dust as starting materials for the degradation of methyl orange. The different metal-doped materials showed a 82.99% degradation rate under the illumination of visible light, whereas the undoped Fe_2O_3 achieved only 38.94%. Nonmetal doping can also improve the photocatalytic activity of Fe_2O_3 nanoparticles. Mendiola-Alvarez *et al.*[222] synthesized phosphorus-doped Fe_2O_3–TiO_2 by the sol–gel method and utilized it for the degradation of sulfamethazine under visible light irradiation. The doped composite has shown improved photocatalytic performance compared to either the Fe_2O_3–TiO_2 composite or TiO_2, which was attributed to the reduced bandgap, small crystallite size, increased existence of hydroxyl on the catalyst surface, and high surface area. Graphene is a type of carbonaceous material having excellent transparency, lightweight, high electrical conductivity, unique structure, high adsorption capacity, and high specific surface area properties, which enhances the photocatalytic performance of α-Fe_2O_3 when it made the hybrid. S. Frindy and M. Sillanpää synthesized α-Fe_2O_3 hybridized with graphene by the hydrothermal method for the degradation of rhodamine B under visible light irradiation and it showed high catalyst activity of ~98%.[223] They demonstrated that the incorporation of graphene into α-Fe_2O_3 nanoparticles resulted in high photocatalytic activity compared to pure α-Fe_2O_3 or α-Fe_2O_3 loaded on other carbonaceous materials. The summary of Fe_2O_3-based photocatalysts for photocatalytic degradation is given in Table 12.

2.4.8 Bi_2O_3 photocatalyst. Bismuth oxide (Bi_2O_3) is found in various crystals forms such as triclinic (ω), orthorhombic (ε), face-centered cubic (δ), body-centered cubic (γ), monoclinic (α), tetragonal (β), and hexagonal assembly.[21] Bi_2O_3 has an excellent photocatalytic activity for wastewater treatment, CO_2 reduction, nitrogen fixation, and water splitting under the irradiation of visible light solar spectrum. However, Bi_2O_3 is now confronted with a larger recombination rate of the electron–hole pairs, which significantly reduces its photocatalytic activity for the degradation of organic pollutants.[232] To boost the overall photocatalytic efficiency of Bi_2O_3, many strategies including composition with other materials, morphology, shape, microstructure, surface structure, interface-engineering, oxygen vacancy, and doping with metal and nonmetal have been developed. For instance, when it is coupled with other semiconductors, its photocatalytic activity becomes more favored. Hsieh *et al.*[237] synthesized the Bi_2O_3/CeO_2 composite *via* the hydrothermal method and compared the photocatalytic performance of pristine Bi_2O_3, CeO_2, and Bi_2O_3/CeO_2 composite, in which the composite showed excellent catalytic performance under visible light illumination for the degradation of Orange II dye. The $CuCo_2S_4/Bi_2WO_6$ heterojunction used for the degradation of tetracycline hydrochloride has also reported by Wang *et al.*[245]

Doping is also an effective and efficient strategy to reduce the large recombination rate of electron–hole pairs. Li *et al.*[232] reported the La-doped Bi_2O_3 prepared *via* the sol–gel method in which La^{3+} doping creates oxygen vacancies on the surface of Bi_2O_3 and also as an efficient scavenger to capture the photoinduced electrons. The prepared material was used for the degradation of methyl orange (MO) and phenol and showed an enhanced photocatalytic activity, which was attributed to the strong synergistic effects of La^{3+} doping and oxygen vacancies

Table 12 Summary of Fe_2O_3-based photocatalysts for photocatalytic degradation

Catalysts	Synthesis methods	Morphology	Model pollutant	Light	Reaction time	Degradation efficiency	Ref.
Fe_2O_3	Chemical solution	Porous nanorods	Rhodamine B	Simulated solar light	270 min	86.4%	224
α-Fe_2O_3/WO_3	Hydrothermal	Nanoparticles	Methylene blue	Visible light	60 min	100%	220
Fe_2O_3@PNH	Condensed polymerization	—	Tetracycline	Visible light	120 min	90%	221
Al and Ti doped Fe_2O_3	From fabric filter dust	Nanoparticles	Methyl orange	Visible light	180 min	82.99%	219
P-doped Fe_2O_3–TiO_2	Microwave-assisted sol–gel	Nanoparticles	Sulfamethazine	Visible light	300 min	100%	222
α-Fe_2O_3-Gr	Hydrothermal	Nanoparticle	Rhodamine B	Visible light	75 min	98%	223
α-Fe_2O_3@TiO_2	Coprecipitation	Nanocomposites	Methylene blue	Visible light	120 min	92%	225
TiO_2/Fe_2O_3	Hydrothermal	Nanocomposites	Cr(VI)	Visible light	160 min	100%	226
α-Fe_2O_3/g-C_3N_4	Heat treatment	Nanocomposites	Diazinon	UV	50 min	100%	227
GO/α-Fe_2O_3	Coprecipitation	Nanoparticles	Methylene blue	Visible light	90 min	90%	228
Fe_2O_3/TiO_2	Atomic layer deposition	Nanoparticles	Methyl orange	Visible light	90 min	97.4%	229
Fe_3O_4@Bi_2O_3-RGO	Self-assembly	Core–shell	Ciprofloxacin	Visible light	240 min	98.3%	230

(OVs), as shown in Fig. 14. According to this report, the photocatalytic mechanism for the degradation of methyl orange and phenol are as follows.

$$\text{La-}Bi_2O_3 + h\nu \rightarrow h^+ + (e^-)_{CB} \quad (22)$$

$$\text{La-}Bi_2O_3 + h\nu \rightarrow h^+ + (e^-)_{OVs} \quad (23)$$

$$La^{3+}(5d^06s^0) + (e^-)_{OVs} \rightarrow La^{2+}(5d^06s^1) + h^+ \quad (24)$$

$$La^{2+}(5d^06s^1) + O_2 \rightarrow La^{3+}(5d^06s^0) + O_2^{\cdot -} \quad (25)$$

$$MO/\text{phenol} + O_2^{\cdot -}/h^+ \rightarrow CO_2 + H_2O + \ldots \quad (26)$$

Singh and Sharma also reported the Ni-doped Bi_2O_3 synthesized by the chemical precipitation method.[233] They used the doped photocatalyst for the degradation of methylene blue under the illumination of visible light, and Ni dopant served as a trapping energy site for the photogenerated charge carriers, which resulted in greatly enhanced photocatalytic activity of the Bi_2O_3 photocatalyst. Different Bi_2O_3-based photocatalysts are summarized in Table 13.

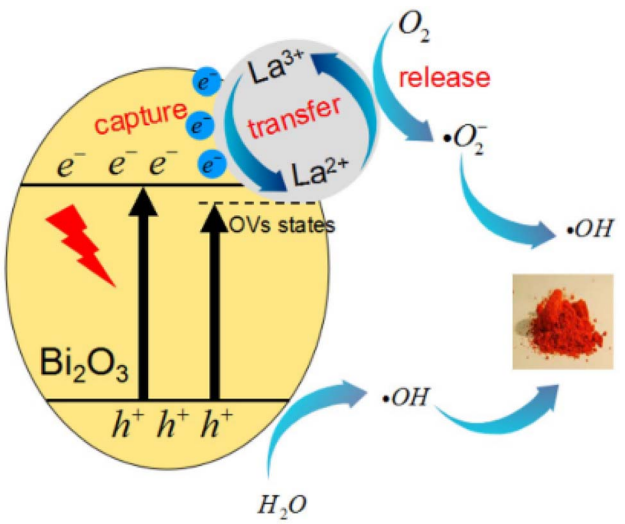

Fig. 14 Proposed schematic photodegradation mechanisms for MO over 2% La-Bi_2O_3 sample under visible light irradiation.[232]

2.4.9 Pb-based oxide photocatalysts. Lead oxide has attracted attention due to its good reactivity, cost-effectiveness, experimental simplicity, and recyclability.[40,246] Lead oxide exists in Pb^{4+} (PbO_2) and Pb^{2+} (PbO) oxidation states. PbO_2 is mainly used as electrode materials in lead–acid battery, which is used in motor vehicles as internal combustion engines.[247] On the other hand, PbO_2 and PbO possess good chemical stability, optical transparency, and micro-hardness, which make them suitable for optoelectronic industry applications.[241,248,249] Lead oxide can also be found in the form including Pb_3O_4, PbO_2, Pb_2O_3 (α, β, and amorphous), and PbO (α, β).[250] PbO nanoparticles have a wide range of applications including energy storage devices, luminescence materials, gas sensors, modifiers in glass, lead crystals, pigments, nanoelectronic devices, lead glazes, UV blockers, pigments, and in decorative potteries.[37,41,251–253] It was also used as a shielding material for gamma radiation protection.[254]

Lead oxide nanoparticles can also be used in photocatalytic degradation.[31–33] However, for photocatalytic applications, PbO is not reported alone but coupled PbO with other semiconductors have been widely reported. The PbO composite with different metal oxide semiconductors has advantages such as shifting the ultraviolet activity of materials to visible light activity by controlling the bandgap and modifying the structure and morphology of the newly formed composite photocatalyst. For instance, Bhachu *et al.*[239] deposited PbO nanoclusters onto titanium dioxide (anatase) polycrystalline films on a glass substrate by the chemical vapor deposition method to form the PbO/TiO_2 composite. The PbO-modified TiO_2 introduced new electronic states above the valence band maximum of TiO_2, which resulted in the enhancement of the photocatalytic activity of TiO_2 in the visible light region. Leelavathi *et al.*[240] designed PbO quantum dot dispersed on anatase TiO_2 to form heterostructures by combining nonhydrolytic sol–gel and combustion methods for the separation of photogenerated charge carriers. They observed that the bare PbO showed very poor photocatalytic activity. They obtained 77% and 50% of the photodegradation percentage of orange G for TiO_2/PbO and TiO_2, respectively, within 2 h.

Table 13 Summary of Bi_2O_3 based photocatalysts for photodegradation of organic pollutants

Catalysts	Synthesis methods	Morphology	Model pollutant	Light	Reaction time	Degradation efficiency	Ref.
α-β Bi_2O_3	Solvothermal	Nanoparticles	Rhodamine B	Visible light	120 min	99.6%	231
La-doped Bi_2O_3	Sol–gel	Nanoparticles	Methyl orange	Visible light	100 min	98%	232
La-doped Bi_2O_3	Sol–gel	Nanoparticles	Phenol	Visible light	100 min	73%	232
Ni-doped Bi_2O_3	Chemical precipitation	Nanoparticles	Methylene blue	Visible light	270 min	81%	233
Bi_2O_3/Bi_2O_4	Calcining raw materials	Flower-like nanoparticles	17α-ethinyl estradiol	Visible light	12 min	~100%	234
TiO_2/Bi_2O_3	Template	Nanoparticles (hollow)	Tetracycline	Visible light	140 min	100%	235
$Cs_2O–Bi_2O_3$–ZnO	Combustions	Nanoparticles (sponge-like structure)	4-Chlorophenol	Simulated sunlight	80 min	98.5%	236
Bi_2O_3/CeO_2	Hydrothermal	Nanoparticles	Orange II dye	Visible light	5 h	—	237
$Bi_2O_3/g-C_3N_4$	Heat treatment	Nanoparticles (spheroidal)	Amido black 10B dye	Xenon	120 min	88.71%	238

PbO has also been used in different metal oxide nanoparticles to modify their photocatalytic activity. Mebed *et al.*[241] prepared PbO–Al_2O_3 nanocomposite by the microwave irradiation method and utilized it for the removal of methylene blue from wastewater under UV-visible or visible light irradiations. Al_2O_3 possesses a very wide bandgap of approximately 9 eV. However, compositing it with PbO made it responsive to visible light irradiation and improves the overall physicochemical properties. Wang *et al.*[242] reported Sb_2O_3/PbO-coupled semiconductor photocatalyst synthesized by the hydrothermal method for the degradation of carbamazepine (CBZ). They selected PbO for coupling with Sb_2O_3 due to its high stiffness, high thermal stability, and high tensile strength. Wang *et al.*[5] synthesized PbO/TiO_2 and Sb_2O_3/TiO_2 photocatalysts for the degradation of UV filter benzophenone-3 under UV-C irradiation, and PbO/TiO_2 completely degraded the UV filter benzophenone-3 within 120 min. They studied the effect of pH by varying it from 3 to 11, and the degradation efficiency at varied pH is shown in Fig. 15a. The degradation rate increased as the pH value increased from 3 to 9 for the photocatalyst with PbO ratio with TiO_2 (1 : 2). However, the degradation rate slightly decreased as pH increased to 11 compared to 9. Fig. 15b represents the schematic of the photocatalytic mechanism of PbO/TiO_2 nanocomposite. Reactive holes (h^+) generated on the surface of PbO and reactive electrons (e^-) generated on the surface of TiO_2 under UV-C irradiation. The photogenerated electrons reduced the dissolved O_2 to superoxide radicals ($O_2^{\bullet-}$). Then, $O_2^{\bullet-}$ radicals undergo the oxidation process with the photogenerated h^+ to produce $^1O_2$, as shown in eqn (27)–(29).

$$PbO/TiO_2 + h\nu \rightarrow TiO_2(e^-) + PbO(h^+) \quad (27)$$

$$(TiO_2)e^- + O_2 \rightarrow O_2^{\bullet-} \quad (28)$$

$$(PbO)h^+ + O_2^{\bullet-} \rightarrow {}^1O_2 \quad (29)$$

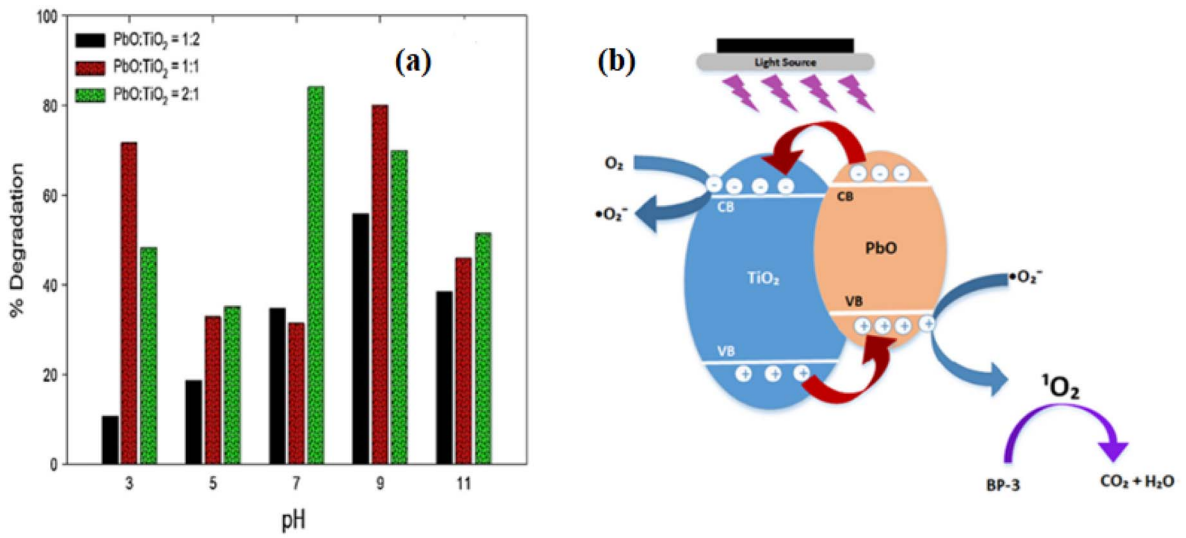

Fig. 15 (a) The photocatalytic degradation of BP-3 by varying the initial pH PbO/TiO_2; (b) mechanism of photocatalytic degradation of BP-3.[5]

Pb-containing metal oxides photocatalyst have also been reported by different groups. For instance, Pourmasoud *et al.*[71] reported $PbWO_4$ synthesized by the coprecipitation method for the degradation of methyl orange from wastewater under UV irradiation and achieved a 97% rate of degradation. Gyawali *et al.*[98] reported an Ag-$PbMoO_4$ photocatalyst synthesized by the sonochemical method for the degradation of Indigo carmine dye under simulated solar light irradiation.

Perovskites containing Pb in their compositions have a potential application in solar energy conversions, but recently, they were studied to use be as photocatalysts. In photocatalysis, perovskites are used as means of energy production and water purification.[255] The combination of PbO with perovskite photocatalysts has also been reported by different scholars. Liu *et al.*[243] synthesized the $PbBiO_2I$/PbO nanocomposite using the hydrothermal method and used it as a photocatalyst for the degradation of crystal violet (CV) dye. According to this report, the formation of a composite between $PbBiO_2I$ and PbO suppresses the rapid recombination of photogenerated electrons–holes pairs and improves the photocatalytic activity of the individual $PbBiO_2I$ and PbO by 3 and 20 times, respectively. The charge carrier transfers and photocatalytic mechanism of the prepared $PbBiO_2I$/PbO are shown in Fig. 16. As one can observe from the depicted Fig. 16, the valence band maximum (VBM) and conduction band minimum (CBM) of $PbBiO_2I$ was higher than that of PbO. Therefore, the photogenerated electrons that occur on the surface of $PbBiO_2I$ could be transferred to the PbO conduction band, whereas holes existing on the surface of PbO can transfer to $PbBiO_2I$. Thus, the charge transfer between the two semiconductors effectively hinders electron–hole recombination, hence improving the photocatalytic efficiency. When electrons and holes reached the CB and VB of $PbBiO_2I$/PbO, the active oxygen species, which degrades the CV, is formed (eqn (30) and (31)). As observed in Fig. 16, in the photosensitized and photocatalytic process, photogenerated and photosensitized electrons react with O_2 on the surface of the photocatalyst and produced superoxide ($O_2^{\bullet -}$). $^1O_2$ is also generated upon the reaction between O_2 and photocatalyst. The combination of perovskites, PbO, and other semiconductors to form heterojunctions has also been reported. Wang *et al.*[256] synthesized $PbBiO_2Br$/PbO/g-C_3N_4 heterojunctions by the hydrothermal method without using a template, and they demonstrated that the enhancement of the photocatalytic activity of this photocatalyst corresponded to the heterojunctions formed between $PbBiO_2Br$, PbO, and g-C_3N_4. Thus, PbO contributes to the enhancement of the photocatalytic activities of this heterojunction.

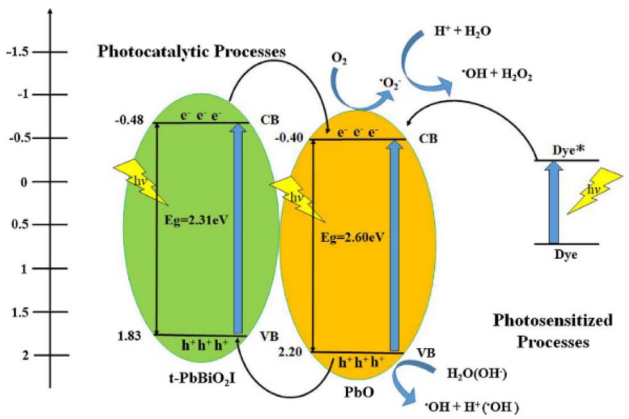

Fig. 16 Schematic illustration of the bandgap structures of *t*-$PbBiO_2I$/PbO.[243]

$$\text{(organic pollutant)CV} + {}^1O_2/h^+ \rightarrow \text{degraded compounds} \quad (30)$$

$$\text{(organic pollutant)}CV^{+\bullet} + O_2^{\bullet -}/{}^1O_2/h^+ \rightarrow \text{degraded compounds} \quad (31)$$

Pb-containing composition of the compounds has also been used for the removal of microbiological contaminants from drinking water. Li *et al.*[257] synthesized Pb-$BiFeO_3$/rGO photocatalyst *via* the hydrothermal method and evaluated the photocatalytic disinfection efficiencies toward Gram-negative *Escherichia coli* (*E. coli*) and Gram-positive *Staphylococcus aureus* (*S. aureus*) under the illumination of visible light. According to

Table 14 Summary of Pb-based photocatalysts for the photodegradation of organic pollutants

Catalysts	Synthesis methods	Morphology	Model pollutant	Light	Reaction time	Degradation efficiency	Ref.
PbO/TiO_2	Chemical vapour deposition	Films	Stearic acid	Visible light	71 h	70%	239
TiO_2/PbO	Sol–gel combustion	Nanocomposites	Orange G	Metal halide lamp	2 h	77%	240
PbO–Al_2O_3	Microwave irradiation	—	Methylene blue	UV	105 min	28%	241
Sb_2O_3/PbO	Hydrothermal	—	Carbamazepine	UV	120 min	—	242
PbO/TiO_2	—	—	Benzophenone-3 under UV		120 min	100%	5
$PbWO_4$	Coprecipitation	Nanoparticles	Methyl orange	UV	100 min	97%	71
Ag-$PbMoO_4$	Sonochemical	Nanoparticles	Indigo carmine	Simulated solar light	120 min	—	98
$PbBiO_2I$/PbO	Hydrothermal	—	Crystal violet	Visible light	24 h	99%	243
Sn doped α-PbO	Chemical precipitation	Nanoparticles	Methylene blue dye	Visible light	100 min	~100%	244

their report, the complete inactivation of *E. coli* and *S. aureus* was achieved within 30 min and 90 min, respectively. In this report, the intercalated Pb coordinate with Bi^{3+} was to provide actives sites for the reaction, hence improving the photocatalytic activity of $BiFeO_3$. Different Pb-based oxide photocatalysts for the photocatalytic degradation of organic pollutants are summarized in Table 14.

2.4.10 Density functional theory (DFT). DFT is a modern calculation widely used in fields such as condensed matter physics, quantum chemistry, and materials science, and it is a practical electronic-structure calculation computational method.[198] DFT is primarily a theory of electronic structure calculations at ground states couched in terms of electron density.[258] The DFT framework provides a computationally easy and controllable way to solve and approximate many-body problems for electrons both in the excited state and ground state.[259] DFT simulation is applied for the study of metal oxides and to understand the improvement of the properties of metal oxides by applying different strategies for different technological applications. To understand the enhancement of metal oxide properties by the DFT method, strategies such as doping with metal or nonmetal, oxygen vacancy, and coupling with other semiconductors to form heterojunctions are among the intensively studied. For instance, Iwaszuk and Nolan studied the PbO and PbO_2 nanoclusters supported on TiO_2 anatase (001) and rutile (110) surface by the first principles DFT method for the modification of the TiO_2 photocatalyst.[260] They investigated the effects of Pb oxidation states on the PbO_x modifications of TiO_2 photocatalysts, which showed a dramatic impact on the nature of band-edge modification of TiO_2 and on the electron–hole separation mechanism. New states were introduced in the pure rutile and anatase when PbO and PbO_2 was adsorbed on the surface of TiO_2. Thus, the adsorbed PbO and PbO_2 nanoclusters induced the visible-light activation of the TiO_2 photocatalyst and predicted the reduction of fast charge recombination.

Islam *et al.*[198] used DFT calculation to investigate the effects of Ce doping into the CuO photocatalyst. After replacing Ce in the place of Cu, the crystal structure of CuO was distorted, and the symmetry of the system was reduced. Due to the distortion of the structure and lack of symmetry, the centers of the negative and positive charges can get separated. Thus, the photocatalytic performance of the Ce-doped CuO was enhanced due to the reduced recombination of the photogenerated electron–hole pairs. The Ce 4f orbital greatly affected the valence and conduction band by introducing defect states near the valence and conduction band. The introduced defect state trapped the photogenerated charges and reduced the fast recombination of photogenerated electrons and holes. They also calculated the real part and imaginary part of the dielectric constant and concluded that the higher the real part of the dielectric, the lower the recombination of photogenerated electrons and holes.

Kitchamsetti *et al.*[261] also used first-principles DFT calculation to identify the formation of O_2 radicals on the surface of NiO (110), which was believed to initiate the degradation of rhodamine B dye. Huang and Hart studied the capability of photocatalytic water splitting of various tungstate oxides by DFT calculations.[262] Singh and Sharma used DFT calculations to investigate the effects of Ni doping into α-Bi_2O_3 on its photocatalytic activities.[233] Pure α-Bi_2O_3 possesses a direct bandgap, as shown in Fig. 17a. However, after Ni was doped, an indirect bandgap bandstructure was obtained, as shown in Fig. 17b. Thus, the Ni-doped α-Bi_2O_3 has an increased charge separation and retarded electron–hole pair's recombination, which was attributed to the time elongation for the charge transit conduction band to the valence band.

Different semiconducting heterojunctions are also studied using DFT to obtain a better understanding of its photocatalytic activities. The construction of heterojunction structures is among the most effective method for improving the efficiency of photocatalysts by accelerating the separation and transport of the electron–hole. When the heterojunction is formed, a potential difference is created between the conduction band and the valence band at the interface. When irradiated electrons can be easily excited, they immediately form electron–hole pairs. Hence, the photogenerated electrons are transferred to the conduction band of other semiconductors rather than recombining with the holes in the valence band. Yao *et al.*[263] reported the DFT studied g-C_3N_4/BiOBr(001) heterojunction for a better understanding of its photocatalytic activity by analyzing the electronic and geometric structures. According to their study, they presented ultrathin g-C_3N_4/BiOBr(001) heterojunction formed by stacking g-C_3N_4 on the top of BiOBr with 3.55 Å of the interlayer distance, as shown in Fig. 18a. In the complete relaxation of the heterojunction, the interaction between the g-C_3N_4 monolayer and the surface of BiOBr resulted in g-C_3N_4 flakes with 2.95 Å interlayer distance, which is the van der Waals distance, as shown in Fig. 18b. Fig. 18c shows the electron localization function of the relaxed g-C_3N_4/BiOBr(001) heterojunction. The strongest position of electron localization is shown by the yellow-colored area. To investigate the reason for a high photocatalytic activity, they calculated the density of states, as shown in Fig. 18d. The optical bandgap of g-C_3N_4 and BiOBr was 2.7 eV and 2.8 eV, respectively. However, the bandgap of the g-C_3N_4/BiOBr(001) heterojunctions was reduced to 1.68 eV, which indicated the high efficiency of charge transfer from the valence band to the conduction band g-C_3N_4/BiOBr. As shown in Fig. 18e, the valence band maxima (VBM) of BiOBr(001) is lower than that of g-C_3N_4, whereas the conduction band minima (CBM) g-C_3N_4 is higher than that of BiOBr(001), as shown in Fig. 18f, which indicates that the g-C_3N_4/BiOBr(001) heterojunction has a typical type-II energy band alignment. This is reasonable for the greater photoresponse to visible light of the g-C_3N_4/BiOBr(001) heterojunction compared to g-C_3N_4 and BiOBr(001).

Moreover, the energy band structure before and after the formation of the heterojunction is shown in a schematic diagram in Fig. 19.[263] As shown in the left of Fig. 19, the energy band edges of both g-C_3N_4 and BiOBr(001) are given before contact formation. Electrons excited from the VB to the CB for g-C_3N_4 and the BiOBr(001) layers under visible light irradiation. As shown in the right of Fig. 19, the g-C_3N_4/BiOBr(001) heterojunction absorbs visible light and electrons excited from the VB

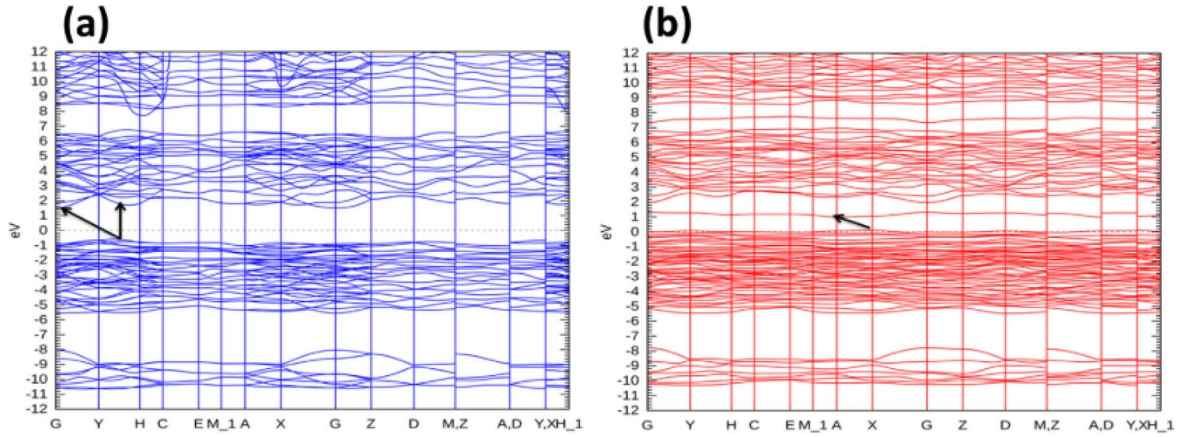

Fig. 17 Electronic bandstructure of (a) α-Bi_2O_3 (b) Ni doped α-Bi_2O_3 at 300 K.[233]

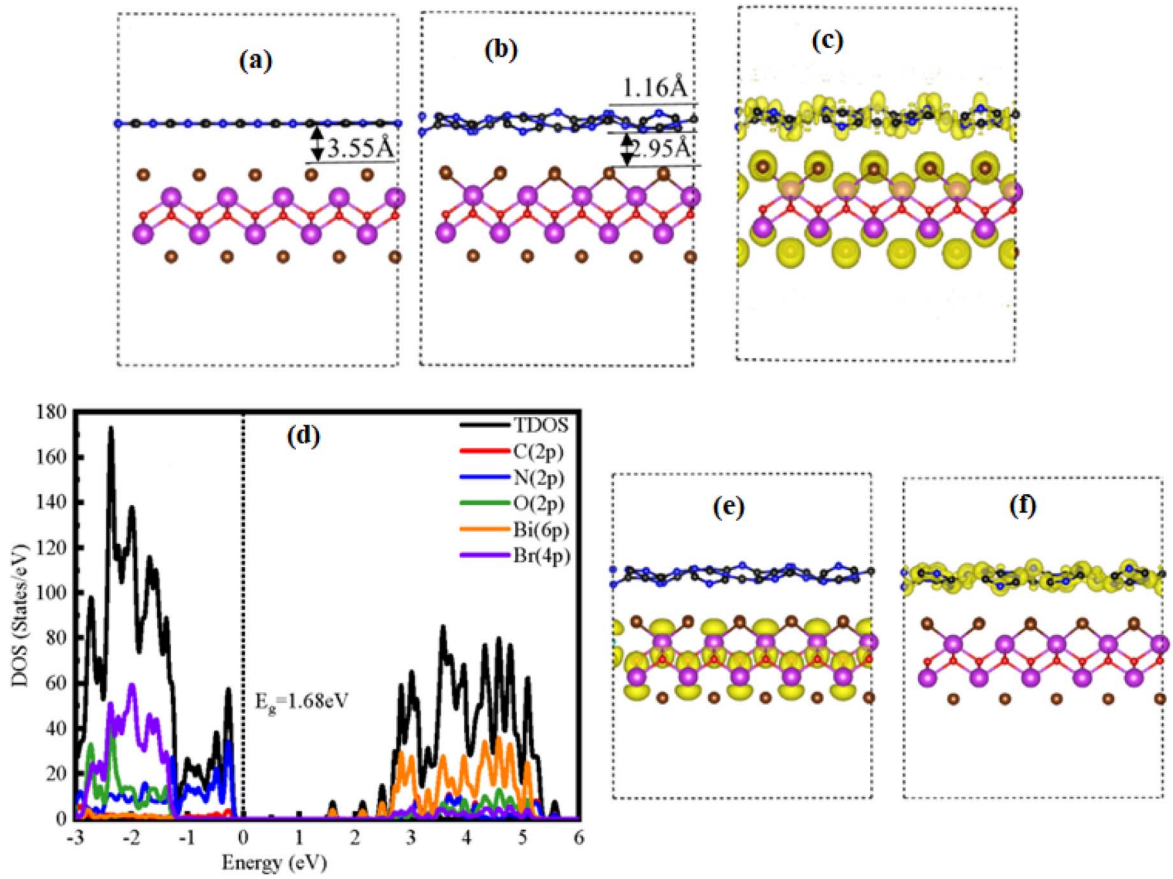

Fig. 18 (a) The heterojunction structure of g-C_3N_4/BiOBr(001) before geometry optimization and (b) after geometry optimization; (c) the electron localization function of g-C_3N_4/BiOBr(001); (d) the calculated TDOS and PDOS of the g-C_3N_4/BiOBr(001) van der Waals heterojunctions; (e) partial charge density of the valence band maxima (VBM) for g-C_3N_4/BiOBr(001) heterojunction and (f) the conduction band minima (CBM) for the g-C_3N_4/BiOBr(001) heterojunction.[263]

to CB, leaving holes behind in the valence band. Some of the photogenerated electrons by the g-C_3N_4 layer were transferred to the CB of BiOBr(001), while some of the photogenerated holes by BiOBr(001) were transferred to the VB of g-C_3N_4. This process resulted in the effective separation of photogenerated electrons and holes at the different surfaces by the built-in electric field. Thus, the fast recombination of photogenerated electrons and holes is reduced, and the photocatalytic performance will be improved efficiently. Oktavianti *et al.*[264] also used the DFT method to study the adsorption of methylene blue dye on Ni-doped ZnO clusters. They investigated the adsorption interaction between methylene blue dye and pure ZnO or Ni-

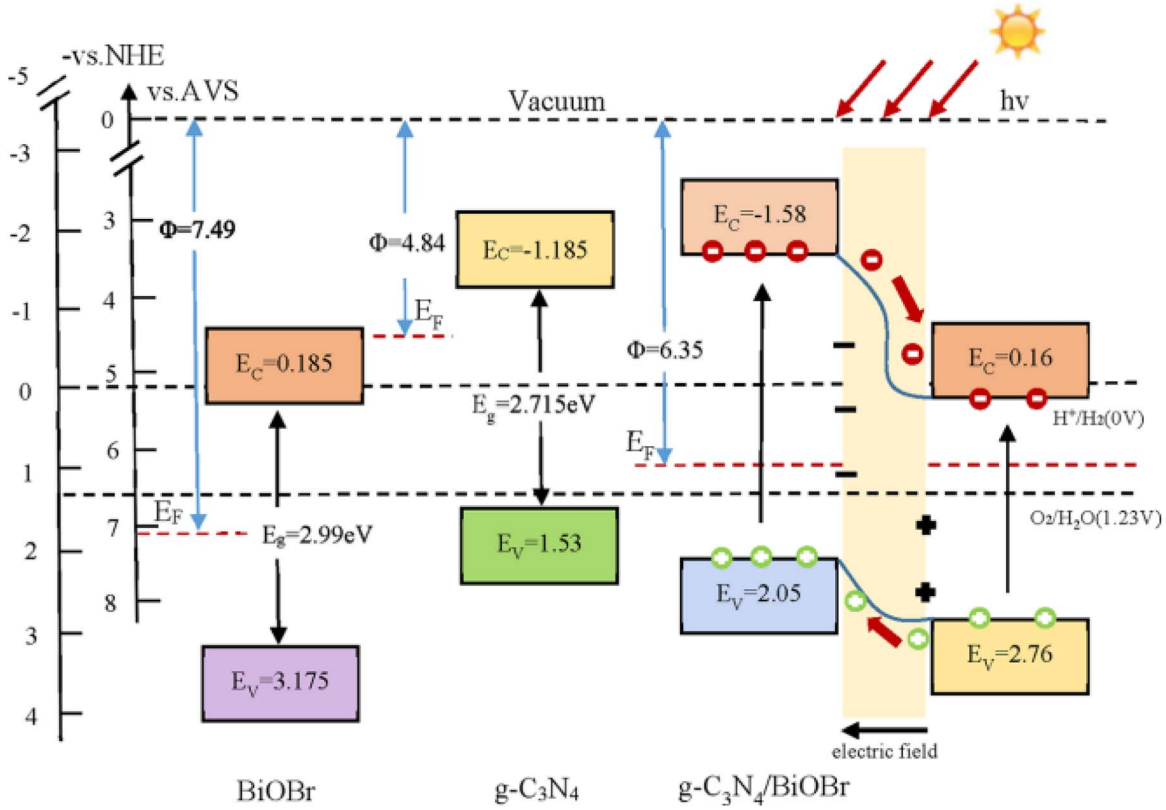

Fig. 19 Schematic diagram of the energy band edge positions before and after the contact between g-C_3N_4 and BiOBr(001) and the charge separation at the interface of C_3N_4/BiOBr(001) under visible light irradiation, where Φ is the work function, E_C is the bottom of the CB, E_V is the top of the VB, and E_g is the bandgap.[263]

doped ZnO in terms of bond length, energy gap, adsorption energy, and Mulliken charge transfer to evaluate the adsorption of ZnO or Ni-doped ZnO toward methylene blue dye.

2.5 Parameters effecting the photocatalytic degradation

2.5.1 Effect of pH. The pH of the reaction in the photocatalysis process significantly affects the photodegradation rate of pollutants. The pH of the reaction solution affects the photocatalysts' surface charge, adsorption of contaminants to the photocatalyst's surface, the degree of ionizations, photocatalysts valence band oxidation potential, and agglomeration.[265] If the pH of the solution increases beyond the isoelectronic point of the catalyst, the negative charge is induced onto the photocatalyst surface and the negatively charged photocatalyst surface attracts cationic pollutants from the aqueous solution. This affects the concentration of electrons transferred between the catalysts and pollutants for degradation. However, if the pH decreases below the zero-point charge of the photocatalyst, the photocatalyst surface is positively charged and attracts anion pollutants. Adeel *et al.*[6] varied the pH of the solution in the range of 2–10 by fixing the CoZnO dosage to 0.05 g and methyl orange solution to 100 mg L^{-1}. Below the pH point of zero charge, the surface of ZnO is negatively charged, whereas above the point of zero charge, it is positively charged. Methyl orange is an anion in acidic conditions; therefore, the lower pH value is favored for the adsorption of methyl orange on the surface of positively-charged ZnO surface due to electrostatic attraction. The high percentage of methyl orange is degraded at lower pH, whereas the percentage of degradation decreased at higher pH due to electrostatic repulsion. At very low pH, the strongly acidic condition dissolves ZnO; hence, the percentage degradation decreases.

Shelar *et al.*[266] studied the effects of pH on the degradation of methylene blue dye of 50 mg L^{-1} concentration in the pH range from 2 to 12 in the presence of 1 g L^{-1} Ag-doped ZnO photocatalyst, as shown in Fig. 20. The photodegradation efficiency increases as the pH value increases from 2 to 8. At pH 8, the highest photodegradation efficiency is observed. However, as the pH value further increases from 9 to 12, the photodegradation efficiency decreases, as observed in Fig. 20. Thus, pH 8 is the optimum value for the highest degradation of methylene blue dye for the Ag-doped ZnO photocatalyst. At pH of zero-point charge = 7.6, the catalyst has zero charges; hence, the surface catalyst becomes positively charged at pH less than 7.6 and becomes negatively charged at pH greater than 7.6. Methylene blue dye is a cation dye; therefore, it is attracted to the surface of negatively-charged catalysts for the photodegradation to be higher. For a pH greater than 8, the photocatalytic degradation is decreased because there is electrostatic repulsion between the negatively charged catalyst surface and hydroxide anions. This could inhibit the generation of $^{\bullet}OH$

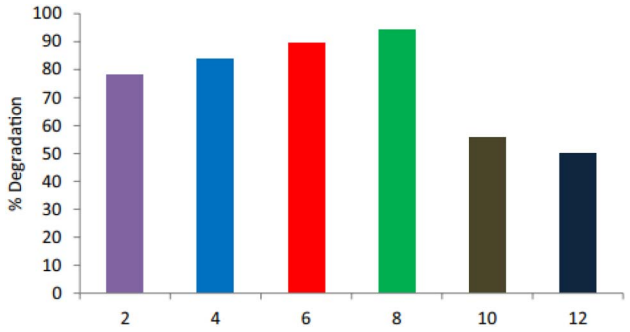

Fig. 20 Effect of pH on the photocatalytic degradation of Methylene blue dye.[266]

radicals, hence decreasing the percentage degradation of methylene blue dye.

Mohagheghian *et al.*[267] investigated the effects of pH on the percentage degradation of Acid Orange 7 (10 mg L^{-1}) using tungsten oxide nanopowder (1 g L^{-1}) by varying the pH values from 3 to 9, as shown in Fig. 21. At pH zero, point charge was 5.09 and pH greater than 5.09 makes the catalyst surface negatively charged, whereas pH lower than 5.09 makes the surface of catalyst positively charged. The negatively charged surface prevents the adsorption of anion dyes and hydroxide anions onto the catalyst surface. Therefore, the highest degradation efficiency of Acid Orange 7 was observed at pH 3.

2.5.2 Effect of catalyst dosage. Photocatalyst dosages also have significant effects on the photodegradation rates of pollutants. To avoid the unnecessary utilization of photocatalysts, optimizing the amount of catalyst is essentially important. By increasing the catalyst dosage, the amount of photodegradation of dye increases. Thus, the number of active species increases with increasing catalyst dosage. Beyond a certain limit of catalyst dosage, the aqueous solution becomes cloudy and blocks the light radiation, and the photodegradation efficiency of the dye decreases. Adeel *et al.*[6] reported Co–ZnO synthesized by the precipitation method and utilized for the degradation of methyl orange under visible

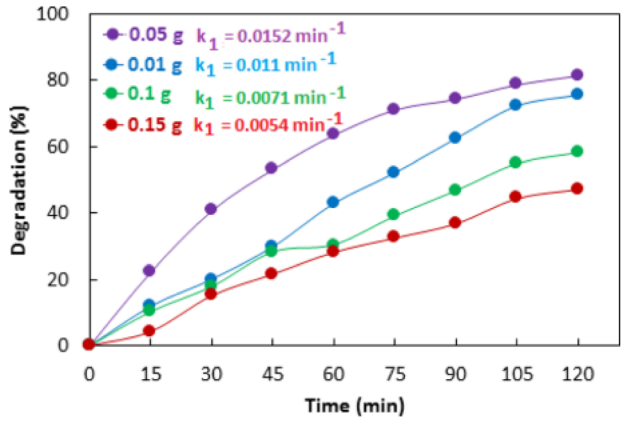

Fig. 21 Effect of pH on the photocatalytic degradation of Acid Orange 7.[267]

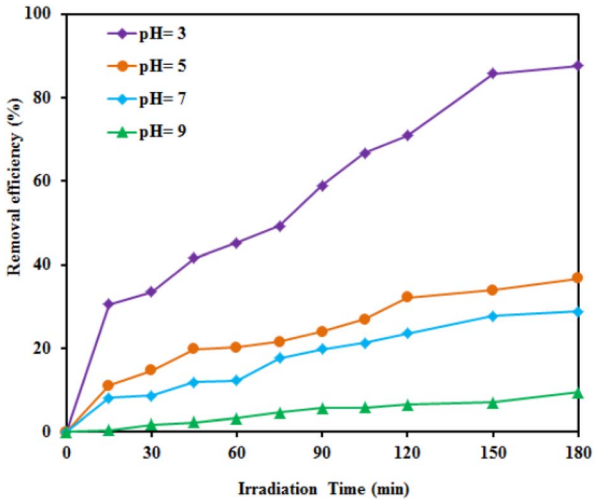

Fig. 22 Effect of the catalyst dose on the photodegradation of methyl orange catalyzed by Co–ZnO.[6]

light. They reported the effects of catalyst dose, pH, temperature, and dye concentration on the percentage degradation of methyl orange. Among these parameters, the effect of catalyst dosage is shown in Fig. 22. They varied the catalyst dosage in the range of 0.01–0.15 g for the photodegradation of 100 mg L^{-1} concentration methyl orange for 120 min. As shown in Fig. 22, the percentage degradation of methyl orange increases as the catalyst dosage increases from 0.01 to 0.05 g and decreases as the catalyst dosage further increases. The decrease in the percentage degradation while the catalyst dosage increases is attributed (i) to the nonhomogeneity of the reaction mixture at a given speed of agitation and (ii) inhibits penetration light to the interior of the solution. Hence, the number of active centers is nonaccessible; consequently, the percentage degradation decreases. Among all catalyst dosages, 0.05 g obtained the largest kinetic rate constant; therefore, it is the optimum dosage for the photodegradation of methyl orange with 100 mg L^{-1} concentration.

2.5.3 Effect of dye concentration. The photocatalysis process is dependent on the pollutants adsorbed onto the photocatalyst surface. In photodegradation, only the amount of dyes adsorbed onto the surface of the photocatalyst contributes to the photocatalysis process.[268] As the concentration of the dye increases, large amounts of dyes are adsorbed onto the photocatalyst surface, while less number of lights reach the photocatalyst surface. Thus, lesser number of active oxidation species is generated, and the photodegradation efficiency decreases. I. Ahmad synthesized different metals (Al, Mg, Ni, Cu, and Ag)-doped ZnO/g-C_3N_4 *via* a one-pot pyrolysis technique and utilized it for the degradation of EBT dye.[169] He named his samples as pure ZnO, g-C_3N_4, Al-doped ZnO/g-C_3N_4, Mg-doped ZnO/g-C_3N_4, Ni-doped ZnO/g-C_3N_4, Cu doped ZnO/g-C_3N_4, and Ag-doped ZnO/g-C_3N_4 with sample coding PZO, GCN, AZGC1, MZGC2, NZGC3, CZGC4, and AZGC5, respectively. He studied the effects of different parameters such as different catalyst effects, catalyst dosage effects, and effects of dye concentration

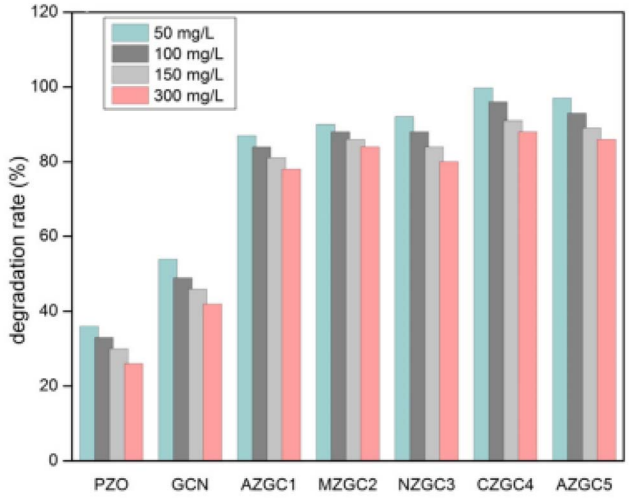

Fig. 23 Effect of dye concentration on photocatalytic EBT dye degradation catalyzed by metals-doped ZnO/g-C_3N_4.[169]

on the photodegradation efficiency of EBT dye. He evaluated the photocatalytic performance as a function of EBT dye by varying concentrations 50–300 mg L^{-1} while keeping other experimental conditions constant. As shown in Fig. 23, the percentage of photodegradation decreases as the dye concentration increases in all the samples. Thus, the adsorption of a large number of dyes on the photocatalyst surface decreases the adsorption of OH^- and also decreases the penetration length of light, which consequently decreases the generation of $^{\cdot}OH$ radical, hence decreasing the percentage degradation.

2.5.4 Effect of irradiation time. It is obvious that if irradiation time increases the rate of degradation efficiency increases. Fig. 24 shows the percentage degradation of methylene blue dye under UV light irradiation time from 0 to 150 min in the presence of ZnO-Fe_x (x & 0, 0.05, 0.075, 0.1 mol%) nanoparticles. In Fe dopant concentration, the percentage degradation of methylene blue dye increases as the irradiation time increases.[269] Among all the doped materials, Fe (0.075%)-doped ZnO shows the highest degradation efficiency in a short time compared to other Fe dopant concentrations.

2.5.5 Effect of oxidizing agent. Oxidizing agents such as ammonium persulphate, potassium bromate, and hydrogen peroxide have a great influence on the photocatalytic degradation of organic pollutants.[270] Saquib *et al.*[271] demonstrated the influence of H_2O_2, $KBrO_3$, and $(NH_4)_2S_2O_8$ oxidizing agents on the photocatalytic degradation of Patent Blue VF and Fast Green FCF in the presence of titanium dioxide (Hombikat UV100 and Degussa P25) as the photocatalysts. Their result revealed that Hombikat UV100 photocatalyst had more efficient degradation for Fast green FCF in the presence of $KBrO_3$ and $(NH_4)_2S_2O_8$ as oxidizing agents, whereas Degussa P25 for the better degradation of Patent Blue VF. They used these three chemicals as electron acceptors.

2.5.6 Effect of intensity of light. The intensity and wavelength of light influence the photocatalytic degradation of dyes in aqueous solution in the presence of photocatalysts.[272] For a photocatalytic reaction to take place, the semiconductor used as a photocatalyst must absorb light to initiate the reaction. The bandgap of the photocatalyst should be equal to or greater than the irradiated light. With the increase in the intensity of light, there is a chance for more electrons to be generated, which increases the number of oxidation species. The irradiated light is either UV or visible light. The UV light has high intensity and is hugely applied in the photocatalytic degradation of textile dyes. It is more utilized for photocatalysts with wide optical bandgap such as TiO_2 and ZnO. However, due to its cost-effectiveness and abundance, visible light is used as an alternative to UV light. Neppolian *et al.*[273] used both UV and visible for the degradation of Reactive Red 2, Reactive Yellow 17, and Reactive Blue 4 dyes catalyzed by TiO_2. They identified that UV irradiation was more effective than solar irradiation in dye degradation because UV has larger energy than solar light; hence, the electron–hole recombination is suppressed in UV

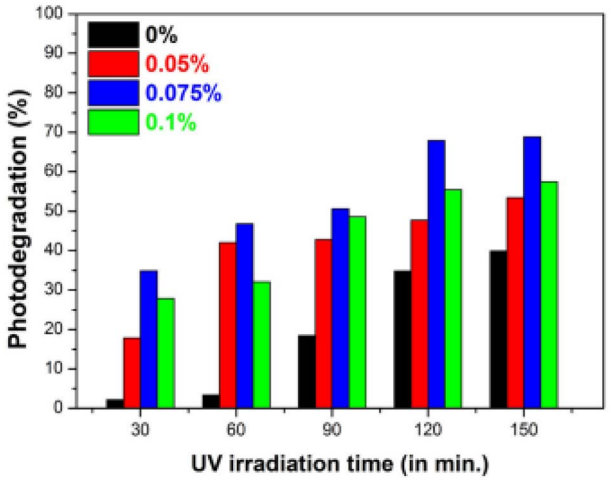

Fig. 24 Influence on the photodegradation of methylene blue dye Fe-doped ZnO catalyst at different irradiation times.[269]

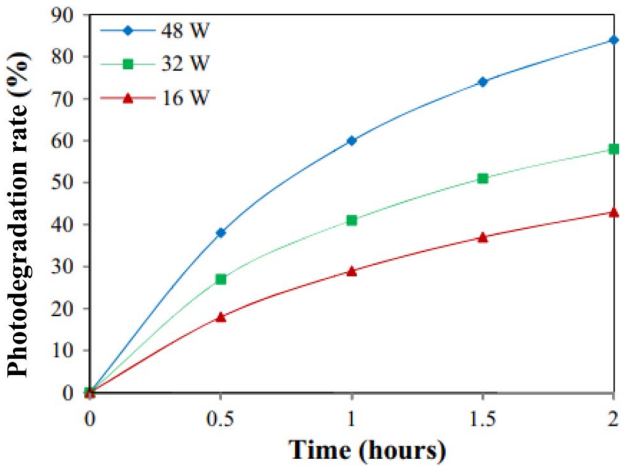

Fig. 25 Effect of light intensity on the photocatalytic degradation rate of phenol using the ZnO@SiO_2 photocatalyst.[274]

irradiation. Galedari *et al.*[274] varied the intensity of light from 16 to 48 W to examine the influence of light intensity on the degradation of methylene blue dye using ZnO@SiO_2 photocatalyst under UV light irradiation. They found an increase in the photodegradation efficiency with an increase in illumination intensity and wavelength of the light source, as shown in Fig. 25. The increase in the degradation efficiency with the intensity of light can be due to the efficiency number of electrons stimulated, which leads to an increase in the generation of hydroxyl radicals.

3 Conclusion and future perspective

In this review, various metal oxide nanoparticles studied by experimental and computational methods for photocatalysis applications are comprehensively overviewed. It is obvious that in this century, the energy crisis and environmental pollution are the main problems the world faces. Nevertheless, researchers around the world are searching for a way to solve these two problems. Photocatalysis technology is a promising technique to overcome the energy crisis and environmental pollution due to its simple, ecofriendly, and green method. In photocatalytic technology, metal oxides are used as a catalyst for the breakdown or decomposition of different organic contaminants, various dyes, and harmful viruses and fungi using ultraviolet or visible light solar spectrum irradiations. One of the attractive properties of oxide materials for photocatalysis is their stability in various conditions. In addition to this, their bandgap can be easily engineered using simple techniques such as doping, composite, and heterojunction, which makes them highly selective for photocatalytic applications. Generally, their light absorption properties, biocompatibility, stability, electronic structure, charge transfer behaviors, and capability of generating charge carriers of the metal oxides have made them selective for photocatalytic applications. Despite the successful achievements of using metal oxides as a photocatalyst, the major drawbacks including the high recombination rate of photogenerated electron–hole pairs, the ultraviolet light activity limitations, and low surface coverage are the bottlenecks. Various strategies such as doping with metals or nonmetals, combining photocatalysts with other materials, morphology controlling, immobilizing with polymer or noble metals, Z-scheme heterostructures, and compositing with carbon-based materials are used to solve the aforementioned drawbacks. However, further work is needed to improve the existing or to discover new materials for photocatalytic applications. In addition to this, among the listed strategies, the most effective one for the practical application of photocatalysis is needed to be identified. On the other hand, the ecotoxicity of the photocatalysts and the clear separation of the photocatalysts from the treated water need more attention. Another issue that needs to be identified is the type of reactive species during the photocatalytic activity. Thus, many articles used scavengers to identify the type of active species that participated in the photocatalytic degradation process; however, it needs more investigation for the identification of active species during the photodegradation process. Generally, for organic pollutant degradation, an important concern that needs to be addressed is improving the response under the irradiation of visible solar light. Thus, for the degradation of organic contaminants efficiently, economically viable, greener, and faster approaches required a significant development in the sustainable degradation of organic pollutants and creating a clean environment for living creatures. Finally, the density functional theory (DFT) method can be used to understand and discover new materials for photocatalytic applications because it is a simple method to search for new materials in photocatalytic applications without using chemicals as raw materials that reduce the cost. Therefore, DFT is recommended to search for new materials that will be used as photocatalyst materials or predicting the way to improve the discovered metal oxides by understanding the properties of materials. Finally, since metal oxide-based heterojunction photocatalysts are showing promising efficiency under visible light, it is suggested that researchers should develop and design new oxide-based heterojunction photocatalysts for photocatalytic degradations.

Author contributions

Fikadu Takele Geldasa: conceptualization and writing – original draft. Mesfin Abayneh Kebede: supervision, Megersa Wodajo Shura: provisioning resources. Fekadu Gashaw Hone: conceptualization, supervision and editing.

Conflicts of interest

There are no conflicts to declare.

Acknowledgements

We acknowledge Adama Science and Technology University and Oda Bultum University for their financial support. Dr Fekadu Gashaw thanks Addis Ababa University for thematic research project (Grant ref. LT/PY-242/2021) grant.

References

1 U. Qumar, J. Z. Hassan, R. A. Bhatti, A. Raza, G. Nazir, W. Nabgan and M. Ikram, *J. Mater. Sci. Technol.*, 2022, **131**, 122–166.
2 A. Touati, T. Hammedi, W. Najjar, Z. Ksibi and S. Sayadi, *J. Ind. Eng. Chem.*, 2016, **35**, 36–44.
3 N. Olama, M. Dehghani and M. Malakootian, *Appl. Water Sci.*, 2018, **8**, 1–12.
4 A. Kushniarou, I. Garrido, J. Fenoll, N. Vela, P. Flores, G. Navarro, P. Hellín and S. Navarro, *Chemosphere*, 2019, **214**, 839–845.
5 Z. Wang, A. Deb, V. Srivastava, S. Iftekhar, I. Ambat and M. Sillanpää, *Sep. Purif. Technol.*, 2019, **228**, 1–13.
6 M. Adeel, M. Saeed, I. Khan, M. Muneer and N. Akram, *ACS Omega*, 2021, **6**, 1426–1435.
7 Q. Li, Z. Chen, H. Wang, H. Yang, T. Wen, S. Wang, B. Hu and X. Wang, *Sci. Total Environ.*, 2021, **792**, 148546.

8 H. Ben Slama, A. C. Bouket, Z. Pourhassan, F. N. Alenezi, A. Silini, H. Cherif-Silini, T. Oszako, L. Luptakova, P. Golińska and L. Belbahri, *Appl. Sci.*, 2021, **11**, 1–21.
9 R. Al-Tohamy, S. S. Ali, F. Li, K. M. Okasha, Y. A. G. Mahmoud, T. Elsamahy, H. Jiao, Y. Fu and J. Sun, *Ecotoxicol. Environ. Saf.*, 2022, **231**, 113160.
10 M. T. Uddin, M. E. Hoque and M. Chandra Bhoumick, *RSC Adv.*, 2020, **10**, 23554–23565.
11 M. Mehrjouei, S. Müller and D. Möller, *Chem. Eng. J.*, 2015, **263**, 209–219.
12 V. O. Ndabankulu, S. Maddila and S. B. Jonnalagadda, *Can. J. Chem.*, 2019, 1–10.
13 M. Zhou, X. Tian, H. Yu, Z. Wang, C. Ren, L. Zhou, Y. W. Lin and L. Dou, *ACS Omega*, 2021, **6**, 26439–26453.
14 M. Mishra and D. M. Chun, *Appl. Catal., A*, 2015, **498**, 126–141.
15 M. M. Khan, S. F. Adil and A. Al-Mayouf, *J. Saudi Chem. Soc.*, 2015, **19**, 462–464.
16 M. Muthukumaran, G. Gnanamoorthy, P. Varun Prasath, M. Abinaya, G. Dhinagaran, S. Sagadevan, F. Mohammad, W. C. Oh and K. Venkatachalam, *Mater. Res. Express*, 2020, **7**, 015038.
17 Y. Boyjoo, H. Sun, J. Liu, V. K. Pareek and S. Wang, *Chem. Eng. J.*, 2017, **310**, 537–559.
18 S. Sood, A. Umar, S. K. Mehta and S. K. Kansal, *J. Colloid Interface Sci.*, 2015, **450**, 213–223.
19 D. Zhu and Q. Zhou, *Environ. Nanotechnol., Monit. Manage.*, 2019, **12**, 100255.
20 A. Mehtab, J. Ahmed, S. M. Alshehri, Y. Mao and T. Ahmad, *Nanotechnology*, 2022, **33**, 142001.
21 A. H. Zahid and Q. Han, *Nanoscale*, 2021, **13**, 17687–17724.
22 J. Luo, S. Zhang, M. Sun, L. Yang, S. Luo and J. C. Crittenden, *ACS Nano*, 2019, **13**, 9811–9840.
23 T. Ma, C. Yang, L. Guo, R. A. Soomro, D. Wang, B. Xu and F. Fu, *Appl. Catal., B*, 2023, **330**, 122643.
24 D. Ayodhya and G. Veerabhadram, *Mater. Today Energy*, 2018, **9**, 83–113.
25 S. Yadav, K. Shakya, A. Gupta, D. Singh, A. R. Chandran, A. Varayil Aanappalli, K. Goyal, N. Rani and K. Saini, *Environ. Sci. Pollut. Res.*, 2022, **30**, 71912–71932.
26 A. B. Djurišić, Y. H. Leung and A. M. Ching Ng, *Mater. Horiz.*, 2014, **1**, 400–410.
27 S. Sukumar, A. Rudrasenan and D. Padmanabhan Nambiar, *ACS Omega*, 2020, **5**, 1040–1051.
28 M. S. S. Danish, L. L. Estrella, I. M. A. Alemaida, A. Lisin, N. Moiseev, M. Ahmadi, M. Nazari, M. Wali, H. Zaheb and T. Senjyu, *Metals*, 2021, **11**, 80.
29 C. Siriwong, N. Wetchakun, B. Inceesungvorn, D. Channei, T. Samerjai and S. Phanichphant, *Prog. Cryst. Growth Charact. Mater.*, 2012, **58**, 145–163.
30 M. Nafees, M. Ikram and S. Ali, *Appl. Nanosci.*, 2017, **7**, 399–406.
31 A. V. Borhade, B. K. Uphade and D. R. Tope, *J. Chem. Sci.*, 2013, **125**, 583–589.
32 A. V Borhade, D. R. Tope and B. K. Uphade, *E-J. Chem.*, 2012, **9**, 705–715.
33 W. Li, H. Yang and Q. Liu, *J. Nanomater.*, 2017, **2017**, 1–8.
34 V. Mirzajani, K. Farhadi and S. M. Pourmortazavi, *J. Therm. Anal. Calorim.*, 2018, **131**, 937–948.
35 M. S. Chavali and M. P. Nikolova, *SN Appl. Sci.*, 2019, **1**, 1–30.
36 S. Wang, Z. Wang and Z. Zha, *Dalton Trans.*, 2009, 9363.
37 A. Aliakbari, E. Najafi, M. M. Amini and S. W. Ng, *Monatsh. Chem.*, 2014, **145**, 1277–1285.
38 İ. K. Akbay, A. Güngör, R. Genç and T. Özdemir, *Selcuk Univ. J. Eng. Science Technol.*, 2019, **7**, 298–308.
39 A. Güngör, R. Genç and T. Özdemir, *J. Turk. Chem. Soc., Sect. A*, 2017, **4**, 1017–1030.
40 R. Tayebee, B. Maleki and M. sabeti, *J. Iran. Chem. Soc.*, 2017, **14**, 1179–1188.
41 S. Yazdani Darki, M. Eslami-Kalantari, H. Zare and Z. Shahedi, *Mater. Chem. Phys.*, 2021, **262**, 124305.
42 Y. Wang and Y. Xia, *Nano Lett.*, 2004, **4**, 2047–2050.
43 N. Baig, I. Kammakakam, W. Falath and I. Kammakakam, *Mater. Adv.*, 2021, **2**, 1821–1871.
44 V. Galstyan, M. P. Bhandari, V. Sberveglieri, G. Sberveglieri and E. Comini, *Chemosensors*, 2018, **6**, 1–21.
45 D. Bokov, A. Turki Jalil, S. Chupradit, W. Suksatan, M. Javed Ansari, I. H. Shewael, G. H. Valiev and E. Kianfar, *Adv. Mater. Sci. Eng.*, 2021, **2021**, 1–21.
46 E. M. Modan and A. G. Plăiaşu, *Ann. "Dunarea Jos" Univ. Galati. Fascicle IX, Metall. Mater. Sci.*, 2020, **43**, 53–60.
47 P. G. Jamkhande, N. W. Ghule, A. H. Bamer and M. G. Kalaskar, *J. Drug Delivery Sci. Technol.*, 2019, **53**, 101174.
48 A. Pohl, *Water, Air, Soil Pollut.*, 2020, **231**, 503.
49 D. A. Alromi, S. Y. Madani and A. Seifalian, *Polymers*, 2021, **13**, 1–26.
50 R. Medhi, M. D. Marquez and T. R. Lee, *ACS Appl. Nano Mater.*, 2020, **3**, 6156–6185.
51 H. Chakhtouna, H. Benzeid, N. Zari, A. el kacem Qaiss and R. Bouhfid, *Environ. Sci. Pollut. Res.*, 2021, **28**, 44638–44666.
52 M. Parashar, V. K. Shukla and R. Singh, *J. Mater. Sci.: Mater. Electron.*, 2020, **31**, 3729–3749.
53 R. Mahdavi and S. S. A. Talesh, *Adv. Powder Technol.*, 2017, **28**, 1418–1425.
54 M. V. Arularasu, *SN Appl. Sci.*, 2019, **1**, 393.
55 S. Liu, X. Wei, S. Lin and M. Guo, *J. Sol-Gel Sci. Technol.*, 2021, **99**, 122–131.
56 F. Heshmatpour and R. B. Aghakhanpour, *Powder Technol.*, 2011, **205**, 193–200.
57 H. Siddiqui, M. R. Parra, M. M. Malik and F. Z. Haque, *Opt. Quantum Electron.*, 2018, **50**, 260.
58 L. F. de S. Lima, C. R. Coelho, G. H. M. Gomes and N. D. S. Mohallem, *J. Sol-Gel Sci. Technol.*, 2020, **93**, 168–174.
59 M. Patel, S. Mishra, R. Verma and D. Shikha, *Discov. Mater.*, 2022, **2**, 1.
60 S. Ahmadi, N. Asim, M. A. Alghoul, F. Y. Hammadi, K. Saeedfar, N. A. Ludin, S. H. Zaidi and K. Sopian, *Int. J. Photoenergy*, 2014, **2014**, 1–21.
61 A. Serrà and E. Vallés, *Catalysts*, 2018, **8**, 395.

62 J. Abel, A. Pramothkumar, N. Senthilkumar, K. Jothivenkatachalam, P. Fermi Hilbert Inbaraj and J. Joseph prince, *Phys. Rev. B*, 2019, **572**, 117–124.
63 S. Jamil, S. R. Khan, B. Sultana, M. Hashmi, M. Haroon and M. R. S. A. Janjua, *J. Cluster Sci.*, 2018, **29**, 1099–1106.
64 M. G. Kotresh, M. K. Patil and S. R. Inamdar, *Optik*, 2021, **243**, 167506.
65 P. Yadav, R. Saini and A. Bhaduri, *Environ. Sci. Pollut. Res.*, 2022, **30**, 71439–71453.
66 A. Helal, S. M. El-Sheikh, J. Yu, A. I. Eid, S. A. El-Haka and S. E. Samra, *J. Nanopart. Res.*, 2020, **22**, 132.
67 M. Kandasamy, A. Seetharaman, D. Sivasubramanian, A. Nithya, K. Jothivenkatachalam, N. Maheswari, M. Gopalan, S. Dillibabu and A. Eftekhari, *ACS Appl. Nano Mater.*, 2018, **1**, 5823–5836.
68 D. Liang, S. Liu, Z. Wang, Y. Guo, W. Jiang, C. Liu, H. Wang, N. Wang, W. Ding, M. He, L. Wang and S. Xu, *J. Mater. Sci.: Mater. Electron.*, 2019, **30**, 12619–12629.
69 B. Uma, K. S. Anantharaju, L. Renuka, S. Malini, S. S. More, Y. S. Vidya and S. Meena, *Ceram. Int.*, 2021, **47**, 10355–10369.
70 B. A. Lemecho, F. K. Sabir, D. M. Andoshe, N. S. Gultom, D. H. Kuo, X. Chen, E. Mulugeta, T. D. Desissa and O. A. Zelekew, *Bioinorg. Chem. Appl.*, 2022, **2022**, 1–10.
71 S. Pourmasoud, M. Eghbali-Arani, F. Ahmadi and M. Rahimi-Nasrabadi, *J. Mater. Sci.: Mater. Electron.*, 2017, **28**, 17089–17097.
72 W. Buraso, V. Lachom, P. Siriya and P. Laokul, *Mater. Res. Express*, 2018, **5**, 1–10.
73 W. M. Rangel, R. A. A. Boca Santa and H. G. Riella, *J. Mater. Res. Technol.*, 2020, **9**, 994–1004.
74 Y. X. Gan, A. H. Jayatissa, Z. Yu, X. Chen and M. Li, *J. Nanomater.*, 2020, **2020**, 1–3.
75 S. K. Godlaveeti, A. R. Somala, S. S. Sana, M. Ouladsmane, A. A. Ghfar and R. R. Nagireddy, *J. Cluster Sci.*, 2022, **33**, 1635–1644.
76 A. M. Shahat, F. M. El-Hossary, A. Ghitas, A. M. Abd El-Rahman and A. A. Ebnalwaled, *IOP Conf. Ser.: Mater. Sci. Eng.*, 2021, **1171**, 012008.
77 M. R. Abhilash, A. Gangadhar, J. Krishnegowda, M. Chikkamadaiah and S. Srikantaswamy, *RSC Adv.*, 2019, **9**, 25158–25169.
78 M. Khashaei, L. Kafi-Ahmadi, S. Khademinia, A. Poursattar Marjani and E. Nozad, *Sci. Rep.*, 2022, **12**, 1–15.
79 W. Wei, X. Yue, H. Cui, X. Lü and J. Xie, *J. Mater. Res.*, 2013, **28**, 3408–3416.
80 B. R. Bade, S. R. Rondiya, Y. V. Hase, M. P. Nasane, S. B. Jathar, S. V. Barma, K. B. Kore, D. S. Nilegave, S. R. Jadkar and A. M. Funde, *AIP Conf. Proc.*, 2021, **2335**, 100001.
81 S. Suthakaran, S. Dhanapandian, N. Krishnakumar and N. Ponpandian, *Mater. Res. Express*, 2019, **6**, 0850i3.
82 S. S. Low, M. Yew, C. N. Lim, W. S. Chai, L. E. Low, S. Manickam, B. T. Tey and P. L. Show, *Ultrason. Sonochem.*, 2022, **82**, 105887.
83 B. Savun-Hekimoğlu, *Acoustics*, 2020, **2**, 766–775.
84 M. A. Dheyab, A. A. Aziz and M. S. Jameel, *Molecules*, 2021, **26**, 2453.
85 S. Stankic, S. Suman, F. Haque and J. Vidic, *J. Nanobiotechnol.*, 2016, **14**, 1–20.
86 K. Wongwailikhit and S. Horwongsakul, *Mater. Lett.*, 2011, **65**, 2820–2822.
87 Y. Shlapa, V. Sarnatskaya, I. Timashkov, L. Yushko, I. Antal, B. Gerashchenko, I. Nychyporenko, A. Belous, V. Nikolaev and M. Timko, *Appl. Phys. A: Mater. Sci. Process.*, 2019, **125**, 1–10.
88 Y. Du, W. Wang, X. Li, J. Zhao, J. Ma, Y. Liu and G. Lu, *Mater. Lett.*, 2012, **68**, 168–170.
89 Ö. A. Yildirim and C. Durucan, *J. Alloys Compd.*, 2010, **506**, 944–949.
90 M. H. Zori, *J. Inorg. Organomet. Polym. Mater.*, 2011, **21**, 81–90.
91 A. Kumar, A. Saxena, A. De, R. Shankar and S. Mozumdar, *RSC Adv.*, 2013, **3**, 5015–5021.
92 J. Guo, S. Zhu, Z. Chen, Y. Li, Z. Yu, Q. Liu, J. Li, C. Feng and D. Zhang, *Ultrason. Sonochem.*, 2011, **18**, 1082–1090.
93 M. Mousavi-Kamazani and F. Azizi, *Ultrason. Sonochem.*, 2019, **58**, 104695.
94 M. J. Kishor Kumar and J. T. Kalathi, *J. Alloys Compd.*, 2018, **748**, 348–354.
95 M. T. Noman, M. Petru, J. Militky, M. Azeem and M. A. Ashraf, *Materials*, 2020, **13**, 14.
96 V. Ramasamy Raja, D. R. Rosaline, A. Suganthi and M. Rajarajan, *Ultrason. Sonochem.*, 2018, **44**, 310–318.
97 A. Manivel, G. J. Lee, C. Y. Chen, J. H. Chen, S. H. Ma, T. L. Horng and J. J. Wu, *Mater. Res. Bull.*, 2015, **62**, 184–191.
98 G. Gyawali, R. Adhikari, B. Joshi, T. H. Kim, V. Rodríguez-González and S. W. Lee, *J. Hazard. Mater.*, 2013, **263**, 45–51.
99 R. Arunadevi, B. Kavitha, M. Rajarajan and A. Suganthi, *Chem. Phys. Lett.*, 2019, **715**, 252–262.
100 A. Hassanjani-Roshan, M. R. Vaezi, A. Shokuhfar and Z. Rajabali, *Particuology*, 2011, **9**, 95–99.
101 C. N. C. Hitam and A. A. Jalil, *J. Environ. Manage.*, 2020, **258**, 110050.
102 W. S. Koe, J. W. Lee, W. C. Chong, Y. L. Pang and L. C. Sim, *Environ. Sci. Pollut. Res.*, 2020, **27**, 2522–2565.
103 P. O. Oladoye, T. O. Ajiboye, E. O. Omotola and O. J. Oyewola, *Results Eng.*, 2022, **16**, 100678.
104 A. Krishna Moorthy, B. Govindarajan Rathi, S. P. Shukla, K. Kumar and V. Shree Bharti, *Environ. Toxicol. Pharmacol.*, 2021, **82**, 103552.
105 S. Dardouri and J. Sghaier, *Korean J. Chem. Eng.*, 2017, **34**, 1037–1043.
106 S. A. Ong, E. Toorisaka, M. Hirata and T. Hano, *J. Hazard. Mater.*, 2005, **124**, 88–94.
107 M. Saeed, M. A. Jamal, A. U. Haq, M. Ilyas, M. Younas and M. A. Shahzad, *Int. J. Chem. React. Eng.*, 2016, **14**, 45–51.
108 I. Khan, K. Saeed, I. Zekker, B. Zhang, A. H. Hendi, A. Ahmad, S. Ahmad, N. Zada, H. Ahmad, L. A. Shah, T. Shah and I. Khan, *Water*, 2022, **14**, 242.
109 M. Khodaie, N. Ghasemi, B. Moradi and M. Rahimi, *J. Chem.*, 2013, **2103**, 1–7.

110 R. R. Ramsay, C. Dunford and P. K. Gillman, *Br. J. Pharmacol.*, 2007, **152**, 946–951.
111 J. Fito, S. Abrham and K. Angassa, *Int. J. Environ. Res.*, 2020, **14**, 501–511.
112 A. M. McDonnell, I. Rybak, M. Wadleigh and D. C. Fisher, *J. Oncol. Pharm. Pract.*, 2012, **18**, 436–439.
113 P. K. Gillman, *Anaesthesia*, 2006, **61**, 1007–1019.
114 R. Prashant and S. Jyothi, *J. Anaesthesiol., Clin. Pharmacol.*, 2010, **26**, 517–520.
115 S. Shakoor and A. Nasar, *Groundw. Sustain. Dev.*, 2017, **5**, 152–159.
116 X. He and C. Zhang, *J. Mater. Sci.*, 2019, **54**, 8831–8851.
117 A. Ajmal, I. Majeed, R. N. Malik, H. Idriss and M. A. Nadeem, *RSC Adv.*, 2014, **4**, 37003–37026.
118 T. Velempini, E. Prabakaran and K. Pillay, *Mater. Today Chem.*, 2021, **19**, 100380.
119 H. Tong, S. Ouyang, Y. Bi, N. Umezawa, M. Oshikiri and J. Ye, *Adv. Mater.*, 2012, **24**, 229–251.
120 J. Zhu and M. Zäch, *Curr. Opin. Colloid Interface Sci.*, 2009, **14**, 260–269.
121 M. Nazim, A. A. P. Khan, A. M. Asiri and J. H. Kim, *ACS Omega*, 2021, **6**, 2601–2612.
122 P. Sangpour, F. Hashemi and A. Z. Moshfegh, *J. Phys. Chem. C*, 2010, **114**, 13955–13961.
123 Q. Xiao, J. Zhang, C. Xiao, Z. Si and X. Tan, *Sol. Energy*, 2008, **82**, 706–713.
124 K. V. Kumar, K. Porkodi and F. Rocha, *Catal. Commun.*, 2008, **9**, 82–84.
125 N. G. Asenjo, R. Santamaría, C. Blanco, M. Granda, P. Álvarez and R. Menéndez, *Carbon*, 2013, **55**, 62–69.
126 H. Anwer, A. Mahmood, J. Lee, K. H. Kim, J. W. Park and A. C. K. Yip, *Nano Res.*, 2019, **12**, 955–972.
127 A. M. Mohammed, S. S. Mohtar, F. Aziz, S. A. Mhamad and M. Aziz, *J. Environ. Chem. Eng.*, 2021, **9**, 105138.
128 I. Ahmad, Y. Zou, J. Yan, Y. Liu, S. Shukrullah, M. Y. Naz, H. Hussain, W. Q. Khan and N. R. Khalid, *Adv. Colloid Interface Sci.*, 2023, **311**, 102830.
129 Y. Liu, W. Wang, X. Xu, J. P. Marcel Veder and Z. Shao, *J. Mater. Chem. A*, 2019, **7**, 7280–7300.
130 X. Lin, D. Fu, L. Hao and Z. Ding, *J. Environ. Sci.*, 2013, **25**, 2150–2156.
131 Z. Ji, Z. Luo, J. Li and P. Li, *Phys. Status Solidi A*, 2019, **216**, 1–9.
132 T. Leijtens, G. E. Eperon, A. J. Barker, G. Grancini, W. Zhang, J. M. Ball, A. R. S. Kandada, H. J. Snaith and A. Petrozza, *Energy Environ. Sci.*, 2016, **9**, 3472–3481.
133 B. Peng, X. Meng, F. Tang, X. Ren, D. Chen and J. Ren, *J. Phys. Chem. C*, 2009, **113**, 20240–20245.
134 K. Pradeev raj, K. Sadaiyandi, A. Kennedy, S. Sagadevan, Z. Z. Chowdhury, M. R. Bin Johan, F. A. Aziz, R. F. Rafique, R. Thamiz Selvi and R. Rathina bala, *Nanoscale Res. Lett.*, 2018, **13**, 229.
135 N. Sakaguchi Miyamoto, R. Miyamoto, E. Giamello, T. Kurisaki and H. Wakita, *Res. Chem. Intermed.*, 2018, **44**, 4577–4594.
136 T. Narkbuakaew and P. Sujaridworakun, *Opt. Mater.*, 2019, **98**, 109407.
137 J. I. Garza-Arévalo, I. García-Montes, M. H. Reyes, J. L. Guzmán-Mar, V. Rodríguez-González and L. H. Reyes, *Mater. Res. Bull.*, 2016, **73**, 145–152.
138 W. Xie, R. Li and Q. Xu, *Sci. Rep.*, 2018, **8**, 1–10.
139 P. Karuppasamy, N. Ramzan Nilofar Nisha, A. Pugazhendhi, S. Kandasamy and S. Pitchaimuthu, *J. Environ. Chem. Eng.*, 2021, **9**, 105254.
140 A. Khlyustova, N. Sirotkin, T. Kusova, A. Kraev, V. Titov and A. Agafonov, *Mater. Adv.*, 2020, **1**, 1193–1201.
141 S. Saroj, L. Singh and S. V. Singh, *J. Photochem. Photobiol., A*, 2020, **396**, 112532.
142 S. Ramandi, M. H. Entezari and N. Ghows, *Ultrason. Sonochem.*, 2017, **38**, 234–245.
143 N. U. Saqib, R. Adnan and I. Shah, *Mater. Res. Express*, 2019, **6**, 095506.
144 L. N. Song, F. Ding, Y. K. Yang, D. Ding, L. Chen, C. T. Au and S. F. Yin, *ACS Sustainable Chem. Eng.*, 2018, **6**, 17044–17050.
145 A. M. Abdel-Wahab, A. S. Al-Shirbini, O. Mohamed and O. Nasr, *J. Photochem. Photobiol., A*, 2017, **347**, 186–198.
146 G. Dong, Y. Wang, H. Lei, G. Tian, S. Qi and D. Wu, *J. Cleaner Prod.*, 2020, **253**, 120021.
147 M. Mohammadi and S. Sabbaghi, *Environ. Nanotechnol., Monit. Manage.*, 2014, **1–2**, 24–29.
148 J. Abdi, M. Yahyanezhad, S. Sakhaie, M. Vossoughi and I. Alemzadeh, *J. Environ. Chem. Eng.*, 2019, **7**, 103096.
149 Y. Zhang, X. Hou, T. Sun and X. Zhao, *Ceram. Int.*, 2017, **43**, 1150–1159.
150 D. Monga and S. Basu, *Adv. Powder Technol.*, 2019, **30**, 1089–1098.
151 W. K. Jo and T. S. Natarajan, *Chem. Eng. J.*, 2015, **281**, 549–565.
152 E. Vasilaki, I. Georgaki, D. Vernardou, M. Vamvakaki and N. Katsarakis, *Appl. Surf. Sci.*, 2015, **353**, 865–872.
153 M. Kocijan, L. Curkovi, T. Radoševi and M. Podlogar, *Catal. Artic.*, 2021, **11**, 1–16.
154 K. P. Ghoderao, S. N. Jamble and R. B. Kale, *Optik*, 2018, **156**, 758–771.
155 M. C. Uribe-López, M. C. Hidalgo-López, R. López-González, D. M. Frías-Márquez, G. Núñez-Nogueira, D. Hernández-Castillo and M. A. Alvarez-Lemus, *J. Photochem. Photobiol., A*, 2021, **404**, 112866.
156 M. M. Ba-Abbad, A. A. H. Kadhum, A. B. Mohamad, M. S. Takriff and K. Sopian, *Chemosphere*, 2013, **91**, 1604–1611.
157 U. Alam, A. Khan, D. Ali, D. Bahnemann and M. Muneer, *RSC Adv.*, 2018, **8**, 17582–17594.
158 K. Qi, X. Xing, A. Zada, M. Li, Q. Wang, S. yuan Liu, H. Lin and G. Wang, *Ceram. Int.*, 2020, **46**, 1494–1502.
159 Z. Mirzaeifard, Z. Shariatinia, M. Jourshabani and S. M. Rezaei Darvishi, *Ind. Eng. Chem. Res.*, 2020, **59**, 15894–15911.
160 M. J. Mochane, M. T. Motloung, T. C. Mokhena and T. G. Mofokeng, *Catalysts*, 2022, **12**, 1439.
161 E. Mugunthan, M. B. Saidutta and P. E. Jagadeeshbabu, *J. Photochem. Photobiol., A*, 2019, **383**, 111993.

162 J. Lin, Z. Luo, J. Liu and P. Li, *Mater. Sci. Semicond. Process.*, 2018, **87**, 24–31.
163 S. Begum, S. R. Mishra and M. Ahmaruzzaman, *Environ. Sci. Pollut. Res.*, 2022, **29**, 87347–87360.
164 P. Cheng, Y. Wang, L. Xu, P. Sun, Z. Su, F. Jin, F. Liu, Y. Sun and G. Lu, *Mater. Lett.*, 2016, **175**, 52–55.
165 S. P. Lonkar, V. Pillai and A. Abdala, *Appl. Surf. Sci.*, 2019, **465**, 1107–1113.
166 W. M. Liu, J. Li and H. Y. Zhang, *Optik*, 2020, **207**, 163778.
167 P. Van Tuan, T. T. Phuong, V. T. Tan, S. X. Nguyen and T. N. Khiem, *Mater. Sci. Semicond. Process.*, 2020, **115**, 105114.
168 M. Ahmad, I. Ahmad, E. Ahmed, M. S. Akhtar and N. R. Khalid, *J. Mol. Liq.*, 2020, **311**, 113326.
169 I. Ahmad, *Sep. Purif. Technol.*, 2020, **251**, 117372.
170 O. Długosz and M. Banach, *Appl. Nanosci.*, 2021, **11**, 1707–1719.
171 M. A. Butler, R. D. Nasby and R. K. Quinn, *Solid State Commun.*, 1976, **19**, 1011–1014.
172 R. Rong and L. Wang, *J. Alloys Compd.*, 2021, **850**, 156742.
173 S. Ramkumar and G. Rajarajan, *Appl. Phys. A: Mater. Sci. Process.*, 2017, **123**, 1–8.
174 C. Wang, X. Zhang, B. Yuan, Y. Wang, P. Sun, D. Wang, Y. Wei and Y. Liu, *Chem. Eng. J.*, 2014, **237**, 29–37.
175 G. Jeevitha, R. Abhinayaa, D. Mangalaraj and N. Ponpandian, *J. Phys. Chem. Solids*, 2018, **116**, 137–147.
176 B. Esencan Türkaslan, A. K. Çelik, A. Dalbeyler and N. Fantuzzi, *Materials*, 2022, **15**, 8019.
177 V. Ramar and K. Balasubramanian, *ACS Appl. Nano Mater.*, 2021, **4**, 5512–5521.
178 T. Govindaraj, C. Mahendran, V. S. Manikandan, J. Archana, M. Shkir and J. Chandrasekaran, *J. Alloys Compd.*, 2021, **868**, 159091.
179 V. A. Tran, T. P. Nguyen, V. T. Le, I. T. Kim, S. W. Lee and C. T. Nguyen, *J. Sci.: Adv. Mater. Devices*, 2021, **6**, 108–117.
180 Y. Yang, B. Liu, J. Xu, Q. Wang, X. Wang, G. Lv and J. Zhou, *ACS Omega*, 2022, **7**, 6035–6045.
181 M. Y. Khan, M. Ahmad, S. Sadaf, S. Iqbal, F. Nawaz and J. Iqbal, *J. Mater. Res. Technol.*, 2019, **8**, 3261–3269.
182 A. Kerour, S. Boudjadar, R. Bourzami and B. Allouche, *J. Solid State Chem.*, 2018, **263**, 79–83.
183 S. Yadav, M. Chauhan, D. Mathur, A. Jain and P. Malhotra, *Environ. Dev. Sustain.*, 2021, **23**, 2071–2091.
184 D. A. Prado-Chay, M. A. Cortés-Jácome, C. Angeles-Chávez, R. Oviedo-Roa, J. M. Martínez-Magadán, C. Zuriaga-Monroy, I. J. Hernández-Hernández, P. R. Mayoral, D. R. Gómora-Herrera and J. A. Toledo-Antonio, *Top. Catal.*, 2020, **63**, 586–600.
185 Y. Wang, J. Gao, X. Wang, L. Jin, L. Fang, M. Zhang, G. He and Z. Sun, *J. Sol-Gel Sci. Technol.*, 2018, **88**, 172–180.
186 K. Polat, *Thin Solid Films*, 2020, **709**, 138254.
187 S. Karthikeyan, K. Ahmed, A. Osatiashtiani, A. F. Lee, K. Wilson, K. Sasaki, B. Coulson, W. Swansborough-Aston, R. E. Douthwaite and W. Li, *ChemCatChem*, 2020, **12**, 1699–1709.
188 M. V. Kangralkar, V. A. Kangralkar, N. Momin and J. Manjanna, *Environ. Nanotechnol., Monit. Manage.*, 2019, **12**, 100265.
189 S. Masudy-Panah, R. Katal, N. D. Khiavi, E. Shekarian, J. Hu and X. Gong, *J. Mater. Chem. A*, 2019, **7**, 22332–22345.
190 H. Gao, J. Zhang and M. Wang, *Mater. Res. Bull.*, 2013, **48**, 3431–3437.
191 K. Chen, X. Wang, P. Xia, J. Xie, J. Wang, X. Li, Y. Tang and L. Li, *Chemosphere*, 2020, **254**, 126806.
192 R. Banu, N. Salvi, S. Gupta, C. Ameta, R. Ameta and P. B. Punjabi, *Arabian J. Sci. Eng.*, 2022, **47**, 365–378.
193 Z. Zhang, L. Sun, Z. Wu, Y. Liu and S. Li, *New J. Chem.*, 2020, **44**, 6420–6427.
194 A. A. M. Sakib, S. M. Masum, J. Hoinkis, R. Islam and M. A. I. Molla, *J. Compos. Sci.*, 2019, **3**, 91.
195 D. Malwal and P. Gopinath, *Catal. Sci. Technol.*, 2016, **6**, 4458–4472.
196 A. George, D. Magimai Antoni Raj, X. Venci, A. Dhayal Raj, A. Albert Irudayaraj, R. L. Josephine, S. John Sundaram, A. M. Al-Mohaimeed, D. A. Al Farraj, T. W. Chen and K. Kaviyarasu, *Environ. Res.*, 2022, **203**, 111880.
197 M. Maraj, A. Raza, X. Wang, J. Chen, K. N. Riaz and W. Sun, *Catalysts*, 2021, **11**, 1–10.
198 M. R. Islam, M. Saiduzzaman, S. S. Nishat, A. Kabir and S. F. U. Farhad, *Colloids Surf., A*, 2021, **617**, 126386.
199 S. Aroob, S. A. C. Carabineiro, M. B. Taj, I. Bibi, A. Raheel, T. Javed, R. Yahya, W. Alelwani, F. Verpoort, K. Kamwilaisak, S. Al-Farraj and M. Sillanpää, *Catalysts*, 2023, **13**, 502.
200 M. Rafique, F. Shafiq, S. S. Ali Gillani, M. Shakil, M. B. Tahir and I. Sadaf, *Optik*, 2020, **208**, 164053.
201 K. Kannan, D. Radhika, S. Vijayalakshmi, K. K. Sadasivuni, A. A. Ojiaku and U. Verma, *Int. J. Environ. Anal. Chem.*, 2022, **102**, 1095–1108.
202 Y. Duan, *Mater. Res. Bull.*, 2018, **105**, 68–74.
203 M. A. Hanif, J. Akter, Y. S. Kim, H. G. Kim, J. R. Hahn and L. K. Kwac, *Catalysts*, 2022, **12**, 151.
204 S. P. Kim, M. Y. Choi and H. C. Choi, *Mater. Res. Bull.*, 2016, **74**, 85–89.
205 Y. Li, Q. Yang, Z. Wang, G. Wang, B. Zhang, Q. Zhang and D. Yang, *Inorg. Chem. Front.*, 2018, **5**, 3005–3014.
206 L. G. Devi and R. Shyamala, *Mater. Chem. Front.*, 2018, **2**, 796–806.
207 S. Yao, S. Zhou, J. Wang, W. Li and Z. Li, *Photochem. Photobiol. Sci.*, 2019, **18**, 2989–2999.
208 C. Wang, G. Guo, C. Zhu, Y. Li, Y. Jin, B. Zou, H. He and A. Wang, *Nanomaterials*, 2022, **12**, 3151.
209 S. A. Ansari, M. M. Khan, M. O. Ansari, J. Lee and M. H. Cho, *RSC Adv.*, 2014, **4**, 26013–26021.
210 L. Ran, D. Zhao, X. Gao and L. Yin, *CrystEngComm*, 2015, **17**, 4225–4237.
211 A. B. Ali Baig, V. Rathinam and V. Ramya, *Adv. Compos. Hybrid Mater.*, 2021, **4**, 114–126.
212 Q. Wang, X. Chen, J. Tian, L. Wei, Y. Liu and C. Yang, *J. Mater. Sci.: Mater. Electron.*, 2020, **31**, 16991–17002.
213 H. Ji, Y. Fan, J. Yan, Y. Xu, X. She, J. Gu, T. Fei, H. Xu and H. Li, *RSC Adv.*, 2017, **7**, 36101–36111.

214 S. Kavitha, N. Jayamani and D. Barathi, *Bull. Mater. Sci.*, 2021, **44**, 26.
215 M. Kumar and A. Rahman, *J. Inst. Eng.: Ser. E*, 2023, **104**, 95–108.
216 L. Machala, J. Tuček and R. Zbořil, *Chem. Mater.*, 2011, **23**, 3255–3272.
217 Y. Wang, S. Wang, Y. Wu, Z. Wang, H. Zhang, Z. Cao, J. He, W. Li, Z. Yang, L. Zheng, D. Feng, P. Pan, J. Bi, H. Li, J. Zhao and K. Zhang, *J. Alloys Compd.*, 2021, **851**, 156733.
218 M. A. Hoque, M. R. Ahmed, G. T. Rahman, M. T. Rahman, M. A. Islam, M. A. Khan and M. K. Hossain, *Results Phys.*, 2018, **10**, 434–443.
219 N. Li, Y. Jiang, Y. long He, L. Gao, Z. zhou Yi, F. rui Zhai and K. Chattopadhyay, *J. Mater. Res. Technol.*, 2021, **15**, 810–820.
220 R. A. Senthil, A. Priya, J. Theerthagiri, A. Selvi, P. Nithyadharseni and J. Madhavan, *Ionics*, 2018, **24**, 3673–3684.
221 T. Zhang, J. Liu, F. Zhou, S. Zhou, J. Wu, D. Chen, Q. Xu and J. Lu, *ACS Appl. Nano Mater.*, 2020, **3**, 9200–9208.
222 S. Y. Mendiola-Alvarez, A. Hernández-Ramírez, J. L. Guzmán-Mar, M. L. Maya-Treviño, A. Caballero-Quintero and L. Hinojosa-Reyes, *Catal. Today*, 2019, **328**, 91–98.
223 S. Frindy and M. Sillanpää, *Mater. Des.*, 2020, **188**, 108461.
224 X. Liu, K. Chen, J. J. Shim and J. Huang, *J. Saudi Chem. Soc.*, 2015, **19**, 479–484.
225 H. Mansour, K. Omri, R. Bargougui and S. Ammar, *Appl. Phys. A: Mater. Sci. Process.*, 2020, **126**, 1–10.
226 Q. Mei, F. Zhang, N. Wang, Y. Yang, R. Wu and W. Wang, *RSC Adv.*, 2019, **9**, 22764–22771.
227 T. J. Al-Musawi, R. Asgariyan, M. Yilmaz, N. Mengelizadeh, A. Asghari, D. Balarak and M. Darvishmotevall, *Magnetochemistry*, 2022, **8**, 137.
228 B. Mandal, J. Panda and B. Tudu, *AIP Conf. Proc.*, 2018, **1953**, 030173.
229 Y. Q. Cao, T. Q. Zi, X. R. Zhao, C. Liu, Q. Ren, J. Bin Fang, W. M. Li and A. D. Li, *Sci. Rep.*, 2020, **10**, 1–10.
230 Y. Zhu, J. Xue, T. Xu, G. He and H. Chen, *J. Mater. Sci.: Mater. Electron.*, 2017, **28**, 8519–8528.
231 K. K. Bera, M. Chakraborty, M. Mondal, S. Banik and S. K. Bhattacharya, *Ceram. Int.*, 2020, **46**, 7667–7680.
232 T. Li, S. Quan, X. Shi, L. Yang and C. Liu, *Catal. Lett.*, 2020, **150**, 640–651.
233 S. Singh and R. Sharma, *Sol. Energy Mater. Sol. Cells*, 2018, **186**, 208–216.
234 Y. Long, L. Li, S. Wang, Y. Chen, L. Wang, S. Zhang, L. Luo and F. Jiang, *Catal. Lett.*, 2018, **148**, 3608–3617.
235 S. Zhang, S. Cao, Q. Shi, Y. Zhang, D. Sun, T. Tang and X. Zhang, *Inorg. Chem.*, 2020, **59**, 18131–18140.
236 A. Hezam, K. Namratha, D. Ponnamma, Q. A. Drmosh, A. M. N. Saeed, C. Cheng and K. Byrappa, *ACS Omega*, 2018, **3**, 12260–12269.
237 S. H. Hsieh, A. Manivel, G. J. Lee and J. J. Wu, *Mater. Res. Bull.*, 2013, **48**, 4174–4180.
238 Y. Cui, X. Zhang, R. Guo, H. Zhang, B. Li, M. Xie, Q. Cheng and X. Cheng, *Sep. Purif. Technol.*, 2018, **203**, 301–309.
239 D. S. Bhachu, S. Sathasivam, C. J. Carmalt and I. P. Parkin, *Langmuir*, 2014, **30**, 624–630.
240 A. Leelavathi, B. Mukherjee, C. Nethravathi, S. Kundu, M. Dhivya, N. Ravishankar and G. Madras, *RSC Adv.*, 2013, **3**, 20970–20977.
241 A. M. Mebed, A. M. Abd-Elnaiem, A. H. Alshammari, T. A. Taha, M. Rashad and D. Hamad, *Catalysts*, 2022, **12**, 142.
242 Z. Wang, V. Srivastava, S. Iftekhar, I. Ambat and M. Sillanpää, *Chem. Eng. J.*, 2018, **354**, 663–671.
243 F. Y. Liu, J. H. Lin, Y. M. Dai, L. W. Chen, S. T. Huang, T. W. Yeh, J. L. Chang and C. C. Chen, *Catal. Today*, 2018, **314**, 28–41.
244 F. T. Geldasa, M. Kebede, M. W. Shura, D. M. Andoshe, N. Tegegne and F. Gashaw Hone, *Phys. Scr.*, 2023, **98**, 065701.
245 Y. Wang, C. Yang, K. Zhang, L. Guo, R. Li, A. Zaheer, F. Fu, B. Xu and D. Wang, *Colloids Surf., A*, 2022, **634**, 127965.
246 F. T. Geldasa, M. A. Kebede, M. W. Shura and F. G. Hone, *AIP Adv.*, 2022, **12**, 115302.
247 C. G. Poll and D. J. Payne, *Electrochim. Acta*, 2014, **156**, 283–288.
248 J. Li, M. Guo, Y. Shao, H. Yu and K. Ni, *ACS Omega*, 2021, **6**, 5436–5444.
249 E. Najafi, M. M. Amini, F. Behmagham, N. Shaabani and N. Shojaei, *Chem. Rev. Lett.*, 2019, **2**, 13–20.
250 H. Karami, M. A. Karimi, S. Haghdar, A. Sadeghi, R. Mir-Ghasemi and S. Mahdi-Khani, *Mater. Chem. Phys.*, 2008, **108**, 337–344.
251 K. T. Arulmozhi and N. Mythili, *AIP Adv.*, 2013, **3**, 122122.
252 S. K. Noukelag, H. E. A. Mohamed, L. C. Razanamahandry, S. K. O. Ntwampe and C. J. Arendse, *Mater. Today: Proc.*, 2019, **36**, 421–426.
253 S. K. Behzad, E. Najafi, M. M. Amini, A. Tadjarodi, A. Dehghani and B. Notash, *Monatsh. Chem.*, 2015, **146**, 35–45.
254 K. H. H. Al-Attiyah, A. Hashim and S. F. Obaid, *Int. J. Plast. Technol.*, 2019, **23**, 39–45.
255 F. Temerov, Y. Baghdadi, E. Rattner and S. Eslava, *ACS Appl. Energy Mater.*, 2022, **5**, 14605–14637.
256 Y. C. Wang, A. H. Lee and C. C. Chen, *J. Taiwan Inst. Chem. Eng.*, 2018, **93**, 315–328.
257 Y. Li, J. Zhao, G. Zhang, L. Zhang, S. Ding, E. Shang and X. Xia, *Water Res.*, 2019, **161**, 251–261.
258 W. Kohn, A. D. Becke and R. G. Parr, *J. Phys. Chem.*, 1996, **100**, 12974–12980.
259 X. Andrade, C. Das Pemmaraju, A. Kartsev, J. Xiao, A. Lindenberg, S. Rajpurohit, L. Z. Tan, T. Ogitsu and A. A. Correa, *J. Chem. Theory Comput.*, 2021, **17**, 7447–7467.
260 A. Iwaszuk and M. Nolan, *Catal. Sci. Technol.*, 2013, **3**, 2000–2008.
261 N. Kitchamsetti, M. S. Ramteke, S. R. Rondiya, S. R. Mulani, M. S. Patil, R. W. Cross, N. Y. Dzade and R. S. Devan, *J. Alloys Compd.*, 2021, **855**, 157337.
262 B. Huang and J. N. Hart, *Phys. Chem. Chem. Phys.*, 2020, **22**, 1727–1737.

263 W. Yao, D. Li, S. Wei, X. Liu, X. Liu and W. Wang, *ACS Omega*, 2022, **7**, 36479–36488.
264 N. I. Oktavianti, G. R. Anindika, A. L. Ivansyah, H. Juwono and Y. Kusumawati, *AIP Conf. Proc.*, 2021, **2349**, 020063.
265 R. Gusain, N. Kumar and S. S. Ray, in *Photocatalysts in Advanced Oxidation Processes for Wastewater Treatment*, 2020, pp. 229–270.
266 S. G. Shelar, V. K. Mahajan, S. P. Patil and G. H. Sonawane, *SN Appl. Sci.*, 2020, **2**, 1–10.
267 A. Mohagheghian, S. A. Karimi, J. K. Yang and M. Shirzad-Siboni, *J. Adv. Oxid. Technol.*, 2015, **18**, 61–68.
268 A. Rafiq, M. Ikram, S. Ali, F. Niaz, M. Khan, Q. Khan and M. Maqbool, *J. Ind. Eng. Chem.*, 2021, **97**, 111–128.
269 M. Senthil Kumar and C. Arunagiri, *J. Mater. Sci.: Mater. Electron.*, 2021, **32**, 17925–17935.
270 U. G. Akpan and B. H. Hameed, *J. Hazard. Mater.*, 2009, **170**, 520–529.
271 M. Saquib, M. A. Tariq, M. Faisal and M. Muneer, *Adv. Sci. Lett.*, 2010, **3**, 512–517.
272 K. M. Reza, A. Kurny and F. Gulshan, *Appl. Water Sci.*, 2017, **7**, 1569–1578.
273 B. Neppolian, H. C. Choi, S. Sakthivel, B. Arabindoo and V. Murugesan, *J. Hazard. Mater.*, 2002, **89**, 303–317.
274 N. A. Galedari, M. Rahmani and M. Tasbihi, *Environ. Sci. Pollut. Res.*, 2017, **24**, 12655–12663.